Universität Rostock

Traditio et Innovatio

Dynamic compression experiments of SiO_2 and GeO_2 at synchrotron- and X-ray free electron laser (XFEL) light sources

Dissertation

zur

Erlangung des akademischen Grades

doctor rerum naturalium (Dr. rer. nat)

der Mathematisch-Naturwissenschaftlichen Fakultät

der Universität Rostock

vorgelegt von

Markus Schölmerich, geb. am 11.07.1986 in Freiburg

aus Hamburg

Rostock, 16.10.2020

1. Gutachter: Prof. Ronald Redmer

2. Gutachter: Prof. Hauke Marquardt

Einreichung: 16.10.2020

Universität Rostock
Institut für Physik
18051 Rostock
Tel: +49 381 498-6916
Fax: +49 381 498-6912
Internet: http://www.physik.uni-rostock.de

Email des Autors: markus.schoelmerich@xfel.eu

Abstract

There is a growing interest in the application of experimental studies of geological materials at high pressure- and temperature conditions to both new and long-standing theories in Earth and planetary science. Such experiments can address essential questions about the structure, dynamics and evolution of the Earth's interior. In addition, the discovery of thousands of extra-solar planets around other stars raised interest about the diversity of planetary architectures, compositions and how such planets might form and evolve.
Silica is one of the most fundamental constituents in planetary science, being vastly abundant in the Earth's crust and mantle. As an essential 'building block', it bonds with Mg, Fe and other elements to form major mineral phases and even free SiO_2 can be expected in localized regions in the Earth's mantle, derived from e.g. subducted oceanic crust. The stability of SiO_2 within these regions is vastly affected by polymorphism at high pressures and SiO_2 serves as an archetype for the dense highly coordinated silicates of planetary interiors and large exoplanets (1-10 M_E).
In this work, the high pressure behavior of four major SiO_2 polymorphs as well as the structural analogue GeO_2 were investigated by means of dynamic compression: α-quartz, fused silica, stishovite and α-cristobalite. Here, laser shock compression and dynamic diamond anvil cell (dDAC) techniques were applied. The concomitant use of hard X-ray radiation at synchrotron- and X-ray free electron laser (XFEL) light sources made a time-resolved investigation of the lattice response at high pressures possible. From laser shock compression, a phase transformation of α-quartz to stishovite, the high-pressure SiO_2 polymorph, as well as to the metastable defective niccolite structure at pressures between 45 GPa and 94 GPa could be demonstrated. By using stishovite as the starting material, it was furthermore shown, that the stishovite (=rutile) structure is stable upon shock loading to 336 GPa, a result deviating strongly from equilibrium data. Moreover, melting of α-quartz, fused silica and α-cristobalite was observed at pressures greater than 119 GPa, 126 GPa and 70 GPa, respectively. At late XFEL probe time delays of up to 200 ns, a resulting recrystallisation from initially crystalline material was shown (α-quartz and α-cristobalite) but not from vitreous silica glass, which indicates a remaining short-range bonding within the melt, from which strong coalescence growth is assumed. The investigation of GeO_2 by means of laser shock compression, revealed a phase transformation of an initially quartz-like structure towards the rutile structure at 19 GPa and a subsequent

melt signature at peak pressures of 53 GPa and 104 GPa. Here, a change of the bond distance of Ge-O and Ge-Ge was demonstrated, which was accompanied by a change of coordination from initially 4-fold to 6.8-fold at 104 GPa.

Ultimately, from the dynamic compression of α-cristobalite by means of the dDAC, phase transitions to the high pressure polymorphs critobalite II, cristobalite X-I and seifertite was demonstrated. The pressure onsets of these phase transitions are directly correlated to the applied compression rate, and the increasing compression rates can shift the transition to higher pressures. Increasing compression rates or applied moderate temperatures (500 °C and 700 °C) furthermore have a direct impact on the molecular unit cell volume of seifertite, which deviates strongly from equilibrium data. Finally, the effect of hydrostaticity within the dDAC was investigated. The experiments revealed, that the phase transition of cristobalite X-I to seifertite is hindered at hydrostatic experimental conditions, e.g. with single crystal α-cristobalite as the starting material. Finally, these results were benchmarked and confirmed by means of metadynamics simulations derived from density functional theory molecular dynamics (DFT-MD) calculations.

Zusammenfassung

Die Entdeckung tausender extrasolarer Planeten (Exoplaneten) in anderen Sonnensystemen wirft neue Fragen in Bezug auf deren Zusammensetzung, Entstehung und Entwicklung auf, die durch experimentelle Untersuchungen geologischer Materialien entschlüsselt werden sollen. Die sogenannten "Super-Erden" haben häufig die 10-fache Masse der Erde und sind mehr als doppelt so groß. Dies hat einen Einfluss auf die vorherrschenden Mineralphasen im Planeten-Inneren, welche ernormen Drücken unterliegen. Ausgehend von den abundanten Phasen unserer Erde, ist davon auszugehen, dass die primären Minerale im Mantel von Super-Erden aus MgO, FeO, $MgSiO_3$ und SiO_2 bestehen. Siliziumdioxid (SiO_2) ist hierbei einer der grundlegendsten Bestandteile, da es in unserer Erdkruste und im Erdmantel überdurchschnittlich häufig vorkommt. Als wesentlicher Baustein geht es mit Mg, Fe und anderen Elementen eine Verbindung ein, um die primären Mineralphasen des Erdmantels zu bilden. In manchen Bereichen des Erdmantels wird sogar reines SiO_2 angenommen, welches z.B. durch ozeanische Kruste subduziert worden ist. Die Stabilität der Minerale wird hierbei durch die Hochdruckmodifikationen von SiO_2 beeinflusst. Zudem stellt SiO_2 ein Archetyp für die dichten Silikate im tiefen Mantel der Erde und großer (1-10 M_E) Exoplaneten dar.

In dieser Arbeit wurde das Hochdruckverhalten von vier SiO_2 Modifikationen und dem strukturellen Analogons GeO_2 mit Hilfe dynamischer Kompression durch Laser induzierten Schock und der dynamischen Diamantstempelzelle (dDAC) untersucht: α-Quarz, Quarzglas, Stishovit und α-Christobalit. Die gleichzeitige Verwendung harter Röntgenstrahlung eines Synchrotrons oder Freien Elektronenlasers (XFEL) ermöglicht eine zeitaufgelöste Untersuchung der Gitterstruktur dieser Materialien. In dieser Arbeit wurde gezeigt, dass die schnellen Kompressionsraten der dynamischen Experimente einen immensen Einfluss auf das Einsetzen der Phasenübergange hat. Durch die Anwendung Laser induzierter Schock-Kompression wurde ein Phasenübergang von α-Quarz zu Stishovit, eine Hochdruckmodifikation von SiO_2, bei einem Druck von 45 GPa beobachtet. Zudem wurde ein Phasenübergang zu einer metastabilen Struktur (*d*-NiAs) bei einem Druck zwischen 73 GPa und 94 GPa gezeigt. Nutzt man Stishovit als Startmaterial, blieb die Struktur bis zu einem Druck von 336 GPa unverändert. Dies stellt einen starken Kontrast zu statischen Experimenten dar, in denen ein Phasenübergang zu der silikatischen $CaCl_2$ Hochdruckmodifikation beobachtet wurde.

Zudem wurde das Schmelzverhalten von α-Quarz, Quarzglas und α-Cristobalit durch Röntgenbeugung bei Drücken von über 119 GPa, 126 GPa und 70 GPa untersucht. Eine späte Bebrobung mit dem XFEL relativ zum Schock von bis zu 200 ns zeigte einen Rekristallisationseffekt von ursprünglich kristallinem Material (α-Quarz und α-Cristobalit) auf. Dieser Effekt war jedoch nicht mit Quarzglas als Startmaterial zu beobachten. Dies deutet auf bestehende Ordnungseffekte der ursprünglich kristallinen Phasen innerhalb der Schmelze hin und es kann von einem starken Kristallwachstum von den Kristallisationskeimen ausgegangen werden. Die Untersuchung von GeO_2 durch Laser induzierte Schock-Kompression zeigte bei einem Druck von 19 GPa eine Phasenumwandlung von einer Quarz-artigen Struktur zu der Rutil-Struktur auf. Bei Drücken von 53 GPa und 104 GPa konnte eine Schmelzsignatur beobachtet und eine Veränderung der Ge-O und Ge-Ge Bindungslängen und der damit einhergehenden Koordinationszahl nachgewiesen werden.
Durch die dynamische Kompression von α-Cristobalit in der dDAC wurden die Phasenübergänge zu den Hochdruckmodifikationen Critobalite II, Cristobalit X-I und Seifertit beobachtet. Die Drücke dieser Phasenübergänge hingen direkt von der angewandten Kompressionsrate ab und zunehmende Kompressionsraten führten zu höheren Drücken der Phasenübergange. Zudem wirkten sich steigende Kompressionsraten auch direkt auf das Volumen der Einheitszelle von Seifertit aus, welche stark von statischen Experimenten abweicht. Dies zeigte sich auch für Experimente mit moderaten Temperaturen (500 °C und 700 °C). Zudem wurde der Effekt von hydrostatischen Bedingungen innerhalb der dDAC untersucht. Hier konnte gezeigt werden, dass quasi-hydrostatische Bedingungen unter Verwendung von α-Cristobalit Einkristallen zu dem Ausbleiben der Phasenumwandlung von Cristobalit X-I zu Seifertit führt, was im Gegensatz zu nicht-hydrostatischen Experimenten mit Pulver als Ausgangsmaterial steht. Die Ergebnisse wurden zudem durch Metadynamik-Berechnungen der Dichtefunktionaltheorie und Molekulardynamik Simulationen verglichen und bestätigt.

Contents

1 Introduction **1**

1.1 Mineralogy at Super-Earth interior conditions 1

1.1.1 Composition of Super-Earths 1

1.1.2 Crystal structure and phase transitions of silica and its structural polymorphs 2

1.2 Theoretical and experimental approaches for high-pressure research . . . 5

1.2.1 Theoretical models 5

1.2.2 Experimental techniques 6

1.3 Motivation and aim of this study 9

2 Material and Methods **11**

2.1 Laser induced shock compression 11

2.1.1 Sample preparation and sample synthesis 11

2.1.2 Experimental setup at MEC and BL3:EH5 15

2.2 Dynamic diamond anvil cell (dDAC) experiments 20

2.2.1 Sample preparation and sample synthesis 20

2.2.2 Experimental dDAC setup at P02.2 21

2.2.3 Resistive heated dDAC experiments 25

2.3 Computational simulations 28

2.3.1 1D radiation hydrodynamics simulations 28

2.3.2 Density functional theory (DFT) - molecular dynamic (MD) simulations 29

3 Results **33**

3.1 Laser induced shock compression experiments 34

3.1.1 α-Quartz 34

3.1.2 Stishovite 43

3.1.3 GeO_2 55

3.1.4 Shock melt and release experiments of α-quartz, α-cristobalite and fused silica 60

3.2 Dynamic diamond anvil cell experiments 64

3.2.1 Dynamic compression of powder α-cristobalite 64
3.2.2 Resistive heated experimental runs 69
3.2.3 Dynamic compression of single crystal α-cristobalite 72
3.2.4 Metadynamic simulations of α-cristobalite by means of variable cell DFT-MD calculations 73

4 Discussion **75**
4.1 Material response to laser induced shock compression 75
4.1.1 α-Quartz 75
4.1.2 Stishovite 78
4.1.3 GeO_2 80
4.1.4 Shock induced melting and recrystallization of α-quartz, α-cristobalite and fused silica 82
4.2 The effect of fast compression and temperature on phase transitions . . . 86
4.2.1 Laser induced shock compression 86
4.2.2 Dynamic compression with the (RH)dDAC 87
4.3 The effect of hydrostaticity on structural transformation pathways 89
4.3.1 Stishovite 89
4.3.2 α-Cristobalite 90
4.4 Conclusions and geophysical implications 92
4.4.1 The transformation pathways of silica and GeO_2 at high pressure conditions 92
4.4.2 Geophysical implications 95

Bibliography **99**

Curriculum vitae **111**

Acknowledgements **115**

Statement of authorship **117**

List of Figures

1.1 Mass-radius diagram of exoplanets with compositional trendlines 1
1.2 Schematic overview of the interior pressure conditions within the Earth and a representative Super-Earth 3
1.3 Polyhedral representation of α-quartz, α-cristobalite and stishovite 5
1.4 Peak pressures (GPa) achieved through various compression techniques as a function of year 6
1.5 Comparison of the (200) Bragg reflection of α-cristobalite at PETRAIII and SACLA 9

2.1 Target holder of MEC and BL3:EH5 and target assemblies on glass slides compressed by weights 12
2.2 Large volume press assembly 13
2.3 Photographs of the LVP cell assembly, the LVP and stishovite encapsuled in Pt 14
2.4 X-ray diffraction pattern of the stishovite synthesis product. 15
2.5 Ta and Al sputter targets- and chamber at DESY 16
2.6 Laser pulse shapes of the optical laser at MEC 17
2.7 Experimental setup at MEC 18
2.8 Experimental setup at BL3:EH5 19
2.9 Quench product and Raman spectra of the cristobalite synthesis 21
2.10 DAC setup 22
2.11 DAC culets with sample 23
2.12 Model of the dDAC 23
2.13 Ramp profiles of the dDAC experimental runs 24
2.14 Photograph of the experimental setup of the P02.2 end-station at DESY . 24
2.15 3D images of the setup of the resistive heated dDAC 25
2.16 RHdDAC connected to the vacuum vessel 27
2.17 Photographs of the RHdDAC at P02.2 27
2.18 Schematic overview of the hydrocode target assembly 28
2.19 Representative result of a hydrodynamic simulation 29
2.20 Workflow of DFT-MD 31

2.21 Mean square displacement of a DFT-MD run 32

3.1 VISAR outlines of the shock drives with α-quartz 35
3.2 U_s - U_p relationship of shocked α-quartz 36
3.3 X-ray diffraction raw data images 37
3.4 Exemplary XRD raw images of a time series of shocked α-quartz at 45 GPa 38
3.5 XRD multiplot XRD data of shocked α-quartz 38
3.6 Diffraction refinement outlines 40
3.7 Results from hydrodynamic simulations on α-quartz 42
3.8 Hydrodynamic simulations of stishovite 44
3.9 VISAR image and outline of a stishovite experimental drive 45
3.10 U_s and U_p relationship of shock compressed stishovite 46
3.11 XRD multiplot of ambient and shock compressed stishovite 47
3.12 XRD outline of compressed stishovite at 301 GPa with theoretical high pressure SiO_2 phase Bragg reflections 48
3.13 Measured *d*-spacing of primary stishovite reflections 48
3.14 P-V/V_0 relationship of shock compressed stishovite 50
3.15 Unit-cell parameters of dynamically compressed stishovite with regard to pressure 53
3.16 Snapshots of the DFT-MD simulation of stishovite for the hydrostatic and non-hydrostatic case at 300 GPa. 54
3.17 VISAR image and outline of shock compressed GeO_2 55
3.18 XRD multiplot of shock compressed GeO_2 56
3.19 Structure factor S(Q) of GeO_2 at 53(9) GPa compared to literature data. . 58
3.20 Pair distribution functions of GeO_2 at various pressures 59
3.21 X-ray diffraction images of shock compressed α-quartz at various delay times 61
3.22 X-ray diffraction pattern of shock compressed α-quartz at various delay times at MEC and BL3:EH5 62
3.23 X-ray diffraction images of shock compressed α-cristobalite at various delay times 62
3.24 X-ray diffraction images of shock compressed fused silica at various delay times 63
3.25 X-ray diffraction pattern of shock compressed α-cristobalite and fused silica at various delay times at MEC 63
3.26 X-ray diffraction images of α-cristobalite, cristobalite II, cristobalite X-I and seifertite with corresponding Bragg reflections 64
3.27 Surface plot showing the effects of rapid compression of α-cristobalite in time-2θ space. 65

3.28 XRD pattern showing the evolution of dynamically compressed α-cristobalite 67
3.29 Molecular volume per formula unit of seifertite as a function of pressure. . 68
3.30 Volume strain with regard to pressure during decompression 69
3.31 XRD pattern demonstrating the evolution of resistive heated α-cristobalite 70
3.32 Molecular volume of seifertite as a function of pressure. 71
3.33 Molecular volume of cristobalite X-I as a function of pressure. 72
3.34 Structure of the ambient and high pressure polymorphs of α-cristobalite derived form DFT-MD 74
3.35 Density and structural evolution of α-cristobalite with regard to pressure from DFT-MD 74

4.1 Pressure-density plot of α-quartz shock wave data with experimental and literature data 76
4.2 Schematic model of shear band melting 77
4.3 P-ρ plot of shock compressed stishovite 78
4.4 SiO_2 phase diagram with experimental and literature data 79
4.5 Ge-O and Ge-Ge distances with regard to pressure 81
4.6 Germanium coordination number in shock compressed GeO_2 82
4.7 Shock hysteresis derived from hydrodynamic simulations 83
4.8 Experimentally determined average grain sizes as a function of delay time 84
4.9 Snapshot of DFT-MD simulations of liquid α-quartz and experimental and simulated XRD liquid scattering signal 85
4.10 Pressure versus compression rate for various dDAC experiments 88
4.11 Lattice parameter ratio *c*/*a* with regard to pressure 89
4.12 XRD outline of shock compressed fused silica 93
4.13 Summary of the high pressure polymorphism of SiO_2 with regard to compression techniques and starting material 97

List of Tables

3.1 U_p, U_s and peak pressures of shock compressed α-quartz 36
3.2 Calculated vs. observed d-spacing (Å) of the stishovite and *d*-NiAs structure in the experimental campaign on α-quartz 39
3.3 Unit cell parameters for stishovite and *d*-NiAs 41
3.4 Experimental results from shock compressed stishovite 44
3.5 Unit cell parameters of ambient and shock compressed stishovite 49
3.6 Fit parameters from refinement of shock compressed stishovite. 50
3.7 Comparison between obtained pressures of the experimental work to literature data and density functional theory. 51
3.8 Experimental pressure conditions and the results of the first (r1) and second (r2) peak positions of g(r) and the coordination number CN 59
3.9 Experimental run conditions and observations from XRD 60
3.10 Summary of the experimental conditions of the dDAC experiments on α-cristobalite 66

Chapter 1

Introduction

1.1 Mineralogy at Super-Earth interior conditions

1.1.1 Composition of Super-Earths

Since the first discovery of a planet orbiting a host star beyond our solar system in 1992 [1], more than 4290 other exoplanets have been confirmed up to date (as of October 8th, 2020). There has been a growing interest in the exoplanet survey missions of discovering low-mass planets with the goal of finding Earth analogues. Because of the development of new telescopes in the past years (e.g. the Kepler-, Spitzer- and TESS space telescopes), hundreds of so-called "Super-Earths" have been found. A Super-Earth is defined as a planet with a mass between 1-10 M_E and a corresponding radius in the range of 1-2.5 r_E [4, 5]. The most abundant population of exoplanets within the size range between Earth and Neptune are representing a novel planetary type with no direct analogues within our solar system [6, 7] and raise fundamental questions about the structure, dynamics and evolution of these terrestrial bodies. Super-Earths can encompass a wide range of compositions depending on their mass-radius relation [3], ranging from iron-rich Super-Mercuries and molten lava planets to water worlds with thick steamy envelopes, to planets enriched in carbon [8]. The compositional variety of Super-Earths are displayed in Figure 1.1. Here, the measured masses

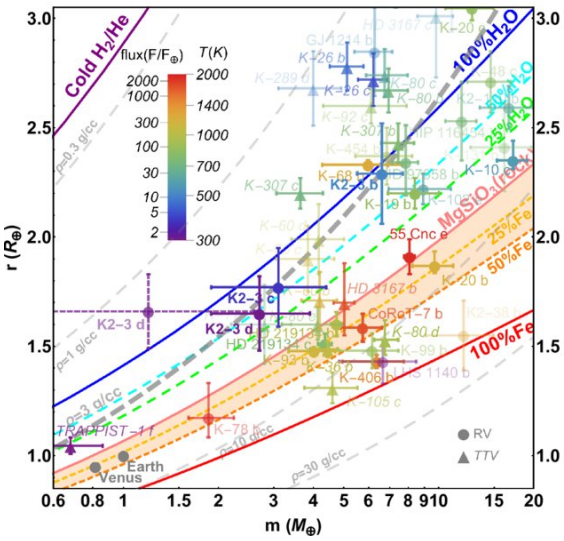

Figure 1.1: Mass-radius diagram for exoplanets for which the mass and radius have been measured combined with compositional trendlines. Modified after [2, 3].

and radii of exoplanets are put into correlation with theoretical mass-radius curves for different chemical compositions. It is evident, that numerous Super-Earths are of same or similar composition as Earth, with a rocky interior. The interior mineralogy plays an essential role for the fundamental question of habitability [9], including the composition of the atmosphere, existence of plate tectonics and the possibility of generating an internal magnetic field [8]. Measured densities of Super-Earths indicate a bulk composition, which is comparable to terrestrial planets of our solar system [6, 10]. Therefore one can model the mineralogy of these planets by assuming an Earth-like composition as a starting point, dominated by O, Fe, Mg and Si [11]. The interior of Earth consists of Mg-rich silicates and oxides within the mantle, overlying a metallic Fe core. The pressure and temperatures encompassed in planetary interiors are tremendous (Fig. 1.2). The silicate-rich mantle of the Earth reaches pressures of up to 135 GPa, within a depth of 2900 km and the core extends to 6371 km with pressures reaching up to 363 GPa. The temperatures within Earth range from ∼1500 K to 2500 K through the mantle and reach 6500 K at the center of the Earth. A terrestrial (rocky) Super-Earth (10 M_E) likely reaches more than 1 TPa at the base of its silicate mantle and up to 4 TPa at the center of the core [6, 12].
The mineralogy of Super-Earths depend on the composition of the mantle and core at respective pressures and temperatures. For terrestrial Super-Earths, simple oxides and silicates are of strong relevance and the properties of the end-member oxides such as MgO, FeO, $MgSiO_3$ and SiO_2 are of major importance to understand the solid solution, solubility and dissociation reactions in plausible mineral assemblages. At the P-T conditions of Super-Earth interiors, the phase relations of even those simple compositions are only starting to be explored and the lack of constrains on the physical and chemical properties of materials at extreme conditions limit the progress in the understanding of the evolution, inner structure and thermal behavior of these planets [6].

1.1.2 Crystal structure and phase transitions of silica and its structural polymorphs

One of the most abundant oxide component within the terrestrial mantles of Earth and Super-Earths is silica. Silica is a reference for a compound of silicon and oxygen (SiO_2), with both elements being the two most common elements on Earth (16 wt% and 30 wt%, respectively) [11]. SiO_2 is the dominant oxide constituent within the Earth's crust (60 wt%) and a major constituent of the Earth mantle, bonding with Fe and Mg to form the primary mineral phases. The reason for the high abundance of SiO_2 within the Earth's mantle is the significantly stronger Si-O bond (466 kJ/mol) in contrast to any other element bonding with oxygen [13]. Free SiO_2 within the Earth's mantle is only expected in localized regions such as subducted oceanic crust, however within the wide range of P-T conditions in Super-Earths, a variety of possible SiO_2 compositions and a large range

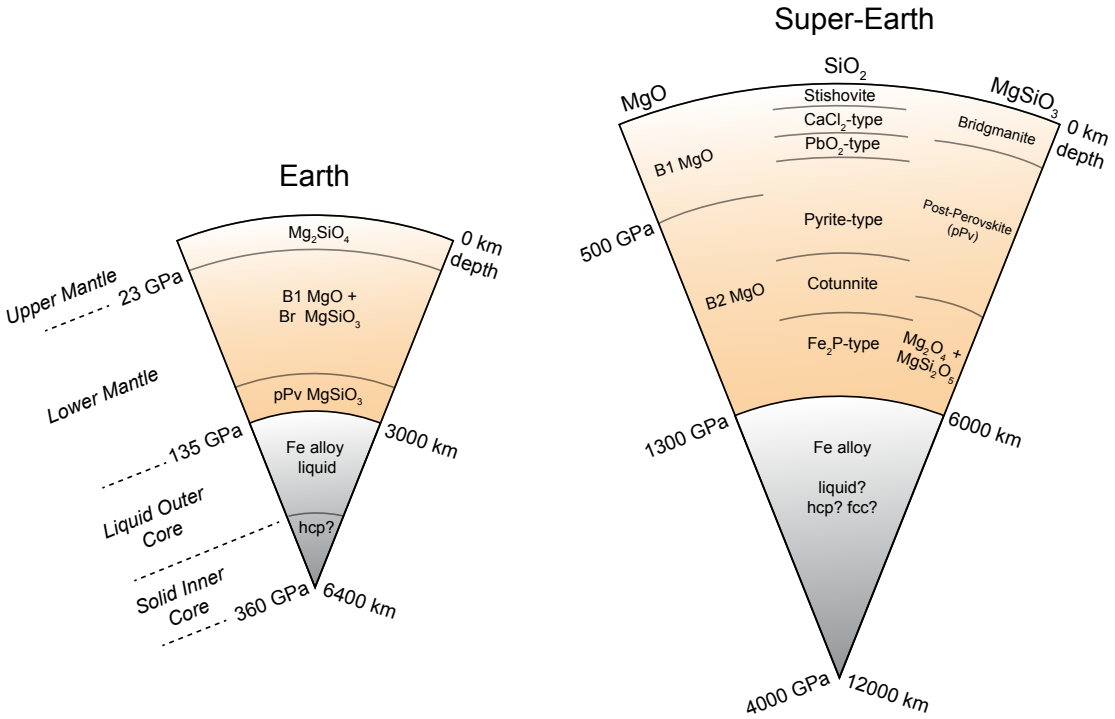

Figure 1.2: Schematic overview of the interior pressure conditions and expected mineral phases in the MgO-SiO_2 system within the Earth and a representative Super-Earth (10 M_E). Modified after [6].

of silica phases are expected [8]. Within the mantle of these planets, silicate phases are likely to be affected by a high structural complexity manifested by prolific polymorphism of SiO_2 and its disproportionation might produce silica-rich regions within the deep end of the Super-Earth's mantle [8].

Under steady state equilibrium conditions, SiO_2 undergoes a well known sequence of phase transitions towards high pressures. Low- or **α-quartz** transforms to the monoclinic coesite structure (Space group *C2/c*) at ∼2 GPa [14, 15] and further crystallizes in the rutile-type structure ($P4_2/mnm$) as stishovite, consisting of octahedrally coordinated Si atoms (Fig. 1.3) [16, 17, 18]. At ∼60 GPa, stishovite undergoes an orthorhombic distortion and displacively transforms to a $CaCl_2$-type structure (*Pnnm*) [19, 20, 21, 22, 23, 24, 25] and seismic discontinuities observed in the mid-lower mantle of Earth (1000-1600 km), for instance, are associated to this phase transition [22, 23]. A further transition to the α-PbO_2 type (seifertite) structure (*Pbcn*) occurs at ∼121 GPa [25, 26, 27, 28, 29, 30, 31]. To date, the highest-pressure experimentally determined SiO_2 phase transformation is to the pyrite-type structure ($Pa\bar{3}$) at around 268 GPa [32]. By using silica glass (**fused silica**) as the starting material, a high pressure transformation towards the rutile structure at ∼10 GPa and to a metastable, monoclinic defective niccolite structure (*d*-NiAs) has been observed at pressures between 30-55 GPa (and 1000-1300 K)

[31]. At pressures exceeding 55 GPa, the $CaCl_2$ structure was shown [21, 22, 23, 24, 25]. Furthermore, numerous studies under static conditions have directly investigated **stishovite** as the starting material for high pressure research due to its strong relevance in planetary science [19, 20, 24, 33, 34, 35, 36, 37, 38]. Stishovite was found in terrestrial impact-related rocks, as well as in shocked meteorites and is likely a dominant phase in free SiO_2 regions within the upper mantle in depth of up to ∼300 km. Similar to α-quartz, it was demonstrated, that stishovite transforms to the $CaCl_2$ structure at ∼60 GPa [20, 38]. However no other phase transitions using stishovite as the starting material has been found at pressures of up to 128 GPa.

At ambient pressures and at temperatures above 1470 °C, the SiO_2 polymorph **α-cristobalite** ($P4_12_12$) forms. It has a subordinate and rather exotic terrestrial occurrence, compared to α-quartz or stishovite, but its high pressure behavior is of great interest to geological studies, since it has been observed in meteorites in close spatial association with high pressure mineral assemblages [39, 40, 41, 42]. α-Cristobalite has been observed in low shocked meteorites [39, 43] but also in meteorites, that show signatures of peak shock pressures exceeding 25 GPa alongside seifertite, the post-stishovite high-pressure polymorph of SiO_2 (”seifertite puzzle”) [40, 41, 42]. According to these studies, α-cristobalite seems to be stable at variable pressure conditions and its phase relations show complex behavior. Under hydrostatic conditions it was shown, that α-cristobalite undergoes a transformational sequence from tetragonal α-cristobalite towards monoclinic cristobalite II ($P2_1/c$) at ∼1.5 GPa and to monoclinic cristobalite X-I ($P2_1/n$) at ∼11 GPa [28, 31, 44]. Using α-cristobalite powder as a starting material, a further transformation towards the orthorhombic seifertite structure at ∼35 GPa was found [45]. These studies provide evidence that seifertite can form at pressures much lower than expected from its thermodynamic equilibrium at ∼121 GPa [46]. Using single crystal α-cristobalite, the transformation pathways towards cristobalite II and cristobalite X-I are observed as well [47], but a further transformation to seifertite even at pressures of up to 80 GPa has not been found [46].

Although it is not a polymorph of SiO_2, the inorganic compound **GeO_2** holds great importance to planetary and high-pressure science due to its structural similarity to α-quartz. Furthermore, it is commonly used in X-ray diffraction experiments because, as a material with a large atomic number, high diffracted X-ray intensities can be expected. GeO_2 exhibits three different polymorphs: α-quartz-type GeO_2, vitreous GeO_2 and rutile-type GeO_2. In static experiments at room temperatures it was shown, that α-quartz-type GeO_2 transforms to a poorly crystalline monoclinic structure ($P2_1/c$) up to at least 52 GPa [31, 48]. At elevated temperatures (1200-1600 K), a pressure-temperature induced transformation of GeO_2 has been observed towards the rutile structure at ∼7 GPa and to the $CaCl_2$ structure at 26 GPa [31]. When starting from vitreous GeO_2, a phase transformation towards a 6-coordinated glass at ∼23 GPa [49] and a phase transformation to the

defective niccolite structure at 25 GPa can be observed [50]. Ultimately, starting with the rutile-type GeO_2, a phase transformation towards the $CaCl_2$ structure at 26 GPa has been found [31].

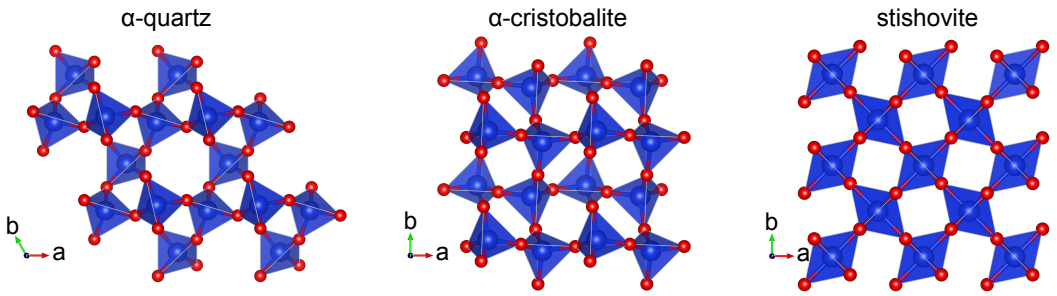

Figure 1.3: Polyhedral representation of α-quartz, α-cristobalite and stishovite. The structures are viewed along the c axis at ambient conditions with the large spheres representing the Si atoms and the small ones the O atoms.

1.2 Theoretical and experimental approaches for high-pressure research

Understanding the structural evolution of materials, such as silicates, at pressures and temperatures comparable to Super-Earth interior conditions, requires several theoretical and experimental approaches. These methods are often complementing each other and give constrains to structural transitions at high pressures and temperatures. The results of an experiment require theoretical confirmation by means of e.g. *ab initio* quantum mechanical simulations. Here, a short overview of theoretical models and the development of high pressure techniques at X-ray sources are presented.

1.2.1 Theoretical models

Planetary materials such as silica are studied by means of density functional theory (DFT) and molecular dynamics (MD) simulations, which use the many-body Schrödinger equation. This method is based on the properties of electrons and nuclei rather on empirically determined parameters. To solve these equations, one has to rely on approximations, which are well tested for a wide range of materials and conditions and the accuracy of e.g. the local density approximation (LDA) or generalized gradient approximation (GGA) have been shown to be typically 1-2% for bond lengths and unit cell dimensions, 5% for vibrational frequencies and 15% for elastic constants [51]. The DFT simulations have been extensively tested against experiments at lower pressures and its success and limitations are therefore well established [8]. For solids which are investigated by means of

temperature, molecular dynamics are often used to sample phase space. Within the MD approach, ions are moved according to the Newton's equation of motion in which each atom has a mass, a velocity and a force acting upon it. Here, the solution of the equation of motion [52] can be approximated with the use of small time steps (e.g., $<$1/20th of a vibrational period). The combination of density functional theory and molecular dynamics are an essential tool for providing information on dynamics which are used to demonstrate electrical and transport properties, as well as diffusion behavior and viscosities in planetary materials. Several approaches have been pursued to explore the phase diagram of silica, and phase transition as well as melting have been thoroughly investigated (e.g. [53, 54, 55, 56, 57, 58, 59, 60, 61]). The results of the simulated phase relations are used, to further constrain the interior and evolution of exoplanets [62, 63].

1.2.2 Experimental techniques

Advances of static and dynamic compression techniques

Within the past century, a wide range of experimental techniques have explored material properties at high pressures and temperatures. The technical capabilities to reach extreme P-T conditions have increased drastically from first static compression achieved with the use of tungsten carbide cells by Bridgman in the mid-1930s [64], to the first diamond anvil cell (DAC) in the late 1950s [65, 66, 67]. In a DAC experiment, a small ($\sim$10-100 µm) sample is compressed between two diamonds [8] and can be heated using laser or resistive heating techniques. Recent developments to improve conventional anvils led to a enormous enhancement of the DAC, resulting in static pressures approaching a terapascal (TPa) at room temperature. This was made possible through the microfabrication of toroidal [68, 69] and double-stage anvils [70]. Furthermore, the so-called dynamic DAC (dDAC) was developed [71] which represents a bridge between static and dynamic (shock) compression. Here, electromechanical actuators apply a load, which produces a tailored time-dependent pressure profile on the investigated material. From initial compression rates of 500 GPa/s in 2007 [71], an increase of up to 160 TPa/s has been demonstrated recently [72]. Static (and semi-dynamic) compression studies can

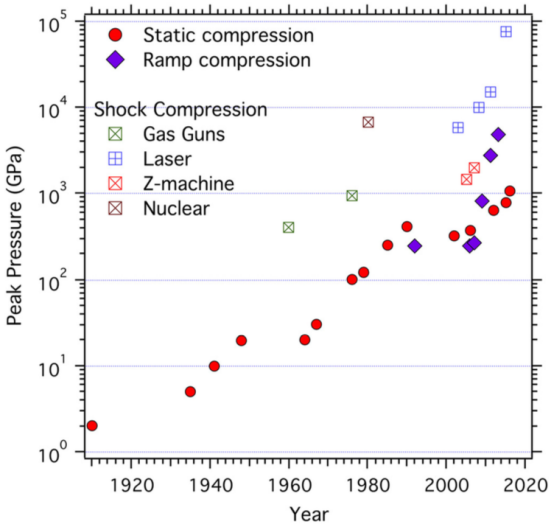

Figure 1.4: Peak pressures (GPa) achieved by various compression techniques as a function of year. Modified after [8].

achieve pressures of several hundreds of gigapascals and are almost always based on the use of multi-anvil presses or (d)DACs. To reach pressures within the terapascal range and temperatures of up to 10000 K or more, however, one needs to rely on dynamic-loading techniques. These include shock and ramp compression, which involve loading durations of nano- to microseconds. Historically, dynamic compression was primarily conducted with the use of gas-guns. A gas-gun can accelerate a flyer plate to several km/s, which generates a shock wave by impacting a sample, leading to immense pressures and temperatures. In the recent decades, however, high-powered lasers and pulsed power drivers are emerging. In a laser shock experiment, the surface of a material is ablated through the irradiance of a short ($\sim$ns) intense laser pulse, which creates a shock wave propagating through the sample. Within these short timescales, pressures and temperatures can reach several tens of thousands of Kelvin and several terapascals [73]. The first demonstrations of strong shock waves with lasers were conducted at large laser facilities, emerging in the 1970s [74]. Through the advances in laser interferometry diagnostics, a precise description of shock wave profile measurements under laser compression was possible [75]. The dynamic compression techniques have undergone rapid development in the last decade, greatly extending the accessible conditions and types of measurements that can be performed. A general overview on the historical evolution of pressures achieved in laboratory experiments with various compression techniques is shown in Figure 1.4.

Advances of high pressure research at X-ray radiation sources

X-rays have been recognized for their exceptional importance since their discovery in 1895 by Röntgen (which led to him being awarded the first Nobel Prize in physics in 1901). In 1897 Larmor derived an expression from classical electrodynamics for the instantaneous total power radiated by an accelerated charged particle, which Liénard extended the following year to a relativistic particle undergoing centripetal acceleration in an circular trajectory. Here, radiated power was shown to be proportional to $(E/mc^2)^4/R^2$, with E being the particle energy, m the rest mass and R the radius of the trajectory [76]. The principle of the energy-loss mechanism was then used in the 1940s for magnetic-induction electron accelerators (betatrons) as machines to produce intense beams of X-rays by directing the accelerated beam to a suitable target [77]. A following trend towards higher energies and shorter wavelengths of synchrotron radiation led, for instance, to the 6 GeV Deutsches Elektronen-Synchrotron (DESY) in Hamburg, which began operating for both high-energy physics and synchrotron radiation in 1964 [76]. To take maximum advantage of the brightness of a synchrotron radiation source, undulators and wigglers were developed, implemented and retrofitted into storage rings. Undulators and wigglers are similar in setup, by being an array of closely spaced, vertically oriented dipole magnets of alternating polarity. The trajectory of an electron beam oscillates in the horizontal plane during passing between two of these magnetic arrays and radiation cones are emit-

ted. Electron emission is present at each bend in the trajectory overlap, which leads to constructive interference resulting in one or a few spectrally narrow peaks (a fundamental and harmonics) in a beam that is highly collimated in both the horizontal and vertical directions, resulting in a high spectral brightness. The wavelengths can be tuned by mechanically adjusting the vertical spacing between the pole tips.
Soon it was apparent, that a third generation of storage rings with a still lower emittance and long straight sections for undulators would permit achieving even higher brightness and with it, a considerable degree of spatial coherence [76]. The third generation facilities optimized for brightness in either the short-wavelength regime (high-energy or hard X-rays) or vacuum ultraviolet and long-wavelength regime (low-energy or soft X-rays). The European Synchrotron Radiation Facility (ESRF) in Grenoble was the first third-generation hard X-ray source with a 6 GeV storage ring coming online in 1994. This was followed by the Advanced Photon Source at Argonne National Laboratory (7 GeV) and PETRAIII at DESY (19 GeV) [76]. Combining pressure vessels such as a diamond anvil cell (DAC) or large volume press with synchrotron beamlines, subsequently enabled *in-situ* XRD measurements under high pressure [78, 79]. For DAC experiments, synchrotrons are ideal, because X-ray radiation easily passes the transparent diamonds and the X-ray beam can be focused down to micrometer spots. The sample between the diamonds is compressed to pressures of up to several hundreds of gigapascals while being heated resistivitly or with a laser system to several thousands of Kelvin [80]. This made the investigation of planetary materials under *in-situ* conditions possible and various studies with the DAC at synchrotrons have been conducted so far (e.g.[81, 82, 83, 84, 85, 86, 87]). Further, a few experiments with a dynamic DAC have been conducted recently at synchrotrons on planetary material, making use of the fast compression rates while being probed by hard X-ray synchrotron radiation [88, 89, 90].

In parallel with the development of accelerator-based X-ray sources, a growing interest in the field of ultrafast science emerged over the past 40 years. Combining the advanced femtosecond lasers with conventional synchrotron-based X-ray sources has enabled the generation of broadly tuneable femtosecond X-rays with the use of laser manipulation of the relativistic electron beam [91, 92, 93]. The most promising development in ultra-fast X-ray sources has been the emergence of X-ray free-electron lasers (XFELs) which have sparked another revolution in X-ray science in the twenty-first century [94]. The free-electron lasers (FELs) were invented by Madey [95] at Stanford University in the 1970s [96]. Here, relativistic electrons propagating through an undulator generate and amplify coherent electromagnetic radiation. By passing the long FEL undulator, the initial random spontaneously emitted radiation of the relativistic electrons are amplified by the bright electron beam. This self-amplified spontaneous emission (SASE)

process can generate multi-gigawatt (GW) and femtosecond (fs) quasi-coherent radiation in the X-ray wavelength range (from a few nanometers to less than 1 Å). Peak brightness can therefore be enhanced dramatically compared to synchrotron radiation, through the use of high power and excellent transverse coherence. The first facilities to make use of the FEL radiation were the FLASH facility at DESY in Hamburg in 2005 (soft X-ray radiation) [97] and the Linac Coherent Light Source (LCLS) facility at SLAC in 2009 (hard X-ray radiation) [98], followed by the SACLA facility in Japan (2011) [99]. An example of the high brilliance of XFELs compared to synchrotron radiation is shown in Figure 1.5. Here, α-cristobalite was investigated by means of synchrotron radiation at the PETRAIII X-ray light source of DESY and at the SACLA X-ray free electron laser. The intensity of X-ray Bragg reflections from SACLA is around 7 times higher compared to PETRAIII, but accumulated only within 7 fs, compared to 20 s at PETRAIII (it should be noted, however, that at PETRAIII the sample was compressed between a DAC, which decreases the signal of the sample to some extent).

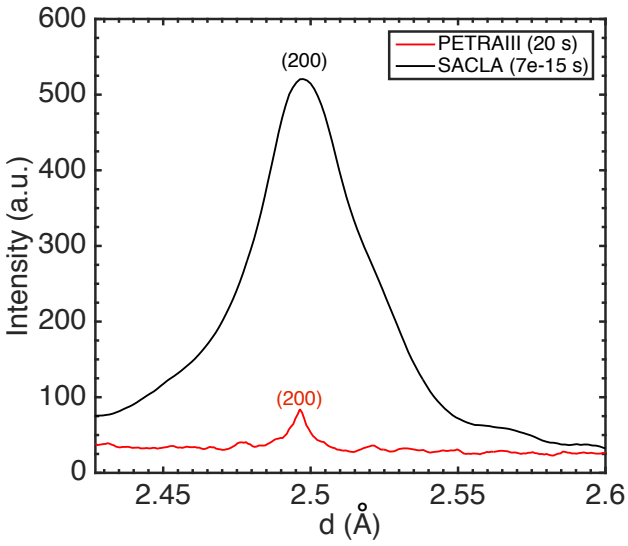

Figure 1.5: (200) Bragg reflection of α-cristobalite at PETRAIII (within a DAC) and SACLA (as a direct target) from this work. Accumulated X-ray penetration time is indicated.

With the implementation of optical laser systems at the LCLS, SACLA and the European XFEL (foreseen in 2020), structural information of the dynamic response of material under shock compression with the concomitant use of femtosecond X-ray pulses can be obtained, and various studies have already investigated planetary materials such as silicates, hydrocarbons or water (e.g. [100, 101, 102, 103, 104]). The investigation of dynamic compression of geological materials at ultra-high pressures with the use of XFEL radiation is, however, still in its infancy and will likely be one of the primary high pressure research challenges in the next decade.

1.3 Motivation and aim of this study

As one of the most important planetary compounds, silica is widely investigated by means of high pressure techniques at pressure and temperature conditions comparable to the interior of Earth. In static experiments, silica was shown to undergo several high pressure

and high temperature phase transitions and the phase relations of silica within the mantle of Earth are well understood. The equation of state for silica at pressures corresponding to P-T conditions of Super-Earths has been thoroughly investigated through dynamic compression techniques, however, structural and melting properties on the atomic level have not been studied so far, due to experimental limitations such as the lack of X-ray diagnostics. Recently, the emergence of optical laser systems at synchrotron radiation sources and XFELs has enabled reaching P-T conditions comparable to Super-Earth interior conditions, and to constrain the structural evolution of silica at ultra-high pressures. Up to date, the only structural information on the silica shock Hugoniot is from α-quartz and fused silica up to 67 GPa, but other modifications such as stishovite or α-cristobalite have not been investigated on the atomic level at all. A detailed comparative study of the high pressure pathways of silica under dynamic compression is needed, in particular in light of its immense geophysical importance for planetary structures and dynamics at high pressures, as well as impact phenomena. Furthermore, it has been shown, that the dynamic response of materials are deviating strongly from equilibrium behavior [105, 106] and it is crucial to investigate the effect of fast compression rates on the phase transition kinetics of silica, especially concerning the validity in comparing the SiO_2 steady state phase diagram to results from dynamic compression experiments. Moreover, the compression with a laser or gas-gun is accompanied by large deviatoric stress. This uniaxial compression might lead to the shifting of phase transition boundaries to larger pressures, compared to hydrostatic equilibrium data [107]. Ultimately, melting properties of planetary materials, such as silica, play an essential role for planetary dynamics. As the liquid outer core is responsible for the electromagnetic field around Earth, dissociated silicate melts might also contribute to the dynamo generation [108]. Therefore, there is a great interest in investigating silicate melts on the atomic scale at pressures corresponding to lower mantle conditions. Furthermore, recrystallization effects from these melts can constrain pressure and temperature conditions of other geophysical events, such as meteor impacts.
In the present study, silica and its polymorphs were investigated by dynamic compression in a variable P-T regime with the concomitant use of hard X-rays of synchrotron- and XFEL radiation sources. Firstly, α-quartz, fused silica, α-cristobalite and stishovite as well as GeO_2 were compressed along their respective Hugoniot with the use of laser induced shock compression at the LCLS and SACLA free electron laser sources. Secondly, α-cristobalite was dynamically compressed with the use of the (resistive heated) dDAC at PETRAIII. The first approach targets the high pressure shock response on the lattice level, including high pressure transitions and melting, whereas the second approach quantifies the relation between compression rate and the phase transition pressure onset at variable hydrostatic conditions. Ultimately, both approaches were complemented by hydrodynamic- and DFT-MD simulations to consolidate the experimental results.

Chapter 2

Material and Methods

This chapter emphasizes on the methodological and experimental approach for studying planetary materials with the use of laser shock compression and dynamic diamond anvil cell techniques at synchrotron radiation- and XFEL light sources. Sample preparation for shock compression experiments, including target synthesis with the use of a large volume press and the experimental setup of the MEC and BL3:EH5 end-stations at the Linac Coherent Light Source (LCLS) and SPring-8 Angstrom Compact free electron LAser (SACLA), respectively, are described in chapter 2.1. Chapter 2.2 will illustrate sample synthesis and preparation for the dynamic diamond anvil cell experiments as well as the detailed setup of the experiments at PETRAIII. Ultimately, computational simulations which were performed to constrain experimental parameters and benchmark results are described in chapter 2.3. These include hydrodynamic-, density functional theory and molecular dynamics simulations.

2.1 Laser induced shock compression

2.1.1 Sample preparation and sample synthesis

In this work, commercial and synthesized sample material was used to investigate the high-pressure behavior of silicates and GeO_2 during shock compression. In order to compare and validate the equilibrium phase diagram of SiO_2 to shock data, several silica polymorphs were chosen as starting material for the shock compression experiments. These include crystalline SiO_2 (α-quartz), amorphous SiO_2 (fused silica) and the high-temperature and high-pressure SiO_2 polymorphs α-cristobalite and stishovite, respectively. Furthermore, GeO_2 was investigated to elucidate high pressure phase transitions and melt properties, including bonding structure and coordination.

Single crystal c-cut α-quartz samples were provided by VM-TIM (Jena, Germany) and HEBO-Spezialglas (Aalen, Germany) as transparent windows with a thickness of 35 µm,

30 µm and 15 µm, respectively. Sample dimensions varied, depending on the experimental setup: α-quartz windows for experiments at LCLS were 2 × 3 mm in size, each fitting precisely on top of the cone shaped holes of the MEC sample holder (Fig. 2.1a) whereas at SACLA, samples were cut to 5 × 5 mm windows, to fit onto the notches of the respective sample holder (Fig. 2.1b). Initial density of α-quartz was 2.65 g/cm^3 (as per supplier's specifications). Samples were optical grade, double sided polished and furthermore anti-reflection (AR)-coated for a wavelength range of λ = 527 - 532 nm. The AR coating was used to avoid reflections ("ghost fringes") at the rear surface of the samples while using the velocity interferometry system for any reflector (VISAR) (see chapter 2.1.2).

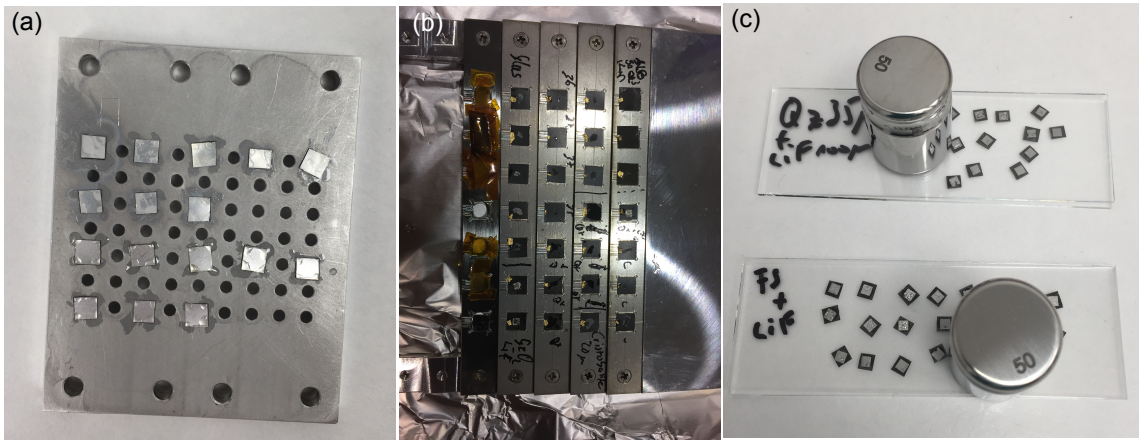

Figure 2.1: Photographs of (a) targets on a sample holder at MEC and (b) at BL3:EH5. Furthermore shown are (c) target assemblies on glass slides compressed by weights.

Apart from crystalline α-quartz, fused silica was investigated, which was provided by Corning Inc (Corning, USA) as 2 × 3 × 0.2 cm thick glass slides. As per supplier's specifications, samples contained no impurities and initial density was 2.2 g/cm^3. Glass slides were polished down to 35 µm in thickness by using SiC sandpaper (P400-P1200) and cut to 2 × 3 mm large windows with a diamond string blade.

The SiO_2 high-temperature polymorph α-cristobalite was provided as natural crystals embedded in volcanic glass (Colima volcanic complex, Jalisco, Mexico). α-Cristobalite pieces were separated from several globules within the volcanic glass and polished with SiC sandpaper (P1200) to 20 µm thick pieces, each cut to 2 × 3 mm windows.

The SiO_2 high-pressure polymorph stishovite was synthesized using the large volume press (LVP), housed at the PETRAIII end-station P61B at the German Electron Synchrotron DESY. Cylindrical rods of fused silica (Goodfellow GmbH) with a diameter of 2.5 mm were cut and polished (SiC sandpaper, P400-P1200) to 3 mm in height, subsequently cleaned with acetone in an ultrasonic bath and placed into a Pt-capsule.

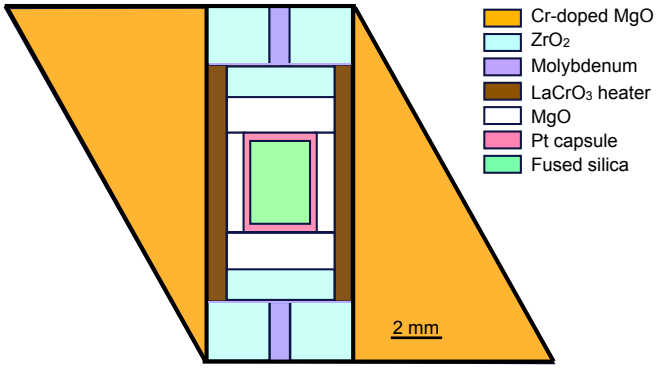

Figure 2.2: Cross section of the large volume press cell assembly with various components and fused silica as starting material used for the synthesis of polycrystalline stishovite.

The capsule and two Pt lids had been cut from Pt foil (Alfa Aesar) and were subsequently cleaned and folded. The capsule was placed into an MgO gasket (4 mm in diameter), which had been polished to 3.3 mm in height (SiC sandpaper, P800), cleaned with acetone and put into a high temperature oven at 1000 °C for one hour. Two 2.6 mm thick MgO spacer, and additionally two 0.8 mm thick ZrO_2 lids (each 4 mm in diameter) were placed on top and bottom of the MgO gasket. The assembly was then put into a cylindrical $LaCrO_3$ rod, which served as a heater during the experiment. The $LaCrO_3$ cylinder was cut to 6 mm in diameter with the use of a razorblade and subsequently perforated with a 4 mm drill. Ultimately, the $LaCrO_3$ furnace was cut and polished (SiC sandpaper, P400) to 10 mm in height. 25 µm thick molybdenum foil (6 mm in diameter) served as a conductor and was put on top and bottom of the furnace. Two ZrO_2 lids (2.25 mm thick and 6 mm in diameter), each perforated with a one millimeter Mo rod, were put on top and bottom of the Mo lids. The assembly was then placed into an 18 mm edge length Cr_2O_3-doped MgO octahedron (Fig. 2.2). The octahedron was put into the center of eight WC-cubes with a truncation of 10 mm and subsequently compressed in the LVP (Fig. 2.3). The octahedral assembly was heated to 1500 °C for one hour after being compressed to a maximum pressure of 12 GPa. Pressure was calibrated at room temperature using the semiconductor to metal transition of ZnTe at 9.6 GPa and 12 GPa. Sample temperatures were estimated through power-temperature relations calibrated in a separate run using a W5%Re/W26%Re thermocouple (C-type). The experimental run product was cut out of the compressed assembly and the stishovite cylinder (Fig. 2.3) was dissected to approximately three pieces (each $\sim$300 µm thick) with the use of a diamond saw. The pieces were then polished with SiC sandpaper (P400-P1200) to 35 $\pm$1 µm thick windows.

The synthesized products were translucent with no visible cracks or impurities. The run products were analyzed with a bench-top X-Ray diffractometer (Europe 600, GNR Analytical Instrument Group) at the P61B end-station (Cu - Kα; λ = 1.5419 Å). X-ray diffraction of the products confirmed the pure stishovite phase composition (Fig. 2.4).

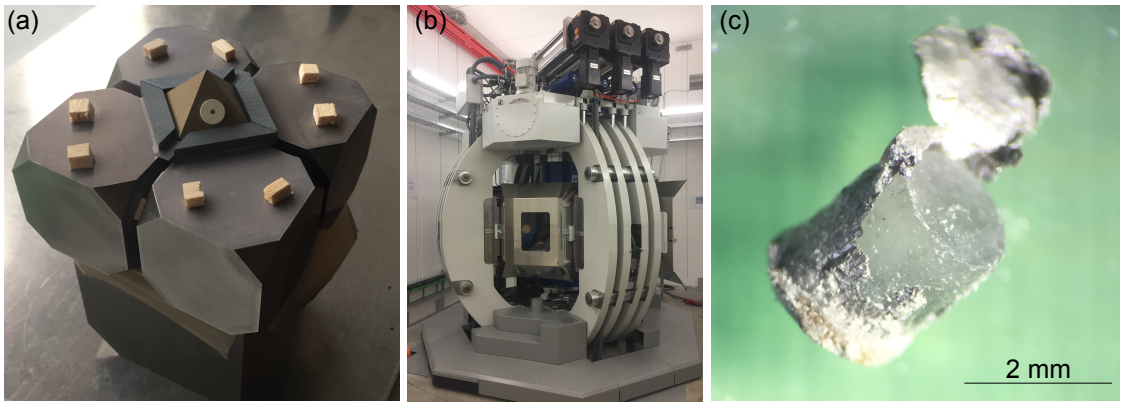

Figure 2.3: Photographs of (a) the cell assembly octahedron surrounded by four WC anvils. Shown are furthermore the wood spacer on top of the anvils as well as spacers between the gaps of octahedron and the anvils. (b) The large volume press at the P61B end-station at DESY. (c) Polycrystalline stishovite sample enclosed in an opened Pt capsule.

Grain size of stishovite was determined through XRD with the commonly used Scherrer equation [109]

$$\tau = \frac{K\lambda}{\beta \cos\theta} \tag{2.1}$$

with τ = grain size, K = shape factor (commonly set to 0.94), λ = X-ray wavelength, β equals the line broadening at full width at half maximum (FWHM) corrected of the instrumental broadening and θ = Bragg angle. Typical average grain size of the synthesized samples was ∼0.52(2) µm.

GeO_2 targets were prepared by mixing 10 wt% GeO_2 powder (Sigma-Aldrich Chemie GmbH, 99.999 % purity, density = 4.23 g/cm^3) with epoxy resin (Double Bubble, Loctite, Henkel Corp). The slurry was mixed for approximately 20 minutes, then equally distributed on polyimide foil (Kapton CB, DuPont de Nemours, Inc) with the use of a wooden stick and subsequently dried for 24 hours. Thickness of the slurry was measured by using a micrometer device and was accounted to 35 ± 4 µm. The GeO_2 coated polyimide foil was ultimately cut into 2 × 3 mm sized pieces.

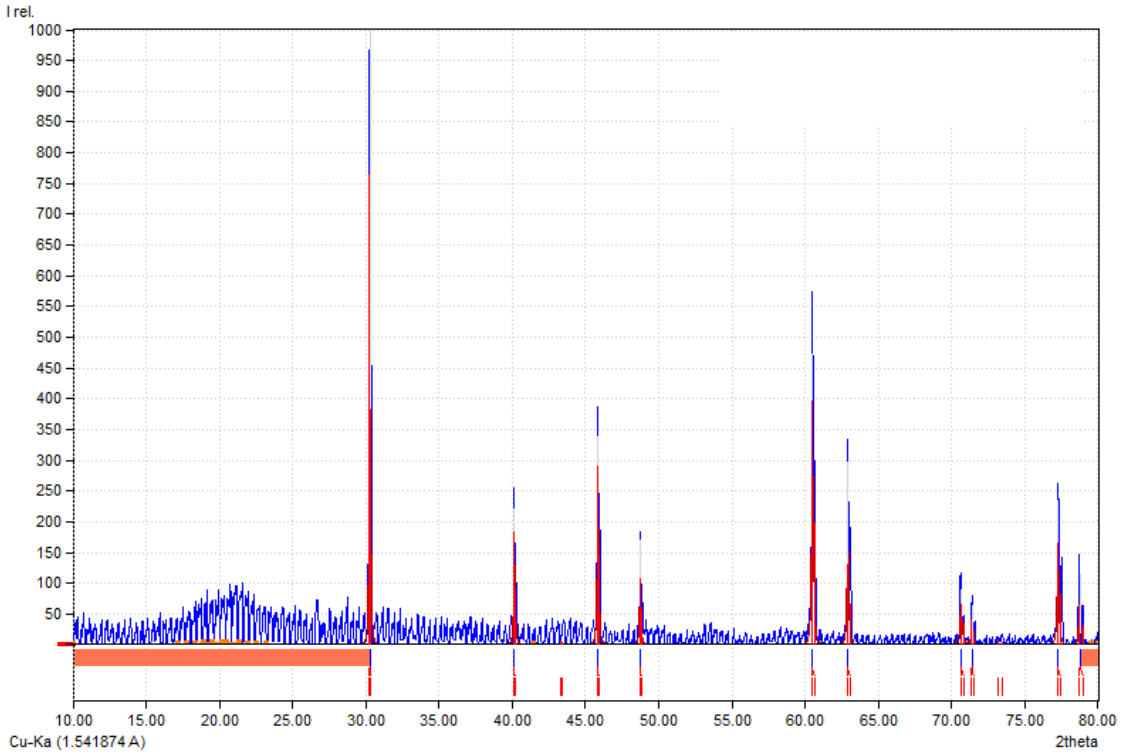

Figure 2.4: X-ray diffraction pattern of the stishovite synthesis product. Shown are the experimental XRD pattern (blue), the background (orange) and a best phase fit (red). The XRD pattern confirmed the pure stishovite composition of the synthesis product.

2.1.2 Experimental setup at MEC and BL3:EH5

A typical laser shock experiment at an XFEL source is carried out by launching a smooth, well defined optical laser pulse onto a target surface while simultaneously probing with the highly brilliant and coherent X-rays at a given time delay. To investigate the time-depending evolution of the structural changes of the samples during shock compression and release, sample dimensions and laser irradiation conditions were held constant during a series of shots. Here, probing with the FEL was systematically varied over time with regard to the shock breakout of the target, which lead to the determination of the structural changes across a range of P, T, ρ paths. The targets are usually built up in a sequence of (i) a plastic ablator at the front end, (ii) the sample and (iii) for ∼20 % of the runs a pressure window at the rear end of the assembly. The ablator consists typically of 50 µm polymide film (Kapton CB, DuPont de Nemours, Inc), which was glued onto the sample with ∼1-3 µm thick two component epoxy resin (Double Bubble, Loctite, Henkel Corp). The kapton film was coated with aluminum to insure sufficient coupling of the laser into the assembly.

Some experiments were furthermore conducted using a 22 µm thick CH coating instead of the kapton film, which was applied directly onto the sample using a sputtering device at the Institut De Minéralogie, De Physique Des Matériaux Et De Cosmochimie (IMPMC),

France. This was done to circumvent the use of epoxy between the kapton and the sample, which always holds an uncertainty in thickness and subsequently makes the analysis more difficult.

To measure the temporal and spatial evolution of the compression wave in the sample, a Velocity Interferometer for Any System (VISAR) was used to detect the Doppler shift of reflected laser light (532 nm) at the sample/pressure window interface. Two VISAR legs with different velocity sensitivities were employed to resolve ambiguities associated with sharp velocity jumps that exceed the time response of the system. By inserting different lengths of fused silica etalons in one leg of the interferometer, it is possible to alter the optical delay in that leg, which was used to control the velocity sensitivity of the interference fringes.

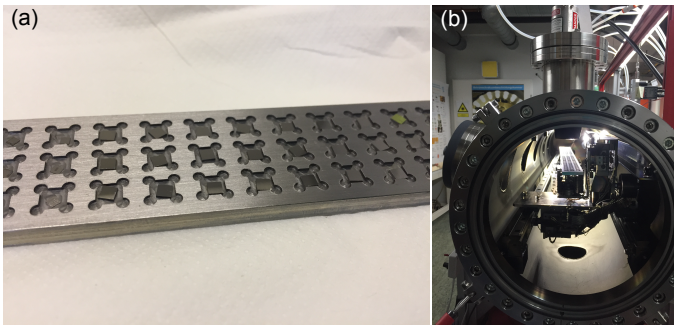

Figure 2.5: Photographs of (a) the sputter sample holder with Ta coated target windows and (b) the sputter chamber with sample holder hosted at the Magnetism and Coherent Phenomena Group at DESY.

The pressure windows for the VISAR were chosen according to the expected pressures, impedance, opacities and densities, achieved during compression. For the shock experiments it was crucial, that the impedance of the pressure window and the sample closely matched. A reference- and sample material mismatch will result in the shock wave resolving into a transmitting shock and a reflective wave directed back into the standard material. Is the impedance of the sample lower than that of the pressure window, the reflected wave will be a rarefaction and the standard will undergo an isentropic release. Is the impedance of the sample higher, the reflected wave is a shock and the pressure window will undergo further shock compression [110].

For most of the experiments, 100 µm and 500 µm LiF windows (courtesy of Los Alamos National Lab) were used, because of the similar impedance values to the silica samples. For higher pressure experiments (above 120 GPa), predominately 25 µm and 125 µm thick Al_2O_3 (HEBO Spezialglas, Aalen) and 100 µm thick MgO windows were applied (courtesy of Lawrence Livermore National Laboratory), because transparency of the LiF windows was decreasing, which made the analysis of the VISAR images increasingly difficult.

All pressure windows were coated with a 100 nm thick tantalum layer with the use of a sputter chamber hosted at the Magnetism and Coherent Phenomena Group at DESY (Fig. 2.5). The Ta layer was used as a reflectivity surface for the VISAR system and was

chosen because its diffraction patterns were easily distinguished from the samples. To prevent an alteration of the timing of the shock wave in the sample, a thin glue layer between ablator, target and pressure window had to be ensured. The assembly was therefore tightened together between two glass slides with weights on top (Fig. 2.1c). The targets were subsequently glued on the target holder of each experimental platform with a small line of epoxy which was applied with the tip of a string of hair.

The Matter in Extreme Conditions (MEC) end-station at the LCLS

Laser induced dynamic shock compression experiments on α-quartz, fused silica, stishovite and GeO_2 were conducted at the Linac Coherent Light Source, USA, at the Matter in Extreme Conditions (MEC) end-station. MEC is equipped with an optical- and VISAR laser system, used for shock compression experiments. A detailed description of the MEC experimental platform can be found in Ref. [111]. The MEC end-station holds a target chamber with target holder, laser- and XFEL optics and detector setup. Experiments at MEC were carried out in transmission Debye-Scherrer geometry with dual drive laser beams incident on the sample at 15° and the XFEL beam at 30° incident to the target normal. The dynamic compression of the target assembly was conducted using the long pulse output from the frequency-doubled Nd-YAG MEC laser system, which operated with two 527 nm beams, typically in a power-limited mode ($\sim$1.5 GW) within a temporally-shaped 10-20 ns pulse. The fine-tuning of the laser energy was achieved with the adjustment of waveplates within the beamline. Furthermore, each beam required a post-shot 7 minute laser amplifier cool down period, resulting in alternating successive shots to sample delivery every 3.5 minutes. For the experiments, the drive laser was focused to a spot diameter of 250 µm with the use of phase plates, which resulted in a smooth ablatively-driven shock-compression wave traveling through the target assembly. Maximum laser energies of 62 J were achieved, resulting in a total maximum laser intensity of $\sim$ 6.3 TW/cm^2. At MEC, etalon lengths of 25.036 mm and 11.006 mm were used, which produced a velocity-per-fringe (VPF) sensi-

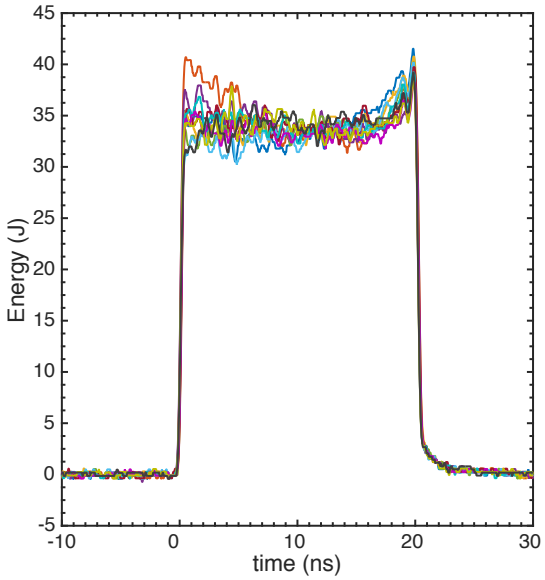

Figure 2.6: Ten representative laser pulse shapes for a conducted time series with the use of the Nd:glass optical laser at the MEC end-station. Laser pulse shapes demonstrated a great level of reproducibility during the experiment.

tivity of 1.99016 and 4.527138 µm/(ns × fringe shift). The velocity at the sample/pressure window interface was corrected to account for the refractive index of the used pressure windows. Fourier analysis of the VISAR interferograms resulted in a resolution of the phase shifts to within 5% of a fringe producing a sample/pressure window particle velocity precision of 50-70 m/s, with a temporal resolution of 0.05 ns. Furthermore, the VISAR images along the target plane were a useful indicator of the planarity of the compression wave. The sweep time of the VISAR windows was set accordingly to the time of the shock breakout and was typically 20 ns or 50 ns.

For the experiments at LCLS we used quasi-monochromatic ($\Delta E/E$ = 0.2-0.5 %) coherent 11.2 keV X-ray pulses with 50 fs pulse duration, containing $\sim 10^{12}$ photons. The FEL beam was furthermore focused to 50 × 50 µm^2 onto the target and centered to the focal spot of the drive laser. X-rays diffraction of the entire shocked sample volume was collected by four Cornell-SLAC Pixel Array Detectors (CSPAD's) [112], which were positioned downstream (Fig. 2.7). 2θ coverage of the scattered X-rays for the chosen X-ray energy and detector-sample distance, ensured an angular coverage of ∼20-75°.

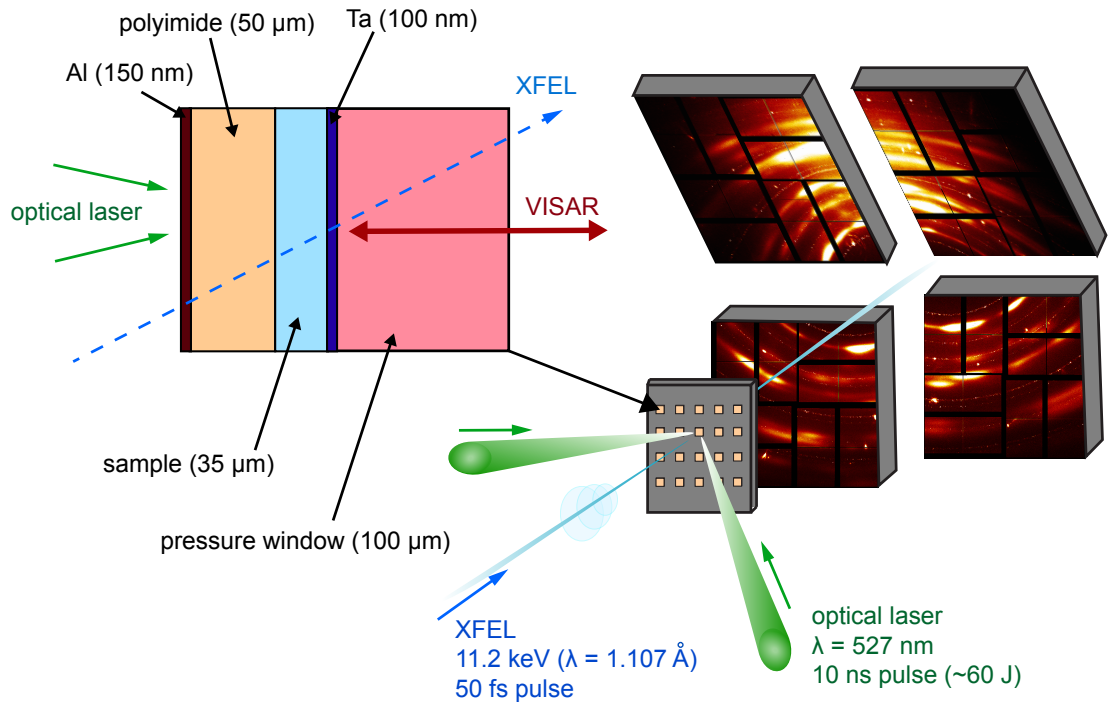

Figure 2.7: Experimental setup arranged in transmission Debye-Scherrer geometry at the MEC end-station of LCLS. On the left is indicated an insight into the sample geometry and on the right the detector arrangement. Dual drive laser beams were incident on samples at 15° and the XFEL beam at 30° from the target normal. Modified after [113].

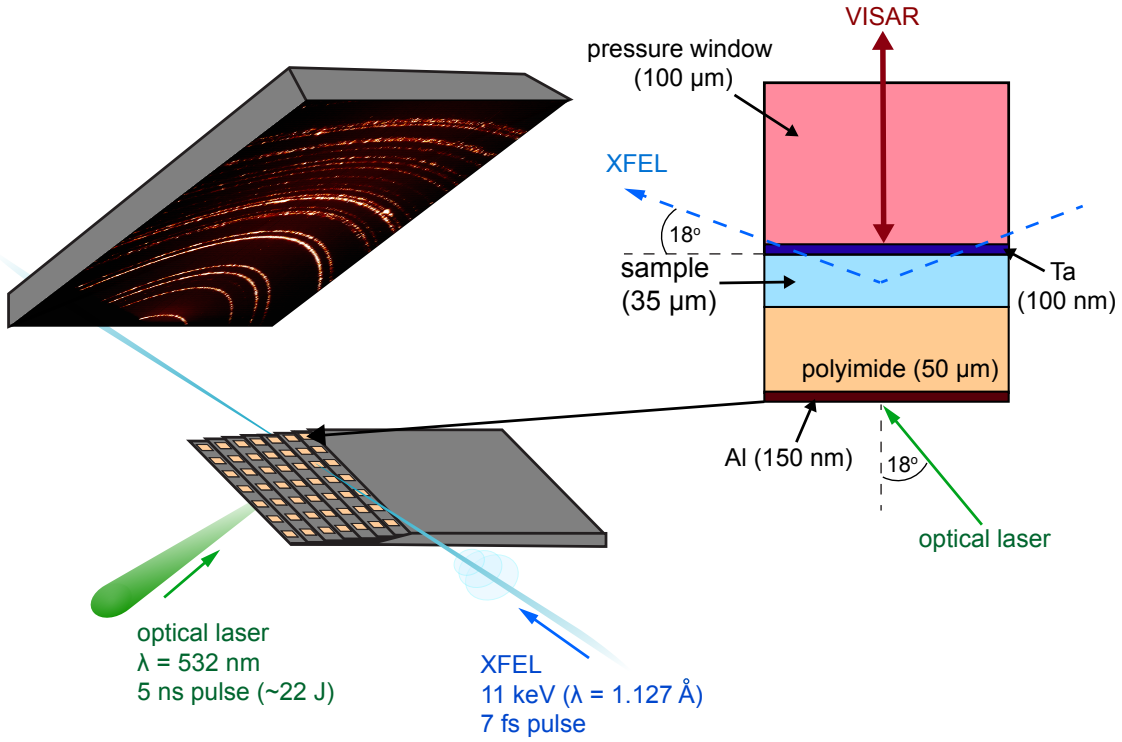

Figure 2.8: Experimental setup in grazing incidence geometry at the BL3:EH5 end-station of SACLA. Grazing-incidence angle of the XFEL towards the target was 18° and drive laser beam was incident on samples at 18° from the target normal. Modified after [113].

The BL3:EH5 end-station at SACLA

Experiments at the Spring-8 Angstrom Compact free electron Laser, Japan, were performed at the BL3:EH5 end-station. The setup for laser induced dynamic shock compression experiments at BL3:EH5 was similar to MEC, however at SACLA, experiments were conducted in grazing incidence geometry with an angle of the XFEL towards sample normal of 18° (Fig. 2.8). A ceramic YAG optical laser operated with one 532 nm beam in combination with 300 µm diameter phase plates. Laser energy was deposited onto the target as a 5-10 ns top hat pulse, at maximum drive energies of 22 J resulting in laser intensities of up to ∼1.5 TW/cm^2. For probing the sample, 11 keV X-ray pulses of ∼7 fs duration were used, focused to a 10 × 30 µm^2 spot onto the targets. A large flat panel detector (CMOS camera coupled with an X-ray scintillator) recorded X-ray scattering from the target during XFEL probing of the assembly. 2θ angular coverage of the scattered X-rays was between ∼20-80°. Similar to MEC, two VISAR legs were employed to resolve fringe-jump ambiguity from the compressed sample velocity traces. Etalon thicknesses of 5.025 mm and 8.037 mm were used, resulting in a VPF sensitivity of 8.91908 and 5.576508 µm/(ns × fringe shift). The sweep time of the VISAR windows was set to 20 ns.

2.2 Dynamic diamond anvil cell (dDAC) experiments

The high temperature SiO_2 polymorph α-cristobalite is found in meteorites in close spatial occurrence to the SiO_2 high-pressure polymorph seifertite. The abundance of low- and high pressure cristobalite phases indicate a complex compression history during impact. Therefore, to investigate the dynamic lattice response of cristobalite to high-pressures at various compression rates, we used an enhancement of a DAC, the dynamic DAC (dDAC). This section describes the sample preparation and DAC setup at the P02.2 end-station at PETRAIII as well as the final adjustment to the dynamic DAC. Further the setup of two experimental runs with the resistive heated dDAC will be shown.

2.2.1 Sample preparation and sample synthesis

α-Cristobalite was synthesized in a high temperature furnace at the Goethe University Frankfurt (GUF), Germany. For the synthesis, fused silica rods (Goodfellow GmbH) were cut to 500 µm thick and 2 cm long discs with the use of a diamond blade saw. The fused silica discs were put on a Pt-mesh and inserted into a high temperature furnace (Carbolite Gero) at ambient pressure and maximum temperatures of 1550 °C for 24 hours. Subsequently, samples were rapidly quenched by dropping the Pt-gasket into water at the cold end of the furnace's Al_2O_3 pipe. The annealing procedure allowed the growth of α-cristobalite crystals of up to $\sim$215 µm in linear dimension (Fig. 2.9a). To verify, that the quench product was cristobalite, samples were probed with a micro-Raman spectrometer (Renishaw PM-1000) housed at GUF. The measurements made use of a red (633 nm) 50 mW-HeNe laser, for which a spectrum was recorded of the initial and quenched product (Fig. 2.9b). The spectrum of the starting material displays the characteristic glass profile, whereas the quench product exhibits characteristic α-cristobalite peaks at wavenumbers of 229 cm^{-1}, 272 cm^{-1}, 285 cm^{-1}, 418 cm^{-1}, 780 cm^{-1}, 791 cm^{-1}, 1075 cm^{-1} and 1192 cm^{-1}. Prior to the dDAC experiments, α-cristobalite pieces were dissected and ground in a Zr-mortar with acetone, to obtain a fine powder. The product was mixed with $\sim$10 wt% gold powder (Sigma Aldrich), which was used as a pressure standard for the experiments. Furthermore, some single crystal α-cristobalite pieces were cut and polished to $\sim$ 15 µm thick discs along the growth direction. Single crystals and powder were both used for the experiments with the dDAC.

Preparation of the diamond anvil cells

The DACs were prepared at the P02.2 end-station of PETRAIII at DESY. The DAC is equipped with two diamond anvils (type Ia standard design from Almax easyLab) glued to a tungsten carbide seat on the upstream side and a cubic boron nitride (c-BN) seat on the downstream side (Fig. 2.10). The diamond tips are truncated to a flat surface, that

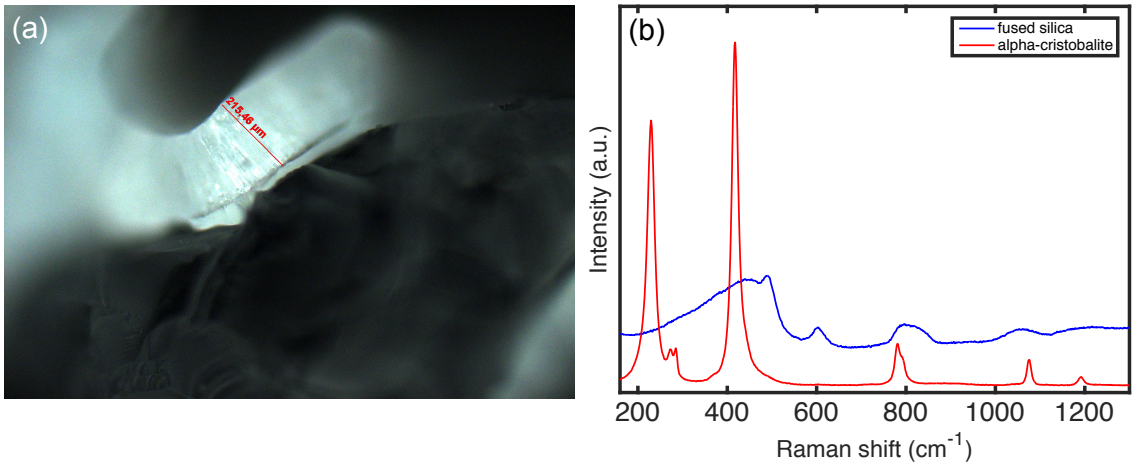

Figure 2.9: (a) Photograph of crisotbalite crystals, which show linear growth of up to ∼215 µm. (b) Characteristic Raman spectra of the starting material shown as fused silica (blue) and the product of the high temperature synthesis displays as α-cristobalite (red).

maintain sub-micron alignment of the anvils as the diamonds are driven together. Pressure between the two diamond anvils is created by mechanically tightening screws between the metal holders. When force is applied to the diamonds the sample gets pressurized. In order to separate the diamonds from each other, a rhenium gasket with a truncation in the center was placed between the diamonds. The truncation was drilled with the laser drilling system at P02.2 and resulted in a centered hole of 200 µm in diameter. It served as a sample chamber in which the sample, a pressure marker and pressure transmitting medium was hosted. The culet size was 200 µm which allowed to reach pressures within the sample of up to ∼100 GPa. The cells were loaded either with single crystal α-cristobalite or α-cristobalite powder (Fig. 2.11). The single crystal experiments were furthermore conducted using Neon as a pressure transmitting medium, to ensure hydrostatic conditions during pressurization. Neon was loaded into the cell with a gas loading system installed at P02.2.

2.2.2 Experimental dDAC setup at P02.2

To investigate the lattice response of α-cristobalite at various compression rates, we made use of the dynamic DAC. The dynamic DAC enhances the DAC by incorporating piezoelectric actuators, that substitute the mechanical tightening of the screws [71]. The DAC is enclosed by a cylinder of hardened steal with a piezoactuator (PA) being placed at the upstream of the cylinder [72]. Here, the PA pushes directly onto the DAC (Fig. 2.12). Because the upstream end of the cylinder is closed with a cap of fine threading, a small pressure is applied to the PA, which pre-compresses the sample. The PA is 90 mm in length (type 64-107 from PI Ceramic GmbH) and is equipped with a through-hole of 9 mm in diameter. This allowed the sample to rotate ±1° on the sample stack in the X-ray

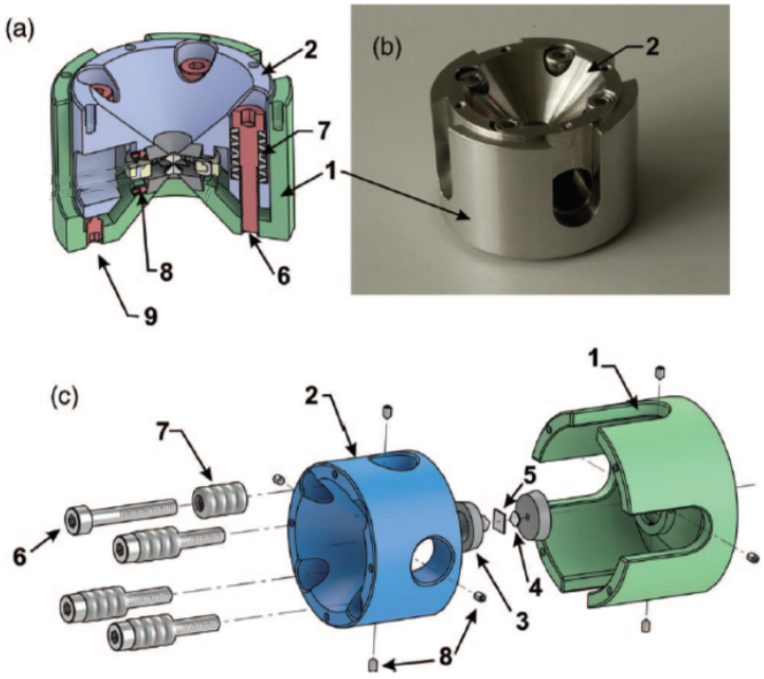

Figure 2.10: BX90 diamond anvil cell design, modified after [114]. (a) section view, (b) photograph and (c) exploded view with (1) outer cylinder part, (2) inner piston part, (3) diamond supporting plates, (4) diamond anvils, (5) metallic gasket, (6) M4 (#8-32 screws for generating loading force, (7) pack of conical spring washers (Belleville springs), (8) setscrews for diamond anvils alignment and (9) safety setscrews.

beam. The large PA provides more force than the usually smaller (60 mm) versions. However, this resulted in the force to the DAC being critically dependent on the parallelism at the interfaces between the dDAC housing and the DAC [72]. The dDAC at P02.2 is driven by a waveform generator (Agilent 33522B), a delay generator (SRS, DG645/5 with Rb clock) and a piezoamplifier (Piezosystem Jena GmbH). The waveform generator allowed to apply trapezoidal waveforms, with different rise, hold and fall times (Fig. 2.13). Three different trapezoidal waveforms were applied, to investigate the effect of slow, intermediate and fast compression, as well as decompression on the lattice response of the sample. Rise times for the waveforms were 980 s, 330 s and 160 s, holding time was 0 s, 330 s and 320 s, and fall times were 19.6 s, 330 s, and 520 s, respectively. Here, a maximum voltage of 6 V was used. The delay generator is controlled by the beamline control computer and the signal, which is triggered by an I/O signal, starts recording of the drive signals on a digital oscilloscope. The delay generator generates a time delay between the I/O signal and the triggering of the two GaAs LAMBDA detectors as well as the waveform generator. For the maximum time resolution, both GaAs LAMBDA detectors were operated the same acquisition frequency (2 kHz), but with an offset by 0.25 ms (half of the exposure time of a single LAMBDA detector), resulting in an effective frequency of 4 kHz at 12 bit data collection mode [72]. The LAMBDA detector is composed of 3 modules, tiled together resulting in a image resolution of 2.3 megapixels with a pixel size of 55 µm and

a sensitive area of 8.5 cm × 8.5 cm.

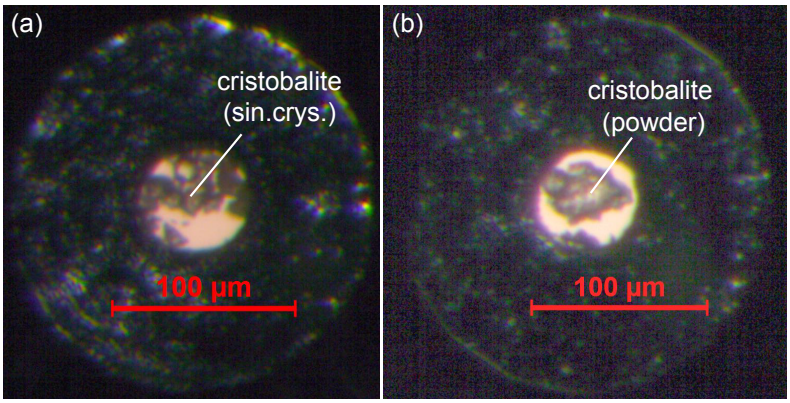

Figure 2.11: DAC culets with (a) cristobalite single crystals embedded into Ne pressure transmitting medium and (b) cristobalite powder.

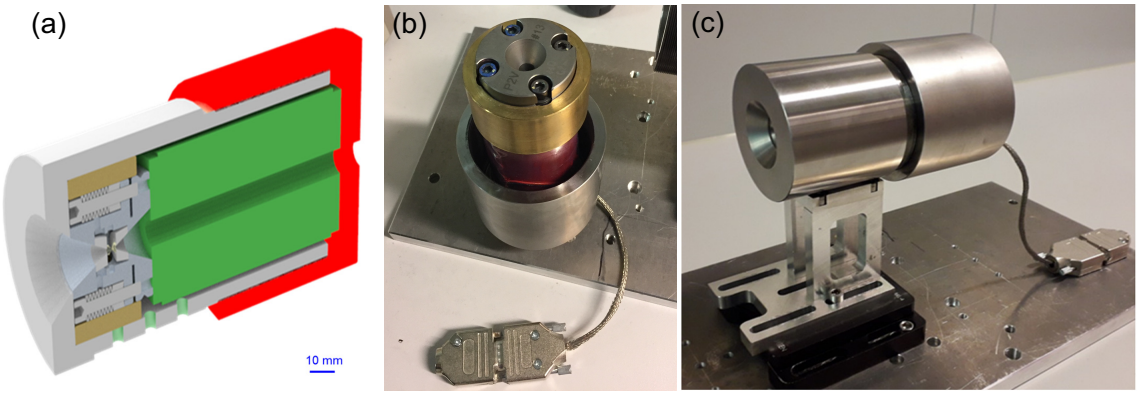

Figure 2.12: (a) 3D model of the dDAC developed at P02.2 at DESY [72]. In green is indicated the piezo-motor on top of the diamond anvil cell (gray). (b) Photograph of the opened dDAC with the diamond anvil cell on top, enclosed in the dDAC. (c) Photograph of the 90 mm dDAC equipped with the large piezoactuator [72].

The two LAMBDA detectors can be operated simultaneously and positioned independently. The detectors are offset in the horizontal direction from the X-ray beam, which passes in between the two detectors (Fig. 2.14). Because of the fast recording of the LAMBDA detectors, it was possible, to achieve a time resolved X-ray study during slow, intermediate and fast ramp compression of α-cristobalite.

For the experiments with the dDAC, a photon energy of 25.6 keV was used. Sample to detector distance (SSD), detector tilt and rotation was calibrated using a Cr_2O_3 (NIST 647b) standard and the DIOPTAS software [115]. The SSD was set to 425.7 mm with the X-ray beam being focused through a Compound Refractive Lens (CRL) system to 8(h) × 2(v) µm^2 FWHM.

Diffraction peaks on both detectors covered a 2θ range of 10° to 22°, which was sufficient to record the (111) and (200) reflection of the pressure calibrant Au to the maximum pressure of 114 GPa. Data was subsequently processed using the customized beamline

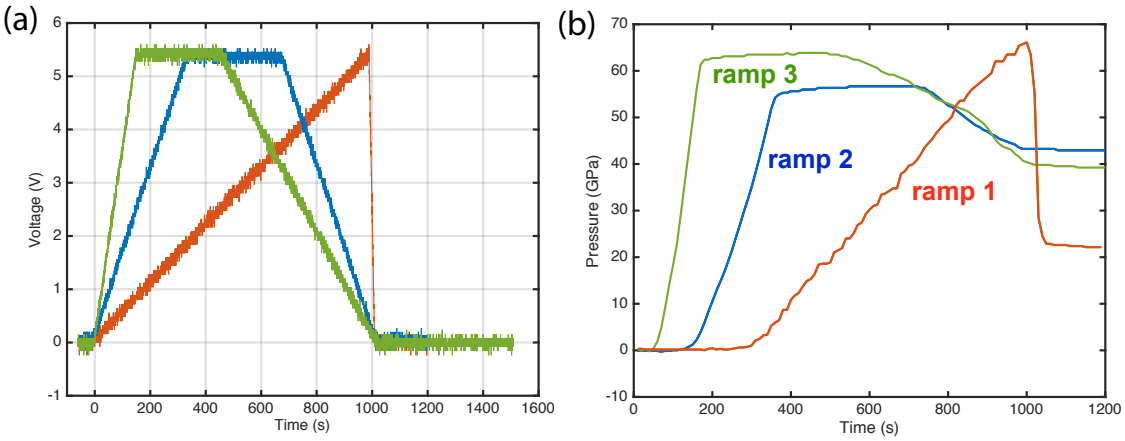

Figure 2.13: (a) Three different waveform voltage profiles as a function of time (s). (b) From the waveform profiles resulting pressures (GPa) within the dDAC as a function of time (s).

software "P02 Processing Tool" which quickly transformed the diffraction images to one-dimensional diffraction patterns as a function of frame number/time. The resulting 1D diffraction patterns were read into a Matlab script and automatically fitted by using the Savitzky-Golay function. From the fitted pattern, Au as well as cristobalite peaks were indexed, from which unit cell parameters were calculated.

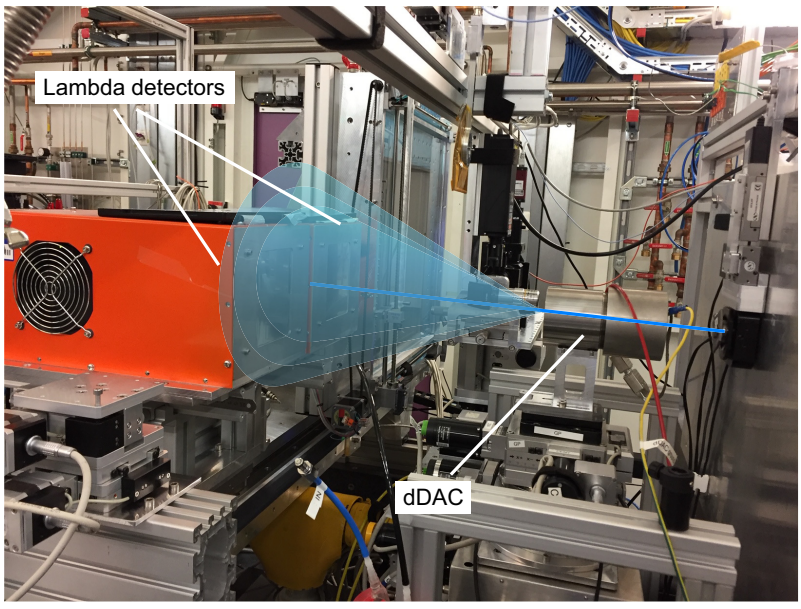

Figure 2.14: Photograph of the experimental setup at P02.2 at PETRA III of DESY. In blue are indicated the X-rays scattered from the dDAC with Debye-Scherrer rings incident on the two LAMBDA detectors.

2.2.3 Resistive heated dDAC experiments

Next to the conventional dDAC experiments, two additional experimental runs were conducted using a resistive heated dynamic DAC (RHdDAC). A detailed desciption of the setup can be found in Ref. [116]. For the heating of the samples, two rigid graphite heater discs (11 mm in diameter, 1.2 mm thick) were put around the diamond anvils with a conical aperture of 104° in the center (Fig. 2.15). Ceramic rings (12 mm in diameter, 0.5 mm thick) were glued to the seats with air-set cement (OMEGABOND 400) to prevent a heat transport towards the cell. To measure the temperature during the experiments, type-R thermocouples were put on the anvil pavilion close to the tip of the diamonds (Fig. 2.15, T1, T2). The wires of the thermocouples were laid into two grooves engraved in the

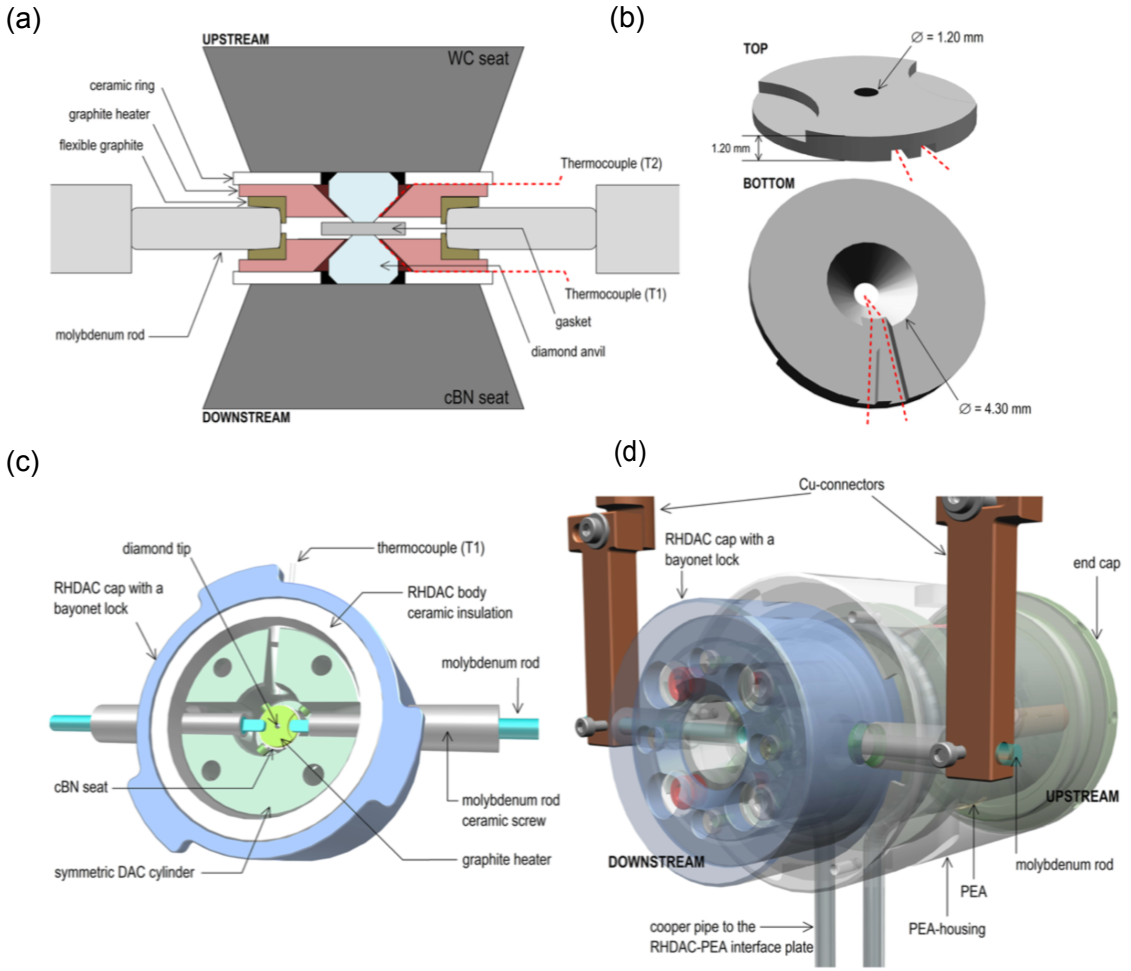

Figure 2.15: (a) Cross section of the inside of the symmetric DAC with seated diamond anvil cells and heating assembly. (b) 3D illustration of the rigid graphite heater (top and bottom view). Thermocouples are placed in the location of the red lines. (c) Attachment of the symmetric DAC cylinder to the cap with a bayonet lock viewed from above. (d) Attachment of the RHdDAC into the PEA-housing viewed from the downstream end. Images are modified after Ref. [116].

bottom faces of the heaters, coated and fixed with ceramic adhesive (Cotronics Resbond

989 from Polytec PT), to electrically insulate the thermocouples. The adhesive serves as a thermal insulator as well, due to its low conductivity (2.16 W/(mK)). Two molybdenum rods (4.7 mm thick and 68 mm long) are inserted into the DAC via two electrically insulating socket head screws, with the flat tips of the rods connecting to the graphite heater. The Mo rods are connected to a DC power supply (8 V, 220 A) with the use of copper connectors. The resistive heated DAC (RHDAC) is placed into the downstream end of the hardened stainless steel case of the piezoelectric actuator with a bayonet locked cap (Fig. 2.15). A water cooled aluminum holder is attached to the exterior of the cap. A fine threaded end cap is tightened on the upstream end. The piezoelectric actuator is thermally insulated from the RHDAC by a hardened stainless steel plate (30 mm thick), filled with ceramic insulation and encircled by a copper pipe at the interface between the RHDAC and the actuator. The piezoelectric actuator expands when connected to the amplifier via a standard high voltage feedthrough, and subsequently pushes the cooling plate, resulting in a transmission of force to the piston of the RHDAC. Furthermore, the housing of the piezoelectric actuator is enclosed with water-cooled jacket, consisting of an outer aluminum case, connected to a water chiller. The water temperature is set to 5°. Temperature of the piezoelectric actuator housing is monitored by two Pt100 sensors, which are placed close to the interface with the cooling plate and the outer part of the cooling jacket. To avoid diamond graphitization, minimize the heat loss through air convection and to avoid the oxidation of the setup, a vacuum vessel is used, at which the RHdDAC assembly is attached to the top lid (Fig. 2.16 & 2.17). To let the incident beam and diffracted X-rays pass, two Kapton windows are set into the stainless steel, water-cooled vacuum vessel on the upstream and downstream sides.

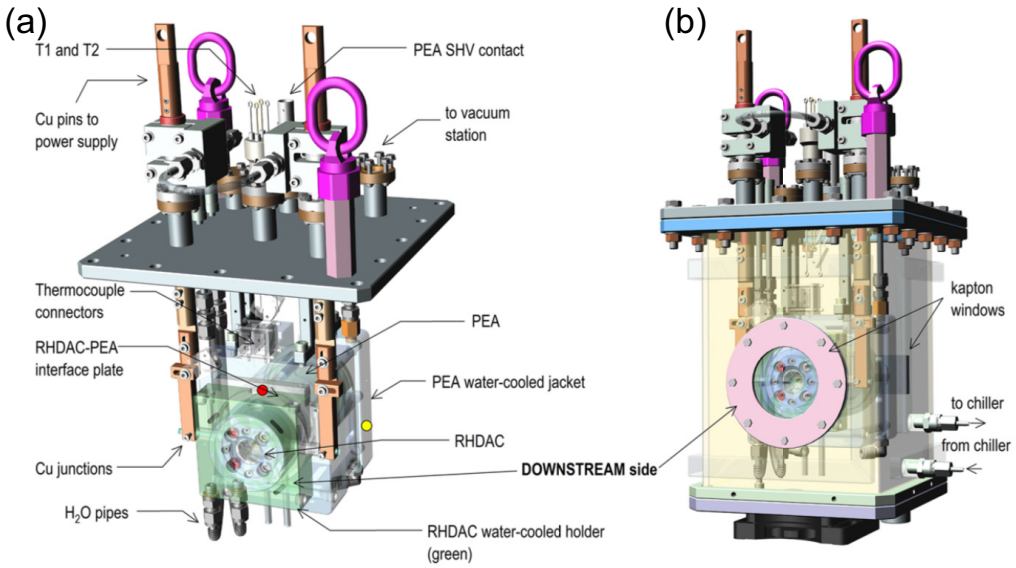

Figure 2.16: (a) Setup of the RHdDAC connected to the lid of the vacuum vessel. (b) RHdDAC inserted into the vacuum vessel. Images are modified after Ref. [116].

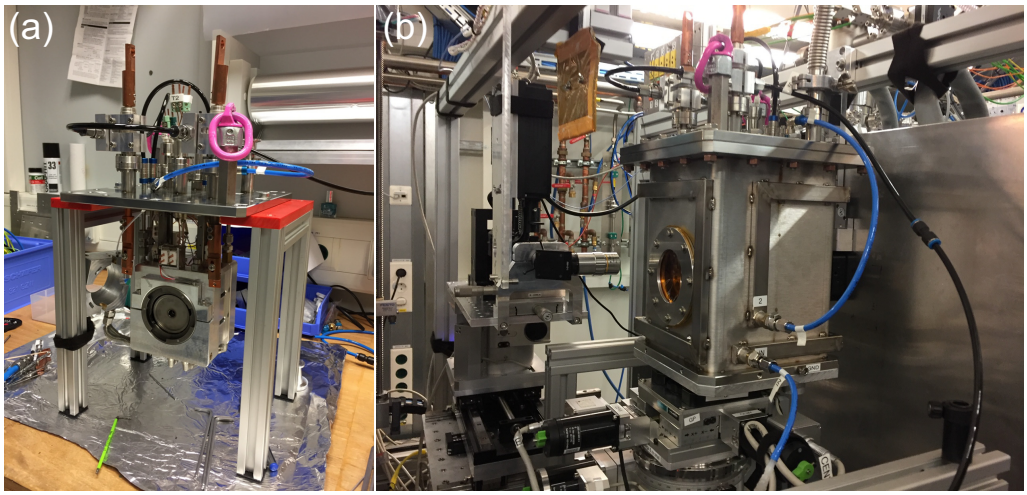

Figure 2.17: Photographs of (a) the interior of the RHdDAC, connected to the lid of the vacuum vessel and (b) the RHdDAC with surrounding vacuum vessel installed at the P02.2 end-station at PETRA III.

2.3 Computational simulations

To constrain experimental conditions and interpret obtained data, theoretical calculations of the experiments and the sample properties at high P-T conditions were conducted. Hydrodynamic simulations were performed, to define experimental parameters during shock compression. Density functional theory and molecular dynamics were used to obtain additional theoretical *ab initio* information about the sample properties on the lattice level at high pressures and to benchmark experimental results.

2.3.1 1D radiation hydrodynamics simulations

The physical processes during the interaction between an optical laser pulse and matter can be described by partial differential equations which can be solved through numerical simulations.

The laser-matter interactions, derived on the basis of experimental properties during shock compression were modeled using the plasma radiation hydrodynamic codes *Esther* [117, 118] and *Helios* [119]. The 1D software codes simulate a moving mesh within the Lagrangian-Eulerian framework, from which the density can be calculated at a fixed mass in each zone and coordinate of the mesh through energy-, mass- and momentum conservation (Fig. 2.18). For the simulations, several material parameters need to be *a priori* known, such as the equation of state, optical indices, thermal conductivities, dense plasma transport coefficients, opacities, collision and ionization frequencies and mechanical parameters. Ultimately, from the simulations the most important variables pressure, temperature and density can be calculated for each time step of the laser-matter interaction. This is vital for the accurate timing of the X-ray probe with regard to the shock wave and resulting peak pressures, temperatures and densities within the sample assembly (Fig. 2.19). The simulations make use of various equation of states of the materials, derived from e.g. the SESAME (Los Alamos

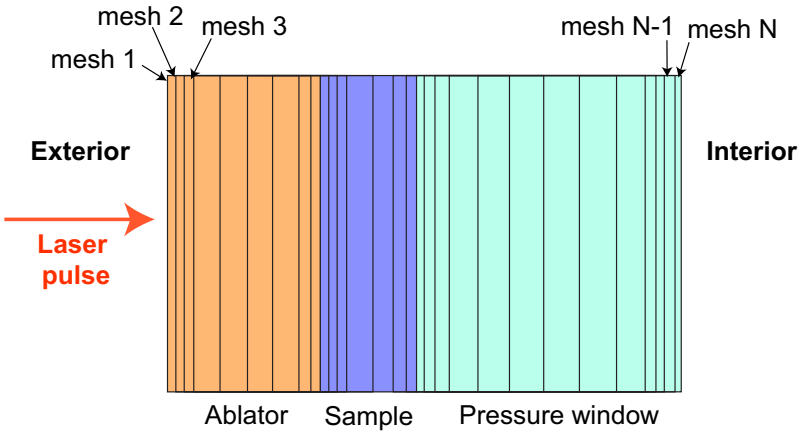

Figure 2.18: Schematic overview of the target assembly of the hydrodynamic simulations. Each part of the assembly (ablator, sample and pressure window) are segmented into smaller sections (mesh 1,2,3...N-1, N), in which the material parameters during shock compression are calculated.

National Laboratory) or the PrOpacEOS (Prism Computational Science, Inc) databases, which present good fits to Hugoniot and brightness temperature measurements in the high energy density (HED) regime. Overall for the simulations, laser pulse shapes according to the experimental measurements (Fig. 2.6) were applied. A typical output of a laser driven shock simulation on α-quartz with given peak pressure is shown in Figure 2.19 in which 3.22 TW/cm^3 top hat laser power input on a target assembly consisting of CH and α-quartz sample. Here, the pressure is plotted as a function of Lagrangian distance versus time. From the output one could obtain information about the conditions during shock transit, but also a time window for probing with the XFEL X-rays. It is important to note, that in an shock experiment, the shock front during the transition of the target assembly needs to be planar and uniform, to ensure reproducibility of measured pressures and densities for each sample. These conditions can be simulated accordingly with the use of hydrodynamic simulations. Furthermore, densities obtained from the the hydrodynamic simulations can be used to implement starting densities of structures, which are used for density functional theory molecular dynamics (DFT-MD) calculations.

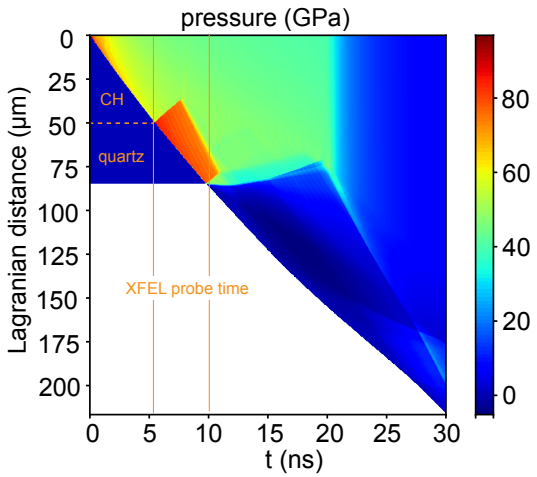

Figure 2.19: A representative result of a hydrodynamic simulation with Lagrangian distance (mm) versus time (ns) of an exemplary shock drive at the MEC end-station with regard to pressure within the α-quartz and kapton (CH) ablator. Shown is furthermore XFEL probing time, at which sample experiences peak pressures.

2.3.2 Density functional theory (DFT) - molecular dynamic (MD) simulations

Classical molecular dynamic simulations are often used to calculate matter under extreme conditions. The MD simulations numerically solve the equation of motion of a many particle system in a periodic boundary system. The integration of the motion of the particles can only be solved, if the forces which are acting on the particles are known. In many MD simulations, a model pair potential [120] is used, however the exact potential is

not known. Therefore, forces on the ions are calculated *ab initio* with density functional theory. DFT deals with the quantum mechanical description of electrons in an external potential and is based on the theorems of Hohenberg and Kohn [121] which state that (i) if two (electron) systems with an external potential v1(**r**) and v2(**r**) have the same ground-state density n(**r**), then the potentials can only differ by a constant and (ii) the density functional E[n(**r**)] has its minimum at the ground-state density. These theorems have the advantage over the use of the usual formulation of quantum mechanics, since it is not needed to solve the many particle Schrödinger equation, which requires an enormous amount of dimensions and is not feasible for more than a few electrons, but instead states, that only an electron density has to be found which yields the minimum energy [122]. From the correct energy functional E[n(**r**)], the ground state energy and density can be obtained. The energy functional can be written as

$$E[n(\mathbf{r})] = V_{ext}[n(\mathbf{r})] + U_H[n(\mathbf{r})] + T_S[n(\mathbf{r})] + E_{XC} \tag{2.2}$$

with

$$V_{ext}[n(\mathbf{r})] = \int v_{ext}(\mathbf{r}) n(\mathbf{r}) d^3r \tag{2.3}$$

being the energy due to the external potential v_{ext}(**r**), and

$$U_H[n(\mathbf{r})] = \frac{1}{2} \int \int \frac{n(\mathbf{r}) n(\mathbf{r}')}{|\mathbf{r} - \mathbf{r}'|} d^3r d^3r' \tag{2.4}$$

as the Hartree energy and ultimately,

$$T_S[n(\mathbf{r})] = \sum_i^N \int \Phi_i^*(\mathbf{r}) \left(-\frac{1}{2} \nabla^2 \right) \Phi_i(\mathbf{r}) d^3r \tag{2.5}$$

as the Kohn-Sham kinetic energy, with E_{XC} representing the Exchange-Correlation (XC) functional [123]. The XC functional consists of all unknown properties of the interacting system and plays an essential role for DFT calculations. In this study, we used the Generalized gradient approximations (GGA) which depends not only on the electron density, but also on its gradient. The GGA by Perdew, Burke, and Ernzerhof (PBE) [124] is used throughout this work which has been shown to give good results in the warm dense matter regime with reasonable computational demands. To reformulate the many-body Schrödinger equation into effective one-particle Schrödinger equations, the theorems of Hohenberg and Kohn were used by Kohn und Sham [125] to derive a set of equations:

$$\left(-\frac{1}{2} \nabla^2 + v_{eff}(\mathbf{r}) \right) \Phi_i(\mathbf{r}) = \epsilon_i \Phi_i(\mathbf{r}) \tag{2.6}$$

$$n(\mathbf{r}) = \sum_i^N |\Phi_i(\mathbf{r})|^2 \tag{2.7}$$

$$v_{eff} = v_{ext}(\mathbf{r}) + \int \frac{n(\mathbf{r}')}{|\mathbf{r} - \mathbf{r}'|} d^3r' + \frac{\delta E_{XC}}{\delta n(\mathbf{r})'} \tag{2.8}$$

The equations have to be solved self-consistently, thus an iterative approach is taken with starting from a guessed groundstate density n(**r**), constructing the effective potential v_{eff} (eq. 2.8), solving equation 2.6, and calculating the new density n(**r**) from equation 2.7. Until the energy is converged, this iteration has to be performed (Fig. 2.20). In this work, the Quantum ESPRESSO software package [126] was employed, and, in order to evaluate the Kohn-Sham equations, a plane wave expansion was used. The straightforward implementation of periodic boundary conditions is the big advantage of using plane waves for the simulations, however its representation near ions is difficult, because of the strong oscillations due to the Coulomb potential. Since many plane waves, which could represent these oscillations, come with large computational cost, so called pseudopotentials are introduced, which replace the wavefunctions with smooth functions without changing the physical outcome. In this study, the projector augmented wave (PAW) method [127, 128] was used , which represents a linear transformation between the all-electron and pseudo-wavefunctions. Furthermore, due to the periodic boundary conditions, calculations need to be done in reciprocal space by integrating over the Brillouin zone. With DFT-MD it is not possible to integrate the Brillouin zone and, instead, a summation over some special **k**-points is favored. Very common, and also applied in this study, is the use of only one Γ point, which has the advantage that the wavefunctions have real values and no complex numbers are needed. This reduced computational costs but convergence of the results needed to be carefully checked.

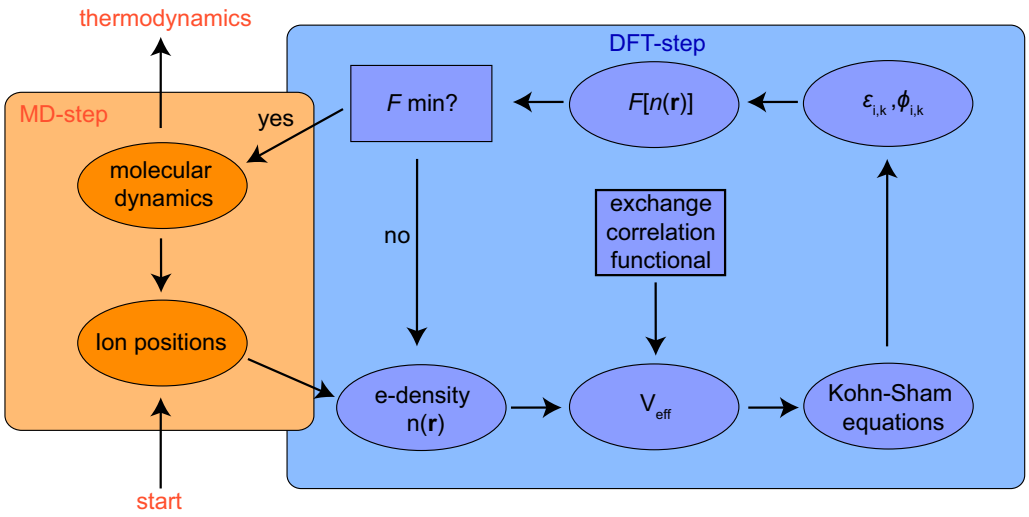

Figure 2.20: DFT-MD workflow as implemented in Quantum Espresso. Here, the DFT calculations (orange) is performed for each MD step (blue). The central input for the DFT calculation is the chosen XC functional (modified after Ref. [123]).

In this work, the Born-Oppenheimer approximation was used, which performs classical MD simulations for the ions and DFT for the electrons. Here, the calculations start with a given ion configuration within a simulation cell, which present the external potential for the DFT calculations in the electron system. The Kohn-Sham equations are solved by guessing an initial electron density n(r), and, together with the Kohn-Sham eigenvalues and wavefunctions result in the energy functional. The iteration is repeated with the new electron density until the energy functional reaches its minimum. Forces on the ions can then be calculated from the Hellman-Feynman theorem and ions are moved in a finite timestep. The MD simulations are in general performed in the microcanonical ensemble, i.e. density and energy are fixed, however for some of the simulations we rather fixed the density and temperature. This was done by using the Anderson thermostat [129], which basically removes heat when the temperature is too high or adds heat when the system is too cold. Alternatively a rescaling function was used, in which the temperature was adjusted externally. Further, for the MD runs, the mean square displacements of the ions were monitored (Fig. 2.21) from which the needed time steps for equilibrium of the system was estimated. The computational resources of the MAXWELL cluster were used at the German Electron Synchrotron (DESY), which included the use of various nodes and the workload manager *Slurm* for job processing.

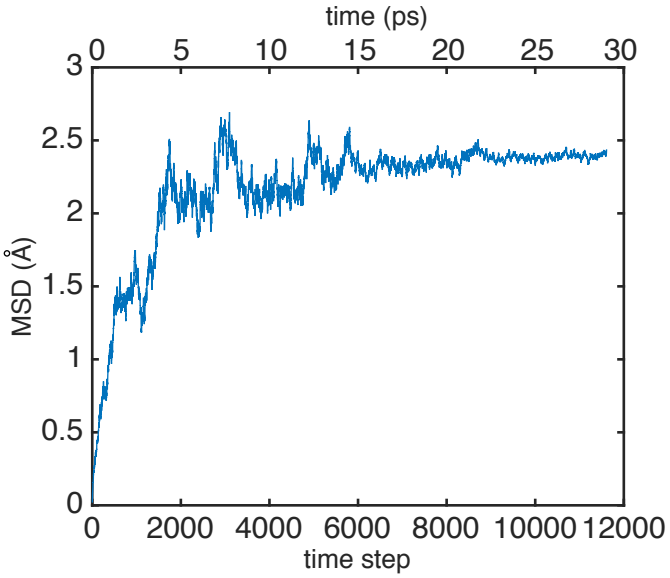

Figure 2.21: Mean square displacement (MSD) of the atoms during a typical MD simulation as a function of time step/time (ps). The MSD is equilibriated at lager time steps, at which thermodynamic parameters were extracted.

Chapter 3

Results

To elucidate the complex dynamic lattice response of silica and its structural analog GeO_2 at ultra-high pressures and to understand the effect of short compression rates and hydrostaticity on the phase transition kinetics during compression, several experiments have been performed by using dynamic compression techniques. This chapter emphasizes on the results obtained from laser induced shock compression experiments at LCLS and SACLA (chapter 3.1) as well as the dynamic diamond anvil cell (dDAC) experiments at PETRAIII (3.2). The results from the laser shock experimental campaigns treat the dynamic compression response of α-quartz (3.1.1) and stishovite (3.1.2) on the lattice level. Time-resolved X-ray diffraction and VISAR analysis are providing insights into the phase transformations and atomic structures at various high pressure states. Furthermore, X-ray diffraction was used to calculate the structure factor, corresponding radial distribution function and the coordination number of GeO_2 (3.1.3). Moreover, results from shock induced melts of α-quartz, fused silica and α-cristobalite are presented with the emphasis on nucleation and grain growth during the pressure release (3.1.4).
The results of the experimental campaign at PETRAIII with the use of the (resistive heated) dDAC demonstrates the unit cell volume dependency of the high pressure polymorphs of α-cristobalite at different compression rates. Ultimately, computational results within the DFT-MD framework and hydrodynamic simulations benchmark the experimental results on the high pressure behavior of α-quartz, stishovite and α-cristobalite during shock- and dynamic compression.

3.1 Laser induced shock compression experiments

3.1.1 α-Quartz

Experimental conditions

Laser induced shock compression experiments on α-quartz were performed at the MEC end-station of LCLS. For the experimental runs, a 10-20 ns, top hat laser pulse shape was used in combination with a 250 µm diameter phase plate to ensure high pressures and controlled stress within the sample. In order to reach a wide range of pressure states, the intensity of the laser pulse was varied between $\sim$2.05 TW/cm^2 and 3.66 TW/cm^2.

VISAR analysis

The particle velocities U_p for each shock drive were derived from the VISAR. For the experimental runs with the VISAR, LiF pressure windows were used as a reference standard. VISAR analysis was conducted with the software *Neutrino* (Copyright 2013; Alessandro Flacco, Tommaso Vinci). Particle velocities, deduced from the VISAR analysis, were used to obtain peak pressures within the sample from impedance matching calculations [130]. The α-quartz sample itself was furthermore used as a pressure standard, next to the LiF standard. Because quartz is transparent, the VISAR could be reflected at the ablator-sample interface and was used up to the maximum pressure of 94 GPa. At the ablator-sample interface, a tantalum layer served as the reflection surface, which was usually located between the sample and the LiF window. Thereby not only the particle velocity but also the shock velocity U_s of α-quartz could be determined. This was done by i) measuring the transit time of the shock wave, by observing the change of reflectivity in the sample. Here, by dividing the well known thickness of α-quartz with the shock wave transit time ($U_s = d_{sample}/t_{transit}$) one can obtain the shock velocity. Moreover, ii) with the use of the subsequent X-ray diffraction measurements, one could determine the shock velocity through the Rankine-Hugoniot relationship

$$U_s = \frac{U_p}{1 - \rho_0/\rho} \tag{3.1}$$

Here, U_p was measured by the VISAR whereas ρ_0 (initial density) and ρ (shocked density) was determined by the refined diffraction data. Methods i) and ii) were in very good agreement and differed from each within $\sim$1 %.
With U_s, U_p and the initial density (ρ_0), one could ultimately calculate the peak pressure within the sample through the Rankine-Hugoniot equation

$$P - P_0 = \rho_0 U_s U_p \tag{3.2}$$

with P_0 as the reference value at ambient state. The uncertainties of the VISAR measurements were typically between 10-15 % and arose predominantly from the uncertainties of the free-surface velocity profile (Fig. 3.1). Moreover, the density measurements from the refinement held an uncertainty from the fitting error of the diffraction data, which was however much smaller than from VISAR measurements and typically between 2-5 %.
Table 3.1 displays results of the four high pressure drives with shock- and particle velocities as well as derived peak pressures from the impedance matching calculations and direct measurements.
From shock wave- and particle velocities we obtain a linear U_s-U_p relationship of

$$U_s = 1.494U_p + 2.478 \tag{3.3}$$

in the pressure regime between 45 GPa to 94 GPa. U_s and U_p agree well with published data as shown in Figure 3.2.

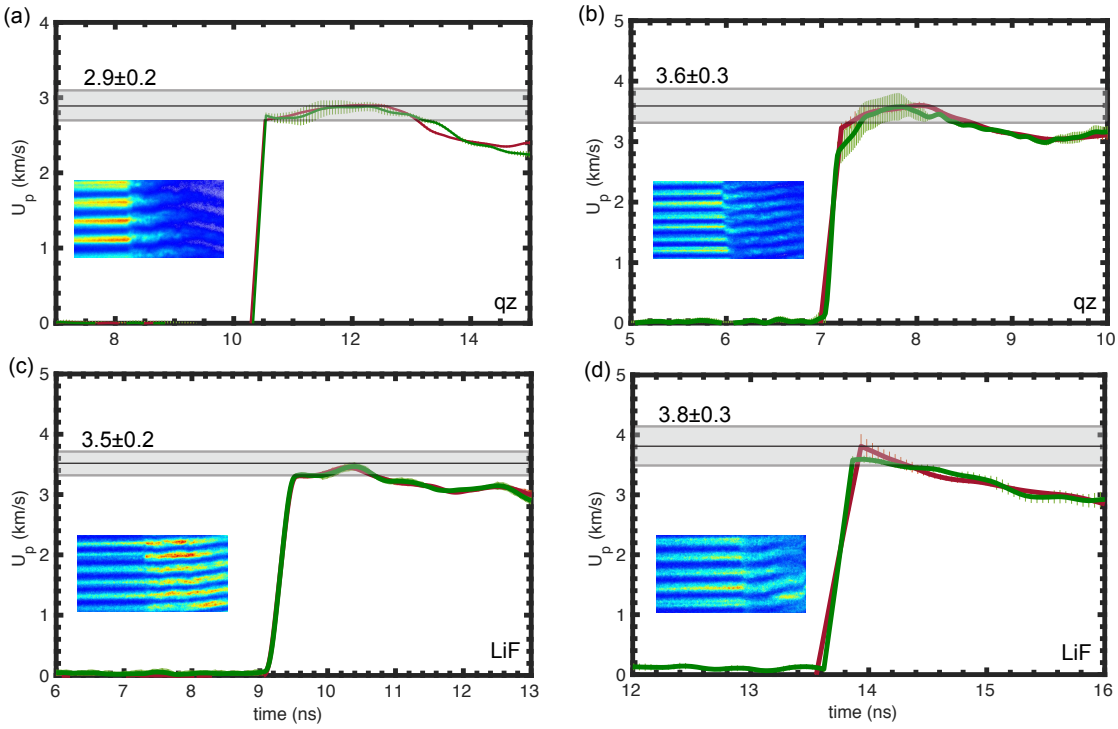

Figure 3.1: VISAR outlines for different pressure drives with particle velocities (km/s) vs time (ns). The black line is the average maximum particle velocity, the grey area indicates uncertainty. Inlets show parts of the raw VISAR images. Particle velocities and subsequently peak pressures were determined either directly from α-quartz (a,b) or indirectly through the impedance matching method with LiF (c,d) windows.

Table 3.1: Experimental results of shock compressed α-quartz from this work. Particle and shock velocities U_p and U_s and peak pressures within the α-quartz samples for different exemplary shock drives from direct and impedance matching methods are shown.

Run #	Peak pressure (GPa)	U_s(calc.) (km/s)	U_p (exp.) (km/s)	U_p (exp.)[a] (km/s)
98	45(7)	6.8(5)	2.9(2)	2.8(9)
105	73(13)	7.9(6)	3.6(3)	3.5(8)
133	79(9)	7.9(4)	3.7(2)	3.5(9)
247	94(14)	8.7(6)	4.1(3)	4.0(7)

[a] derived from impedance matching of the quartz/LiF interface

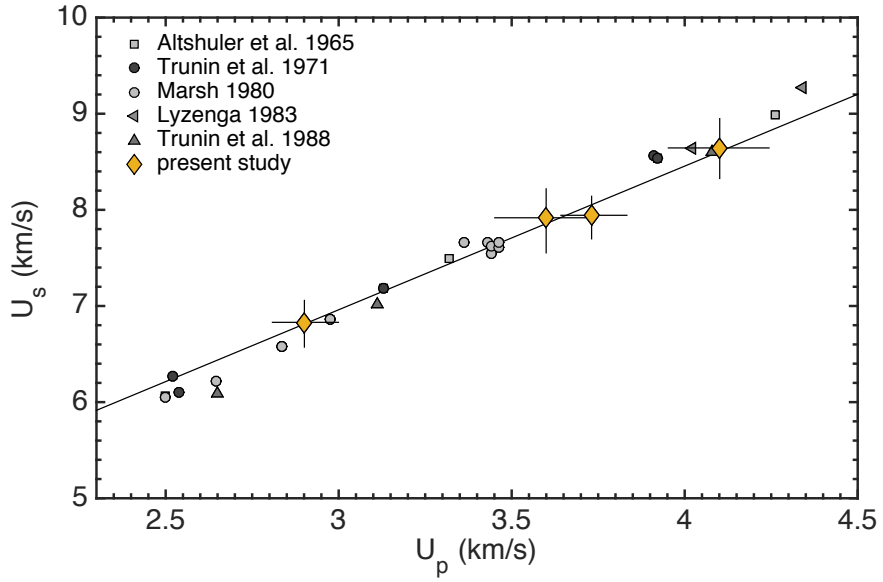

Figure 3.2: U_s - U_p relationship of shocked α-quartz from this work and literature.

X-ray diffraction

Figure 3.3 illustrates the raw X-ray diffraction (XRD) images recorded from α-quartz at ambient- and driven conditions. For the driven samples, XRD images were collected at or close the vicinity of the shock breakout, hence at peak pressure conditions. Shock breakout was recorded and confirmed by the VISAR. The diffraction image at ambient conditions displays a single crystal reflection (Fig. 3.3a) which was indexed to the (302) Bragg reflection of α-quartz. Furthermore, the aluminum coating is observed as polycrystalline Bragg reflection rings within the ambient X-ray diffraction images. These signatures are vanished in the XRD images of the high pressures drives due to the degradation of Al from the high pressure and temperature conditions. From the azimuthally integrated XRD images, several time-resolved diffraction lineouts were extracted and are shown in Figure 3.5. Here, for each peak laser intensity, successive time delays of the XFEL with regard to the optical laser were applied. These are indicated as the relative time of the shock breakout observed by the VISAR. The ambient α-quartz structure was indexed in the pre-shot (cold) pattern. One furthermore can observe a broad peak at a 2θ

angle of ∼32°, which is associated to the diamond (111) peak. This reflection derived most likely from a demixing of the partially compressed kapton (CH) ablator and subsequently highly compressed carbon at high pressures and temperatures. A signature of the demixing and can be observed in every XRD pattern of this study.

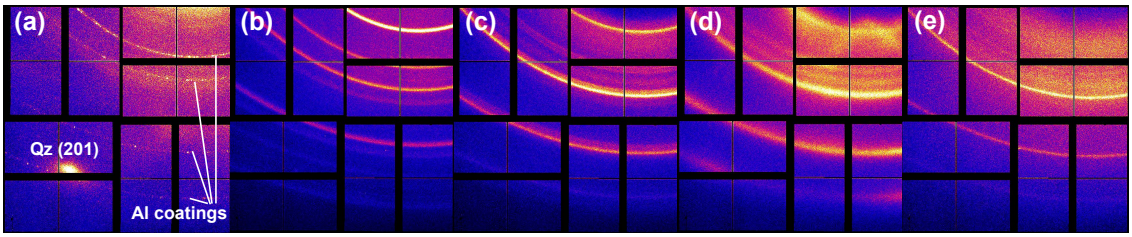

Figure 3.3: X-ray diffraction raw data images for α-quartz at (a) ambient conditions, (b) 45(7) GPa and ∼2900 K, (c) 73(13) GPa and ∼4600 K, (d) 79(9) GPa and ∼4700 K and (e) 94(14) GPa and ∼5500 K. Pressures were determined by the VISAR analysis and temperatures were estimated through hydrodynamic simulations.

Derived from the X-ray diffraction data, one observes a phase transformation from single crystal α-quartz to a crystalline structure at 44(7) GPa (Fig. 3.3b & 3.5 purple lines). Here, the high-pressure structure exhibits symmetric crystalline diffraction reflections which can be indexed to the rutile structure (tetragonal, $P4_2/mnm$), which is associated to the SiO_2 high pressure phase stishovite. Approximately 2 ns before shock breakout one can observe the emerging of several stishovite Bragg reflections. These include the (110), (101), (111), (210), (211), (220), (301) and (112) Bragg reflections of the stishovite unit cell with a maximum intensity around shock breakout (Fig. 3.4). The relative intensities of the stishovite peaks indicate no preferred orientation and are comparable to powder diffraction rings, hence stishovite is most likely polycrystalline. At peak pressures of 73(13) GPa, four dominant Bragg reflections are emerging in the XRD pattern on top of the stishovite peaks (Fig. 3.3c & 3.5 green lines). The Bragg reflections appear at 2θ-angles of ∼30.2°, ∼34.6°, ∼45.5° and ∼53.8° which can be indexed to the (100), (101), (102) and (110) Bragg reflections of the defective niccolite (*d*-NiAs) structure of SiO_2 [31]. At 79(9) GPa, the previous very pronounced (110) stishovite peak is decreasing in intensity and broadening, whereas Bragg reflections of the *d*-NiAs structure are further emerging (Fig. 3.3d & 3.5 red lines). Ultimately at the highest pressure of 94(14) GPa, one can solely observe the Bragg reflection of the *d*-NiAs structure and no other structures appear to be present (Fig. 3.5 yellow lines). The strong (110) stishovite peak has vanished completely and instead a bulk feature can be observed. A complete list of determined Bragg reflections with corresponding identified phases at each driven peak pressure is shown in Table 3.2. Also listed are theoretically Bragg reflections of the high pressure SiO_2 polymorph $CaCl_2$. This polymorph was not observed within the XRD images at pressures >60 GPa, which has been previously found in static compression experiments.

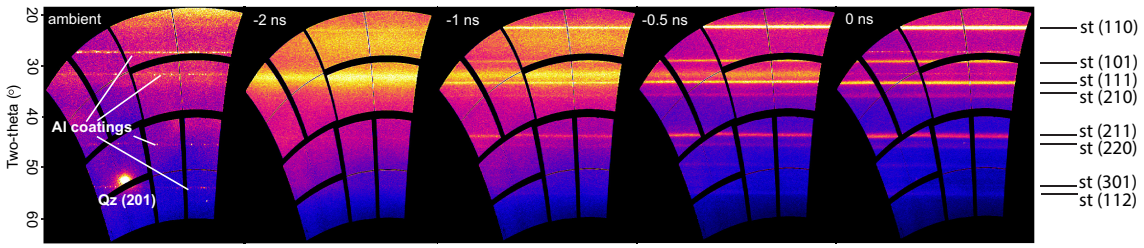

Figure 3.4: Exemplary XRD raw images of a time-series at 45(7) GPa. Time (ns) indicates the time before shock breakout. Given on the top are furthermore the positions of the stishovite Bragg reflections.

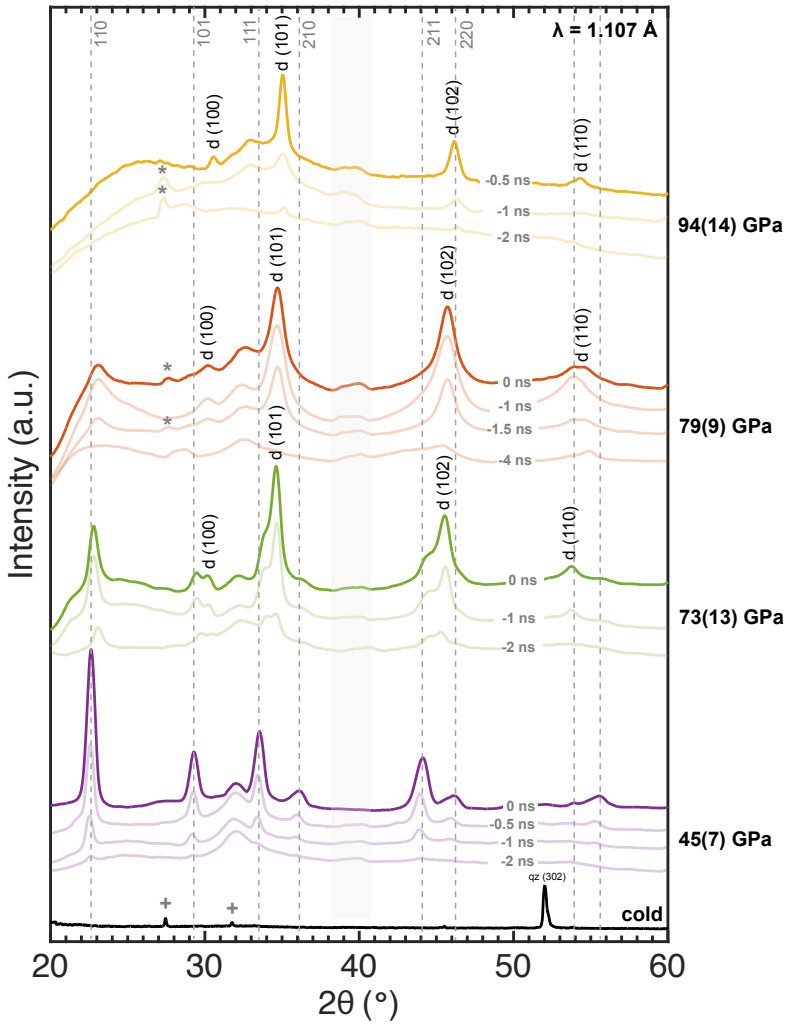

Figure 3.5: Multiplot of XRD data. Shown are the ambient data and time series (indicated as the time before shock breakout) at various peak pressures. Grey dashed lines indicate stishovite Bragg reflections at 45 GPa. d: *d*-NiAs phase; ⋆: Tantalum; +: Aluminum. Grey band indicates a detector gap of the CSPADs.

Table 3.2: Calculated vs. observed d-spacing (Å) of the stishovite and *d*-NiAs structure at different peak pressures. Given are furthermore theoretical $CaCl_2$ positions, which would be observed as a peak splitting of the stishovite (101) and (220) peaks.

phase	hkl	d (observed, Å)	d (calculated*, Å)
45 GPa			
stishovite	110	2.814	2.857
	101	2.186	2.215
	111	1.914	1.942
	210	1.781	1.807
	211	1.472	1.493
	220	1.411	1.429
	301	1.187	1.201
73 GPa			
stishovite	110	2.808	2.824
	101	2.121	2.182
	111	1.894	1.915
	210	1.780	1.786
	211	1.466	1.473
	220	1.401	1.412
	301	1.182	1.186
d-NiAs	100	2.181	2.129
	101	1.859	1.868
	102	1.428	1.436
	110	1.224	1.229
($CaCl_2$)	011	not obs.	2.101
	121	not obs.	1.422
79 GPa			
stishovite	110	2.760	2.808
	101	2.129	2.164
	111	not obs.	1.900
	210	1.764	1.776
	211	not obs.	1.463
	220	not obs.	1.404
	301	1.176	1.178
d-NiAs	100	2.123	2.110
	101	1.856	1.852
	102	1.425	1.425
	110	1.223	1.218
($CaCl_2$)	011	not obs.	2.077
	121	not obs.	1.406
94 GPa			
d-NiAs	100	2.098	2.095
	101	1.838	1.846
	102	1.411	1.429
	110	1.212	1.209

*calculated from the unit cell parameters at respective pressures

XRD refinement and densities of shock driven α-quartz

A *Le Bail* refinement on the azimuthally integrated XRD diffraction data was performed using the GSAS-2 [131] and EXPO2014 [132] software packages. Here, the known stishovite [33] and *d*-NiAs [31] phase properties served as starting structures for the refinement analysis. For the profile function, the Pearson VII peak shape was applied and the background was fitted using the Chebyshev polynomial. From the refinement calculations, lattice parameters (*a*,*c*), unit cell volume (V) and goodness of fit factor (χ^2) were obtained and are listed in Table 3.3. Calibration of the sample to detector distances and the detector tilts was performed using a CeO_2 (674b) NIST Standard Reference Material. Examples of the refined diffraction patterns are shown in Figure 3.6.

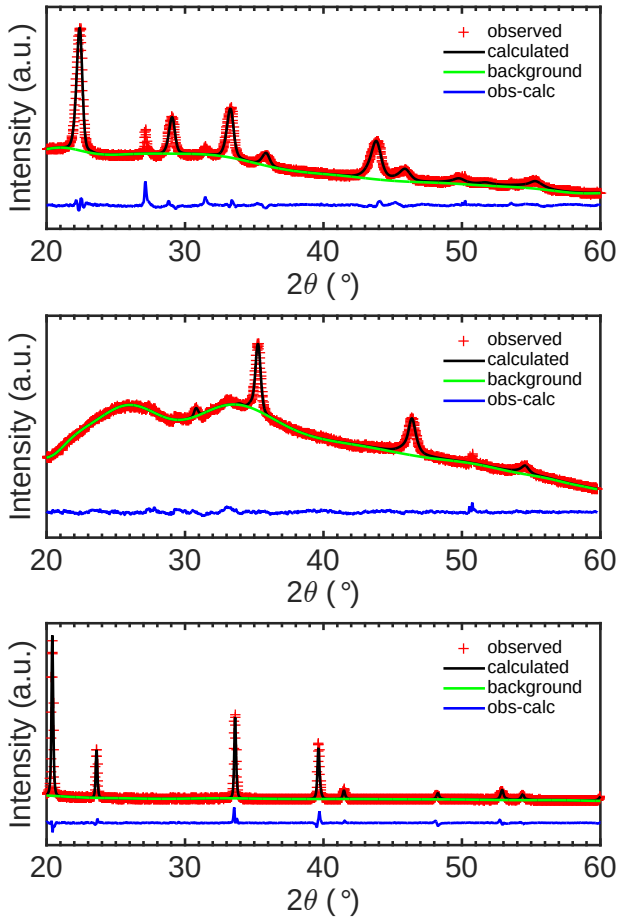

Figure 3.6: Outlines of *Le Bail* refinements on integrated diffraction data. Shown are the diffraction refinements at a peak pressure of 45(7) GPa (top panel), at a peak pressure of 94(14) GPa (middle panel) and of the CeO_2 standard (lower panel).

The density of stishovite obtained from its respective Bragg reflections of the refined diffraction pattern at 45(7) GPa is ρ = 4.61(9) g/cm^3. At 73(13) GPa a mixed stishovite/*d*-NiAs structure was observed and a phase mass fraction of $\frac{stishovite}{d-NiAs} = \frac{30.6wt.\%}{69.4wt.\%}$

Table 3.3: Unit cell parameters for the stishovite (st) and *d*-NiAs (d) structure at different experimental runs.

Run #	Peak pressure (GPa)	Identified phase	a (Å)	c (Å)	V p.f.u. (Å ^{3})	reduced χ^2
264	45(7)	st	4.041(7)	2.648(5)	21.6(1)	1.687
107	73(13)	st (30.6 wt.%)	3.99(2)	2.61(1)	20.8(2)	2.050
		d (69.4 wt.%)	2.45(1)	3.89(2)	20.3(2)	2.050
133	79(9)	st (17.3 wt.%)	3.97(1)	2.58(2)	20.5(3)	1.929
		d (82.7 wt.%)	2.44(1)	3.86(2)	19.9(1)	1.929
109	94(14)	d	2.418(6)	3.912(9)	19.85(9)	1.537

could be calculated from the refined diffraction pattern. The densities of stishovite and *d*-NiAs are $\rho_{stishovite}$ = 4.80(8) g/cm^3 and ρ_{d-NiAs} = 4.89(9) g/cm^3, respectively. The resulting density ratio was calculated to be $\frac{\rho_{stishovite}}{\rho_{d-NiAs}} = 0.98(3)$ and the total density of the mixed phase is ρ = 4.86(9) g/cm^3. At 79(9) GPa, a relative phase mass fraction of $\frac{stishovite}{d-NiAs} = \frac{17.3wt.\%}{82.7wt.\%}$ can be obtained and the calculated densities of stishovite and *d*-NiAs are $\rho_{stishovite}$ = 4.87(9) g/cm^3 and ρ_{d-NiAs} = 5.02(9) g/cm^3, respectively. Here, the density ratio of the mixed phase is $\frac{\rho_{stishovite}}{\rho_{d-NiAs}} = 0.97(3)$ with a resulting total density of ρ = 4.99(9) g/cm^3. At 94(14) GPa, refinement of the XRD pattern with *d*-NiAs as the starting structure results in a total density of 5.04(10) g/cm^3.

Hydrodynamic simulations

On the basis of the experimental laser- and target properties, hydrodynamic simulations were conducted. For the simulations of the kapton ablator and α-quartz sample, the SESAME 7770, and SESAME 7383 equation of states were employed. Both give reasonable fits to Hugoniot and brightness temperature measurements in the experimental pressure regime. The conditions of all four experimental runs were simulated at 2.05 TW/cm^2, 2.6 TW/cm^2, 2.9 TW/cm^2 and 3.66 TW/cm^2. For the experiments as well as the simulations, a 10 ns top hat pulse shape at an incident angle towards the target normal of 15° was used. Snapshots of the simulations at different times are shown in Figure 3.7. From the simulations for each laser power, one obtains maximum pressures within the α-quartz targets of $\sim$48 GPa, $\sim$76 GPa, $\sim$82 GPa and $\sim$97 GPa which are in great accordance to experimental determined pressures. Calculated densities were $\sim$4.68 g/cm^3, $\sim$4.88 g/cm^3, $\sim$4.97 g/cm^3 and $\sim$5.07g/cm^3. Ultimately, calculated temperatures of each run were $\sim$2900 K, $\sim$4600 K, $\sim$4700 K and $\sim$5000 K, respectively.

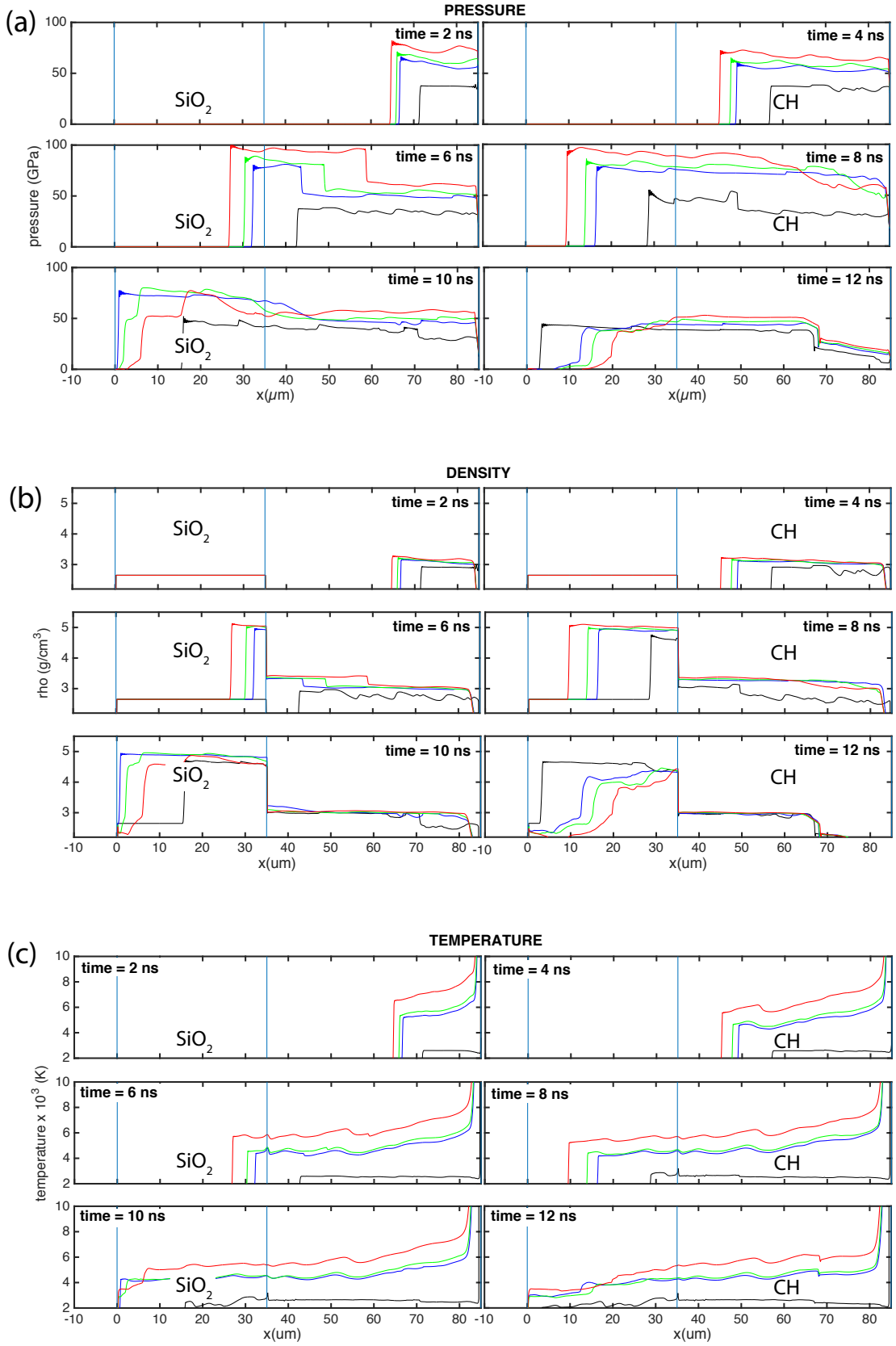

Figure 3.7: Temporal evolution of (a) pressure, (b) density and (c) temperature within the kapton and α-quartz targets derived from hydrodynamic simulations. Four different laser power inputs of 2.05 TW/cm^2 (black), 2.6 TW/cm^2 (blue), 2.9 TW/cm^2 (green) and 3.66 TW/cm^2 (red) are shown.

3.1.2 Stishovite

In this subsection, results from shock compression experiments on stishovite at the LCLS and SACLA X-ray free electron lasers are shown. The results have been published in *Scientific Reports* **10**, 10197 (2020).

Experimental conditions

The laser induced shock compression experiments on polycristalline stishovite were carried out at the MEC end-station of the LCLS- and the BL3:EH5 end-station of SACLA. For the experimental runs, synthetic polycrystalline stishovite was used with an initial density of ρ_0 = 4.30 g/cm^3 (Tab. 3.4, run795997). To compress the stishovite samples to ultra high pressures, a 10 ns flat top hat laser pulse shape in combination with 250-µm diameter phase plates at laser energies of 48.6 J, 50.6 J and 51 J was used. In order to reach very high pressures within the stishovite samples at SACLA, it was necessary to compensate the relative low optical laser energies (E_{max} = ∼22 J) of the ceramic YAG optical laser (ω=532 nm) at BL3:EH5. Hence, A shorter shock drive (5 ns) was chosen, which resulted in higher laser intensities. However, the planarity of the shock wave was decreasing and strong perturbations in the laser profile were observed.

Since only a limited number (10) of stishovite samples was available, it was not possible to obtain several diffraction patterns sufficient for a time series at each peak pressure. The samples were rather probed at- or close to vicinity of the shock breakout (±0.5 ns), hence when the sample was completely compressed. The timing of the shock breakout was *a priori* determined through hydrodynamic simulations. For the simulations of the experiment, the hydrodynamic software package *Helios* [119] was used. A representative result of the achieved pressures as a function of time and Lagrangian distance is shown in Figure 3.8. Here, the target assembly consisted of 50 µm kapton tape and 35 µm stishovite. The simulations employed the SESAME 7770 and SESAME 7360 equation of state for kapton and stishovite, respectively. The calculations show, that maximum pressures of 340(10) GPa can be achieved within ∼3 ns with the use of a 10 ns top hat laser pulse at 51 J.

VISAR analysis

From VISAR analysis, the free surface velocity U_{fs} and reflectivity of the shocked stishovite samples were obtained (Fig. 3.9). The free surface velocity can be converted to particle velocity U_p by using the acoustic approximation $U_{fs} = 2U_p$. Similar to chapter 3.1.1 (VISAR analysis), two different approaches were taken, to determine the shock velocity U_s during shock transit. The first method constituted of measuring the transit time of the shock wave in observing the change of reflectivity of the transparent stishovite.

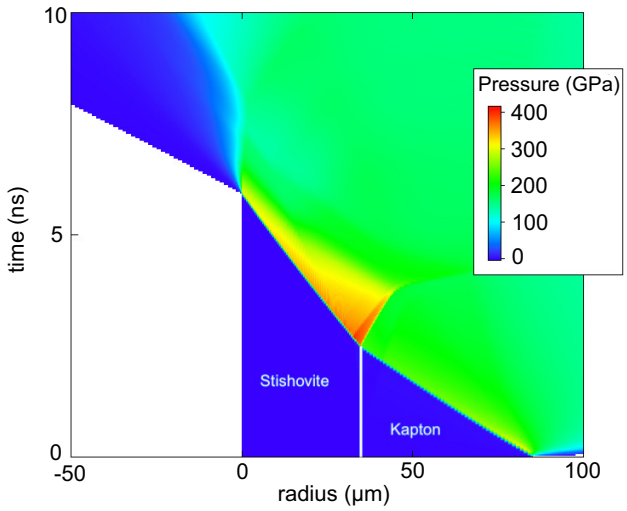

Figure 3.8: Pressure conditions derived from hydrodynamic simulations using the hydrodynamic code *Helios* [119].

With the well known sample properties, one can calculate U_s by dividing the thickness of the sample with the shock wave transit time (U_s = $d_{sample}/t_{transit}$). In the second approach, the densities of stishovite at each peak pressure, obtained through XRD refinement were used to calculate the shock velocity 3.1. In combination with equation 3.2 and the Rankine-Hugoniot relationship

$$E - E_0 = \frac{1}{2}(P + P_0)(1/\rho_0 - 1/\rho) \tag{3.4}$$

one can calculate internal pressures P (GPa) and energies E-E_0 (kJ/mol) at each experimental run. Here, E_0 and ρ_0 are reference values at ambient state. The results of the velocimetry measurements of stishovite during shock compression are listed in Table 3.4. Similar to the measurements at LCLS with α-quartz as starting material, uncertainties of

Table 3.4: Experimental results from this work on shock compressed stishovite. Particle and shock velocities U_p and U_s, as well as pressures and energies determined from VISAR are given.

Run	U_p (km/s)	U_s (km/s)	P_{VISAR} (GPa)	E-E_0 (kJ/mol)
SACLA-795997	n.a.	n.a.	ambient	n.a.
SACLA-796485	0.45(2)	9.66(53)	18(2)	0.10(1)
SACLA-796491	2.38(4)	12.10(25)	123(5)	2.82(12)
LCLS-235	4.75(8)	14.76(31)	301(12)	11.28(48)
LCLS-233*	4.90(8)	15.04(45)	317(15)	12.01(56)
LCLS-239	5.10(9)	15.35(31)	336(13)	13.01(51)

the VISAR were typically between 10-15 % and predominantly arose from the uncertainties of the free-surface velocity profile (Fig. 3.9). The quality of the VISAR at SACLA

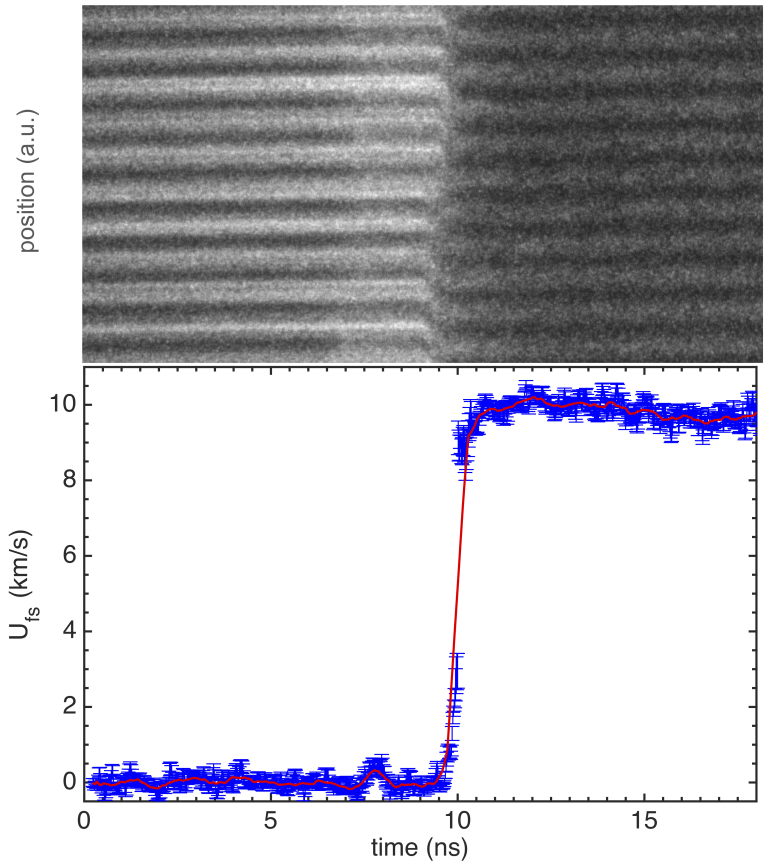

Figure 3.9: Representative VISAR image from the experiment (top image) and the corresponding free surface velocity trace (bottom image, red line). Furthermore, standard deviation of the velocity are shown (blue error bars).

was slightly inferior and the uncertainty was between 15-18 %. Moreover, the uncertainty of the density measurements of the refinement was typically between 1-2 %.

A linear fit to the U_s-U_p relationship from this study in the high pressure stishovite regime is shown in Figure 3.10. It should be noted that U_s for run233 was solely calculated by dividing the sample thickness with the shock transit time, which was determined from the reflectivity change in the VISAR image.
From the shock- and particle velocities, which were obtained in this work, one can calculated a linear fit of

$$U_s(km/s) = 1.21U_p + 9.155 \tag{3.5}$$

within the pressure regime of 0-336 GPa which is in excellent agreement to literature data [133] and indicates that the applied acoustic approximation for stishovite is valid at these pressures.

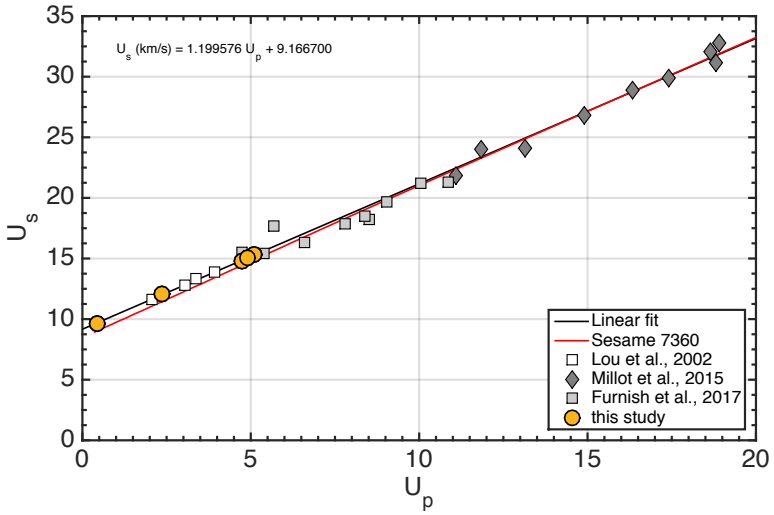

Figure 3.10: U_s - U_p relationship from this work and literature [63, 133, 134, 135]. Shown is furthermore the linear fit from this work and the SESAME7360 equation of state as a reference.

X-ray diffraction

Figure 3.11 illustrates a multiplot of 5 different XRD images and their corresponding azimuthally integrated XRD pattern at the ambient state and at peak pressures of 18(2) GPa, 123(5) GPa, 301(12) GPa and 336(13) GPa. At ambient state, one can observe the characteristic polycrystalline stishovite Bragg reflections. The most prominent reflections are (110), (101), (111), (210) (211) and (220) which are further observed upon shock loading up to 336(13) GPa. For the high pressure drives at LCLS at 301(12)GPa and 336(13) GPa, partly ambient stishovite peaks are still apparent (Fig. 3.11, indicated with an asterisk). This feature indicates that the sample was not completely compressed during XFEL probing. Furthermore intensity of the stishovite peaks from experiments of SACLA and LCLS are deviating from each other, mainly due to background corrections.
Next to the experimentally obtained X-ray diffraction pattern, the theoretical Bragg reflections of the stishovite, PbO_2 and pyrite-type silica structures at 336 GPa were calculated. The peak positions of each structure are plotted in comparison to the XRD spectra of run239 in Figure 3.12. Except of the stishovite Bragg reflections, no other high pressure SiO_2 polymorph candidate matches the present XRD pattern at the respective pressure.
Furthermore, the evolution of lattice spacing d (Å) of the primary stishovite reflections at given peak pressures are shown in Figure 3.13 and compared to other SiO_2 high pressure structures. Here, the characteristic peak splitting towards the $CaCl_2$ structure, seen in static experiments, cannot be observed. Furthermore, neither does the d-spacing of α-PbO_2 nor the pyrite-type silica fit the obtained XRD spectra from this study.

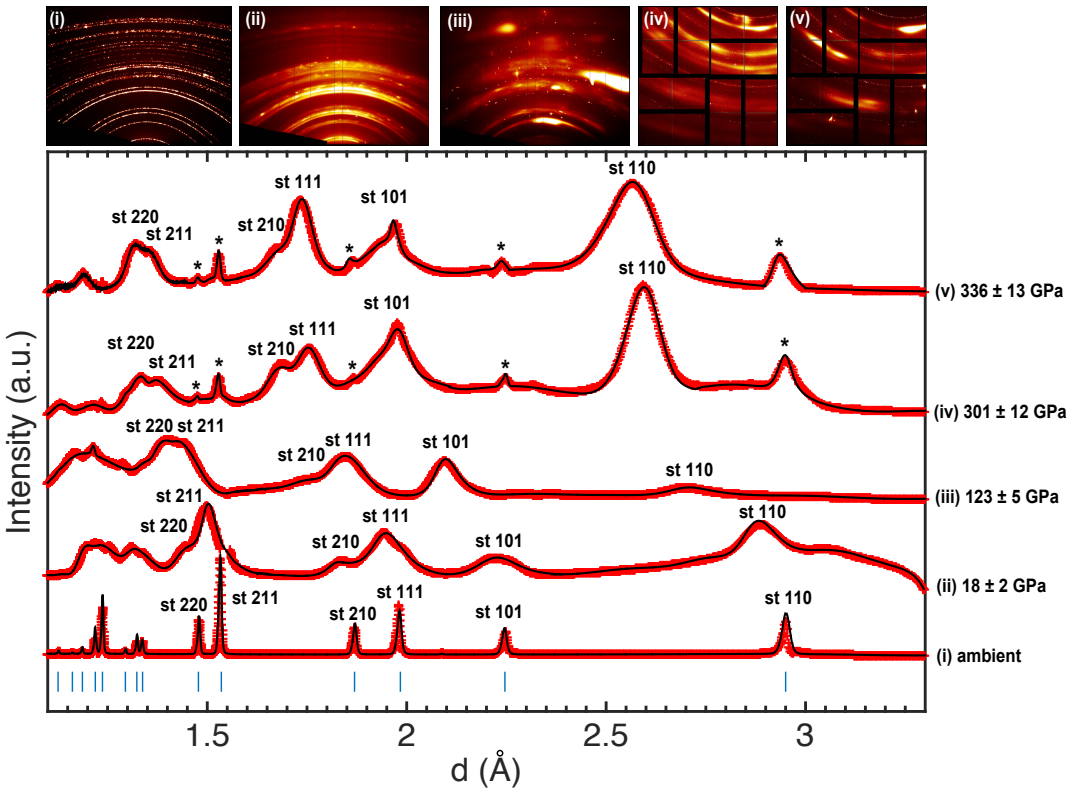

Figure 3.11: Multiplot of XRD pattern of stishovite. Observed *d*-spacing (red crosses) and Le Bail-fitted pattern (black line) of stishovite at ambient conditions, 18(2) GPa, 123(5) GPa, 301(12) GPa and 336(13) GPa. Stishovite peaks are labeled at each peak. Peaks at ambient conditions are indicated with an asterisk. Note that peaks are shifting to lower *d*-spacing values due to the change in volume of the lattice with increasing pressure.

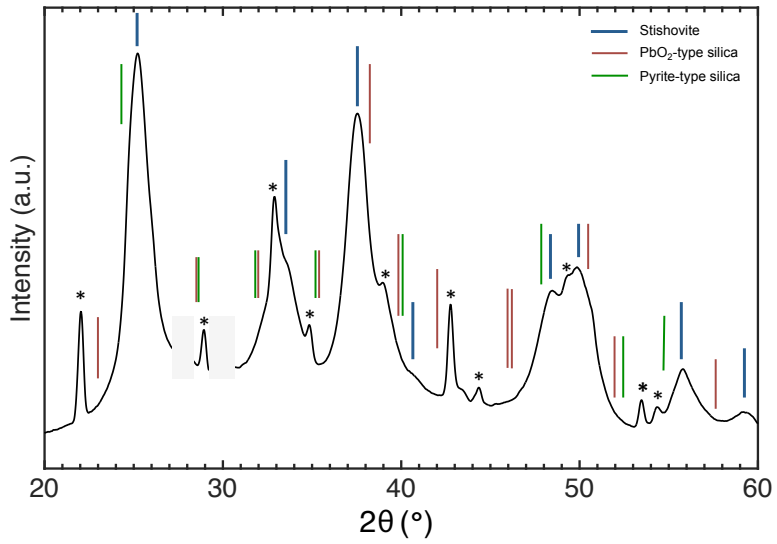

Figure 3.12: XRD outline (black line) of run235 at 301 GPa. Indicated are Bragg Peaks of stishovite (blue), of the PbO_2 type silica (red) and the pyrite-type SiO_2 (green). Peaks with an asterisk indicate still un-shocked stishovite. Gray areas indicate discontinuities in the plot from detector gaps.

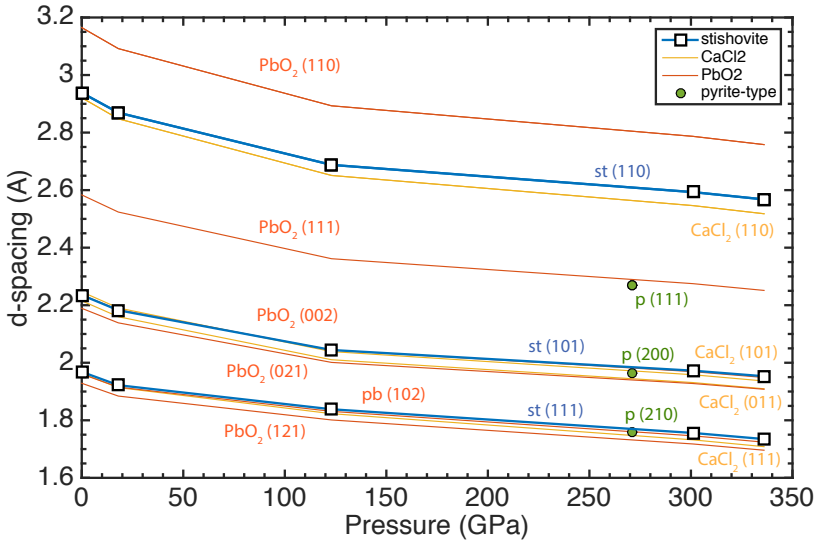

Figure 3.13: Measured *d*-spacing of primary stishovite reflections at given pressures (squares) compared to calculated *d*-spacing positions of stishovite (blue), $CaCl_2$ (yellow), α -PbO_2 (red) and pyrite-type silica (green dots).

XRD refinement, volume change and densities of stishovite

A *Le Bail* refinement on the integrated XRD diffraction data at ambient- (run795997) and shock compressed conditions were performed using the EXPO2014 software [132]. Refinement was conducted with the stishovite starting structure [33] and the Pearson VII peak shape function. Here, the the lattice parameters (*a*,*c*), unit cell volume (V) and density (ρ) were calculated and listed in Table 3.5. From the refined diffraction pattern, a relative change in volume of $V/V_0 = 0.95$ and a shock density of 4.51 g/cm^3 can be extracted at peak pressures of 18(2) GPa. At 123(5) GPa, XRD of compressed stishovite reveals a relative volume change of $V/V_0 = 0.80$ at a density of 5.35 g/cm^3 and at 301(12) GPa a volume change of $V/V_0 = 0.69$ at a density of 6.3 g/cm^3 can be determined. At 336(13) GPa, the highest achieved pressure within stishovite in this work, a relative volume change of $V/V_0 = 0.66$ at a density of 6.44 g/cm^3 was calculated. Note that for run LCLS-233 at 317(15) GPa, no X-ray diffraction data was available due to an electromagnetic pulse (EMP) and subsequent failure of the CSPADs during the optical laser shot. For this run, volume and density is solely determined from velocimetry data, described in the previous section. Here, a relative volume change of $V/V_0 = 0.67$ at a shock-density of 6.4 g/cm^3 was calculated. To evaluate the quality of the refinement, a goodness of fit factor (χ^2)

Table 3.5: Unit cell paramters of ambient and shock compressed stishovite. Shown are volume, density and lattice parameter *a* and *c*, obtained from refined XRD spectra.

Run	V (Å ^{3})	ρ (g/cm^3)	a (Å)	c (Å)
SACLA-795997	46.5(2)	4.30(2)	4.176(8)	2.664(6)
SACLA-796485	44.3(3)	4.51(5)	4.09(1)	2.65(1)
SACLA-796491	37.3(2)	5.35(4)	3.85(1)	2.513(9)
LCLS-235	31.8(4)	6.3(1)	3.69(2)	2.33(2)
LCLS-233*	31.3(9)	6.4(3)	n.a.	n.a.
LCLS-239	31.0(4)	6.44(8)	3.66(2)	2.32(1)

*no XRD information is available for run233. All results of run233 were solely determined through velocimetry data.

and the reliability factors, R_{wp} and R_p were determined and listed in Table 3.6. It must be noted that larger χ^2 factors are calculated for the shock-compressed runs at LCLS, due to the partially ambient phase and the gaps of the CSPADs. To calibrate the sample to detector distances and detector tilts, the NIST Standard Reference Materials (SRM) CeO_2 (674b, LCLS) and LaB_6 (660a, SACLA) were used.

Table 3.6: Fit parameters from refinement of shock compressed stishovite. Shown are the goodness of fit factor (reduced-χ^2) and the reliability factors, R_{wp} and R_p, derived from *Le Bail* refinements of stishovite.

Run	reduced-χ^2	R_{wp}	R_p
SACLA-795997	1.153	2.474	1.689
SACLA-796485	1.422	3.724	2.372
SACLA-796491	1.367	2.473	1.602
LCLS-235	3.590	2.615	1.917
LCLS-239	1.962	3.661	2.526

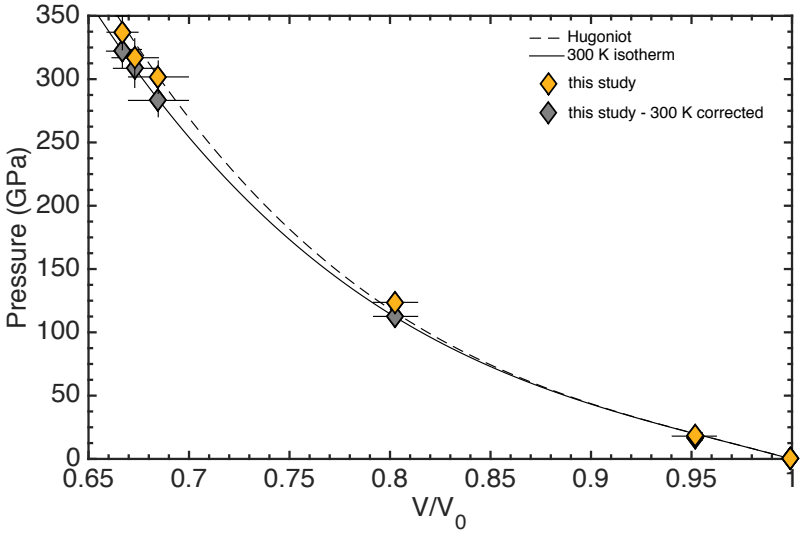

Figure 3.14: Relative volume change of shock compressed stishovite with regard to pressure from this study.

First principle calculations

In order to validate achieved pressures obtained from the experiments, results were compared to first principle simulations. Here, ground states from density functional theory were computed starting with the refined structures and densities of each experimental run. DFT was performed using 48 atoms in a 2×2×2 tetragonal supercell with Γ centered k-points to sample the entire Brillouin zone. The effect of the finite size in the simulation zone cell was investigated by using a larger cell of 384 atoms (3×3×3), however no immediate effect on the internal stress was observed. A good compromise between accuracy and computation speed was found for the plane-wave expansion of the Kohn-Sham orbitals with a cutoff of 80 Ry.

The determined pressures from DFT are in reasonable agreement to the experimental results and to literature data (Tab. 3.7). Internal stress is not computed for run233, since a refined starting structure was not available.

Table 3.7: Comparison between obtained pressures of the experimental work to literature data and density functional theory.

Run	P_{VISAR} (GPa)	P_{EOS}[133] (GPa)	P_{DFT} (GPa)
796485	18(2)	17.1	20.6
796491	123(5)	119.3	118.9
235	301(12)	313.8	305.1
233*	317(15)	329.6	n.a.
239	336(13)	359.1	335.9

Equation of state

To gain more information about the equation of state of stishovite at high pressures, P-V/V_0 (Fig. 3.14) was corrected to a 300 K isotherm and fitted with the *EosFit* software [136] to the third-order Birch-Murnaghan equation of state [137]. The 300 K isotherm was calculated by subtracting the thermal pressure from the shocked state at fixed volume [37]. To calculate the thermal pressure, one has to estimate the reached temperature conditions of the individual experimental runs, which was done according to the approach of [63], using the Mie-Grüneisen formalism [138, 139]

$$\gamma(V) = V\frac{\partial P(V,T)}{\partial E(V,T}|_V \tag{3.6}$$

The Grüneisen parameter γ(V) is assumed to be only a function of the volume

$$\gamma(V) = \gamma_0\left(\frac{V}{V_0}\right)^q; \gamma_0 = 1.35 \tag{3.7}$$

with q = 2.6 [133], V_0 as the ambient specific volume and γ_0 the ambient Grüneisen parameter [140].
The pressure on the isentrope can be derived from the Eulerian strain framework [141], using a finite strain parameter *f*

$$f = \frac{1}{2}\left[\left(\frac{V_0}{V}\right)^{\frac{2}{3}} - 1\right] \tag{3.8}$$

and the third-order Birch-Murnaghan strain-stress relation [137]

$$P_S = 3K_{0,S}f(1+2f)^{\frac{5}{2}}[1 + (3/2)(K'_{0,S} - 4)f] \tag{3.9}$$

Furthermore, the internal energy of the isentrope can be described through

$$\Delta E_S = (9/2)V_0K_{0,S}f^2[1 + (K'_{0,S} - 4)f] \tag{3.10}$$

To calculate the shock temperature, one can use the Debye model using the Debye temperature θ(V):

$$\theta(V) = \theta_0 \left(\frac{V_0}{V}\right)^{\gamma} \tag{3.11}$$

and the specific heat C_V as a function of the temperature only:

$$C_V(T) = 9nR \left(\frac{T}{\theta_0}\right)^3 \int_0^{\theta_0/T} \frac{x^4 e^x}{(e^x - 1)^2} dx \tag{3.12}$$

with n the number of atoms in a formula unit (n=3, SiO_2) and R being the perfect gas constant.
From equation 3.6 and 3.7 one can write

$$P_H - P_S = \frac{\gamma}{V}(E_H - E_S) \tag{3.13}$$

with H being the states along the Hugoniot and S for the isentrope, derived from the reference state E_0, V_0 and T_0.
The Rankine-Hugoniot relation gives:

$$E_H = E_0 + \frac{1}{2}(P_H + P_0)(V_0 - V) \tag{3.14}$$

Using equation 3.6, 3.7 and 3.14, the pressure along the Hugoniot can be obtained with:

$$P_H = \frac{P_S - \gamma(\frac{E_S}{V} - \frac{P_0}{2})(\frac{V_0}{V} - 1)}{1 - \frac{\gamma}{2}(\frac{V_0}{V} - 1)} \tag{3.15}$$

With the equations 3.6, 3.7, 3.9 and 3.14 one can write:

$$\frac{V}{\gamma}(P_H - P_S) = \int_{T_H}^{T_S} C_V dT \tag{3.16}$$

With

$$dS = \frac{\gamma C_V}{V} dV + \frac{C_V}{T} dT \tag{3.17}$$

and

$$ln\left(\frac{T_S(V)}{T_0}\right) = -\int_V^{V_0} \frac{\gamma}{V} dV \tag{3.18}$$

one can calculate the temperature along the isentrope using equation 3.7 as

$$T_S(V) = T_0 exp\left(\frac{\gamma_0)}{q}\left[1 - \left(\frac{V_0}{V}\right)^q\right]\right) \tag{3.19}$$

The temperature along the Hugoniot can then be calculated by solving equation 3.10 using a constant specific heat C_V = m(3nR) with m being a multiplier to the Duong-Petit limit value:

$$T_H = T_S + \frac{V)}{m(3nR)\gamma}(P_H - P_S) \tag{3.20}$$

Ultimately, the shock wave data fit to the third-order Birch-Murnaghan equation of state yields a bulk modulus of $\mathbf{K_0}$ **= 307** $\pm$ **4 GPa** and its first pressure derivative $\mathbf{K_0'}$ **= 4.66** $\pm$ **0.15 GPa** in the range of 0-336 GPa.

Variable cell DFT-MD simulations

Lattice parameters *a* and *c* derived from the XRD *Le Bail* refinement were plotted against run pressures (Fig. 3.15). While lattice parameter *c* exhibits an almost linear trend, lattice parameter *a* shows signs of a decreasing relative compression at pressures exceeding ∼100 GPa. These results indicate strong anisotropic compression which might contribute to the remaining stishovite structure at ultra-high pressure conditions.

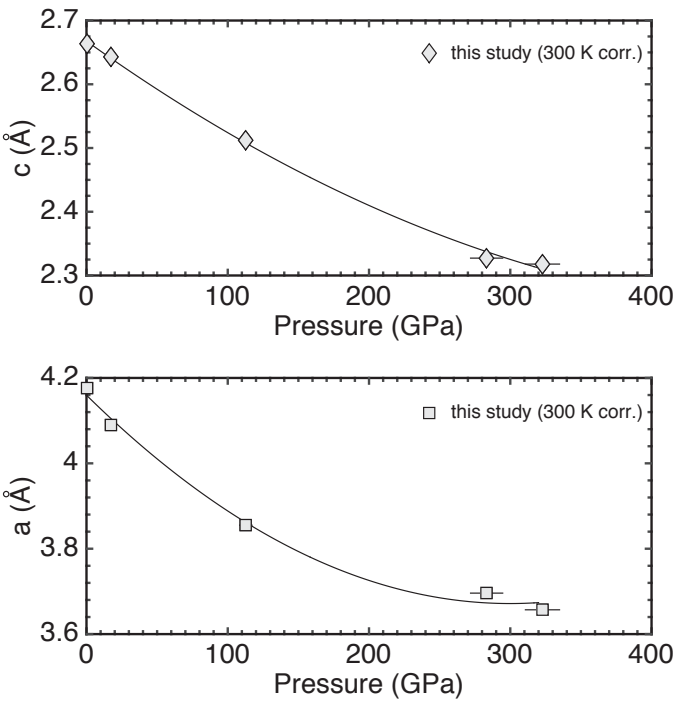

Figure 3.15: Unit-cell parameters *a* and *c* of stishovite with regard to pressure (GPa).

To elucidate the effect of anisotropy within the *c*-direction of the stishovite unit cell, a metadynamics study at given experimental pressures by means of variable cell DFT-MD (vc-md) was performed. Here, refined structures of the experimental runs were used, to generate a 2 $\times$ 2 $\times$ 2 stishovite unit cell, generated through a plane wave self consistent field (pwscf) optimization. Subsequently a variable cell DFT-MD simulation was conducted, employing a total number of 48 particles (32 O and 16 Si atoms). The ionic temperature was set to 300 K and was controlled through velocity rescaling. The interaction between electrons and ions is described by PAW pseudopotentials and the PBE approximation was chosen for the exchange correlation functional. The planewave energy cutoff was set to 80 eV and the Γ point was used for the k space. A total of 3000 time steps was applied, each 2.5 fs long, resulting in 7.2 ps total simulation time. All simula-

tion parameters have been thoroughly checked to ensure the convergence of the results. Two cases were simulated: in the first approach, all lattice vectors were allowed to move freely under hydrostatic compression and the pressure was applied within all three crystallographic directions. In the second approach, non-hydrostatic conditions were simulated, in which the compression was only applied in the *c*-direction, generating large uniaxial stress conditions within the unit-cell.

The results of the simulations show that in the case of hydrostatic compression at 300 GPa and 300 K, the expected displacive phase transition towards the high pressure polymorph $CaCl_2$ is promoted. Here, the structure differs from stishovite only by a small rotation of the octahedral chains (Fig. 3.16).

At non-hydrostatic conditions it can be demonstrated that applying uniaxial stress displaces only the oxygen atoms slightly, but the general stishovite structure is still preserved.

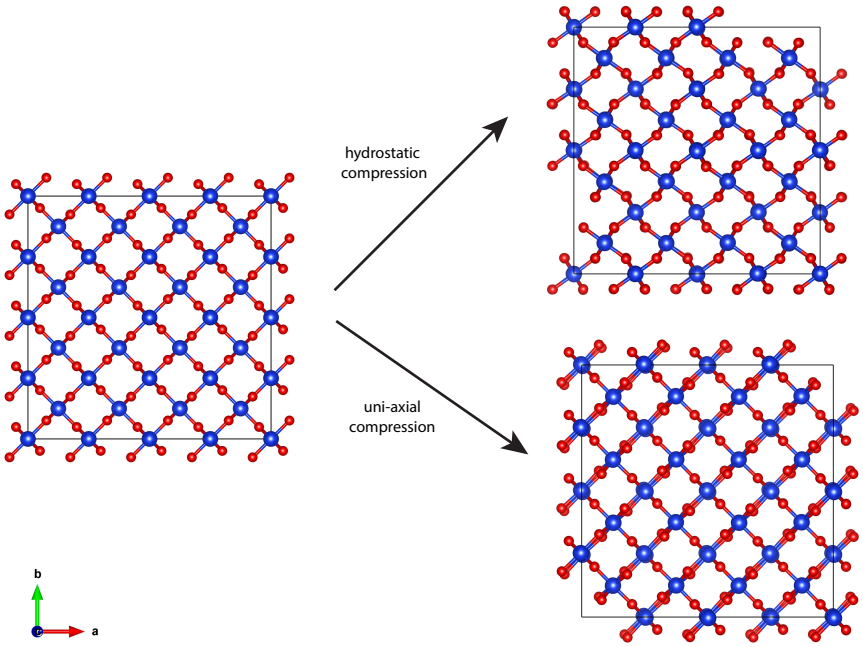

Figure 3.16: Snapshots of the DFT-MD simulation of stishovite for the hydrostatic and non-hydrostatic case at 300 GPa and 300 K. The structures are viewed along the c axis with the large spheres representing the Si atoms and the small ones the O atoms. In the hydrostatic case, the expected high-pressure $CaCl_2$ structure can be observed in contrast to the partially intact stishovite structure in the non-hydrostatic case.

3.1.3 GeO_2

Experimental conditions

Laser induced shock compression experiments on GeO_2 were carried out the MEC end-station of LCLS to elucidate the high pressure phase transformation on the respective Hugoniot and to calculate the structure factor, radial distribution function and the coordination number at high pressure conditions.
Here, a 10 ns, quasi flat top hat laser pulse shape in combination with 250-µm diameter phase plates was used to launch a smooth and well defined laser pulse onto the GeO_2 targets. For the experiments, three different drive laser energies of 7.7 J, 14,5 J and 31.2 J were applied.

VISAR analysis

Pressures were determined with the VISAR at the MEC end-station (Fig. 3.17). For some of the experimental runs, 100 µm LiF windows were glued on the rear surface of the GeO_2 samples. Hence, one was able to conduct impedance matching calculations with given equation of state for LiF [9] and GeO_2 [142]. From VISAR analysis, peak pressures of 19(5) GPa, 53(9) GPa and 104(12) GPa were determined for the three applied laser energies. The uncertainties of the VISAR measurements were typically between 11-25 %, derived from the uncertainties of the velocity profiles (Fig. 3.17) and impedance matching calculations.

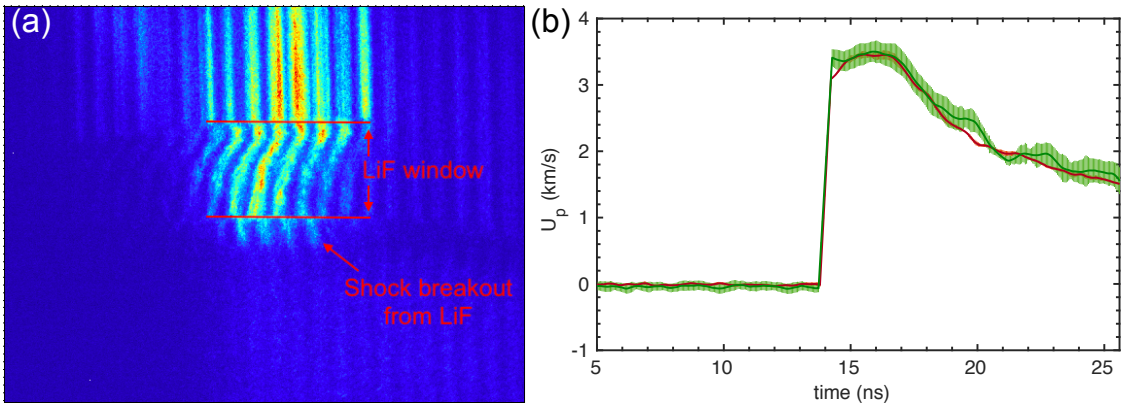

Figure 3.17: (a) VISAR image and (b) outline of shock compressed GeO_2. Shown in the VISAR image is fringe shift within the LiF window and the subsequent shock breakout. The uncertainty of the particle velocities from the VISAR image are shown in green in the VISAR outline.

X-ray diffraction

From the obtained XRD images, azimuthally integrated XRD pattern of the driven GeO_2 runs were derived and are shown in Figure 3.18. At 19(5) GPa, initially ambient quartz-

like GeO_2 transforms to the high pressure rutile structure (Fig. 3.18, indicated as ”r”). In the two diffraction outlines in can be shown, that at an early time delay (-1.5 ns before shock breakout), only the ambient GeO_2 Bragg reflections are observed. This indicates, that the sample is incompletely compressed. At a later time delay (-0.5 ns before shock breakout), four distinct new peaks are emerging. These peaks are located at 2θ angles of ∼21.5°, ∼27.1°, ∼30.9° and ∼42.4°, which can be indexed to the (110), (101), (111) and (220) Bragg reflections of the rutile structure.

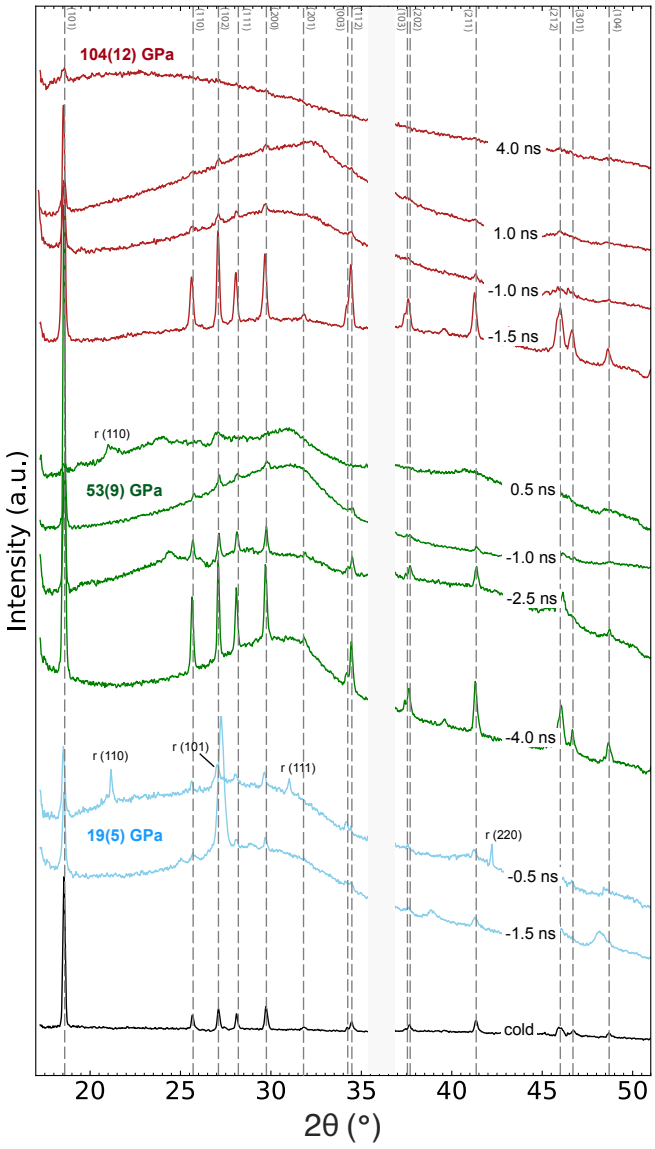

Figure 3.18: XRD multiplot of shock compressed GeO_2. Shown are ambient data (cold) as well as XRD pattern at various time delays at three peak pressures of 19(5) GPa, 53(9) GPa and 104(12) GPa. Indicated are the ambient peak positions of GeO_2 (dashed lines) as well as Bragg reflections of the rutile structure (r). The gray band depicts a detector gap.

At a higher peak pressure of 53(9) GPa Bragg reflections of the ambient GeO_2 structure

at early delay times (-4.0 ns and -2.5 ns before shock breakout) are still present. However, as the driven samples are probed closer to the shock breakout, (hence, when the sample is completely compressed) a decrease in peak intensities of the ambient phase and an increase of an amorphous (melt) structure can be shown. One nanosecond before the shock breakout (-1 ns), the ambient GeO_2 peaks have almost entirely vanished and solely a broad amorphous feature can be observed. This is an indication of the onset of shock induced melting of GeO_2. After shock breakout, a distinct peak at a 2θ angle of $\sim 21^\circ$ is re-emerging. This peak is indexed to the (110) Bragg reflection of the rutile structure.
At the highest experimental peak pressures of 104(12) GPa, one can observe a transition of ambient GeO_2 at early delay times (-1.5 ns relative to the shock breakout) to a melt structure close to the vicinity of the shock breakout (-1 ns to 1 ns relative to shock breakout). Ultimately, at late time delays on the release (4 ns after shock breakout), a bulk feature with various low intensity peaks of the ambient GeO_2 structure is shown.

Structure factor and pair distribution functions

The structure factor of shock compressed GeO_2 was furthermore calculated, to gain information about inter-atomic properties (e.g. bonding and coordination) of the crystalline and melt structure at respective pressures. The structure factor S(Q), which is related to coherent scattering from the sample, can be described as

$$S(Q) = \frac{I^{coh}(Q)}{N f^2(Q)} \tag{3.21}$$

with N as the number of atoms, f as the atomic form factor and I^{coh} as the coherent X-ray scattering.
Through Fourier transformation of S(Q), one can obtain the expression

$$F(r) \equiv 4\pi r \left[\rho(r) - n\right] \tag{3.22}$$

with n as the average density (number density) of GeO_2 and r the radial distance from a reference atom. Here, *F(r)* is limited by the experimental finite maximum of Q_{max} at LCLS of ~ 6 Å^{-1}.
From *F(r)* one can obtain the radial distribution function

$$g(r) = 1 + \frac{1}{4\pi r n} \int_0^{Q_{max}} Q(S(Q) - 1) \sin(Qr) dQ \tag{3.23}$$

with n as the number density from the GeO_2 shock Hugoniot, which is based on the pressure during compression. Density is taken from [142] and converted into number density whereas Q is expressed as $4\pi \sin\theta/\lambda$.

The structure factors and radial distribution functions were calculated using the software package *PDFgetX3* [143]. Prior to the calculation of S(Q) and g(r), the background from a "dark shot" (only X-rays) was subtracted. Furthermore, some experimental runs were conducted only with epoxy resign, to obtain information about the compressed scattering signal of the kapton ablator + epoxy. This signal was also subtracted from the overall scattering of the experimental runs.
A representative plot of the structure factor is shown in Figure 3.19. Here, two dominant peaks can be observed at ∼2.4 Å $^{-1}$ and ∼4.7 Å $^{-1}$. This is in great accordance to experimental static data at similar pressures [49].

Figure 3.20 illustrates the resulting radial distribution functions of shock compressed GeO_2 at ambient state and pressures of 19(5) GPa, 53(9) GPa and 104(12) GPa. The first and second peak of g(r) is considered to represent the Ge-O and Ge-Ge distance (Å), respectively. In this work, an increase of the Ge-O distance from 1.73 Å at ambient state to 1.83 Å at 19(5) GPa can be observed. Further, Ge-O distance decreases at higher pressures to 1.77 Å at 53(9) GPa and 104(12) GPa, respectively. The second (Ge-Ge distance) peak increases from 3.08 Å at ambient conditions to 3.24 Å at 19(5) GPa. At 53(9) GPa and 104(12) GPa, this value decreases again to 3.04 Å and 3.08 Å , respectively.

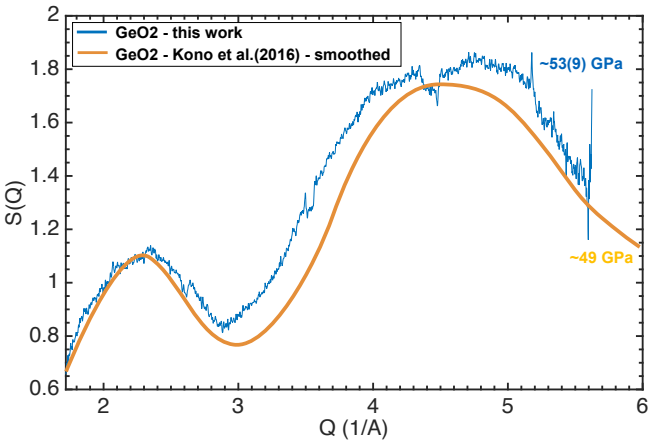

Figure 3.19: Structure factor S(Q) of GeO_2 at 53(9) GPa compared to literature data at comparable pressure [49].

Moreover, to quantify the change in coordination of GeO_2, one can use the calculated pair distribution function to obtain the coordination number of each structure with the use of the equation:

$$CN = 2 \int_{r_0}^{r_{max}} 4\pi\rho g(r) dr \tag{3.24}$$

with r_0 and r_{max} being the left edge position and the peak position of the first peak of g(r) and ρ the number density. Here a change in the coordination number from 4 at ambient state to 5.8 at 19(5) GPa and 53(9) GPa, respectively can be demonstrated. At 104(12) GPa, a further increase of the coordination number to 6.9 is shown (Tab. 3.8).

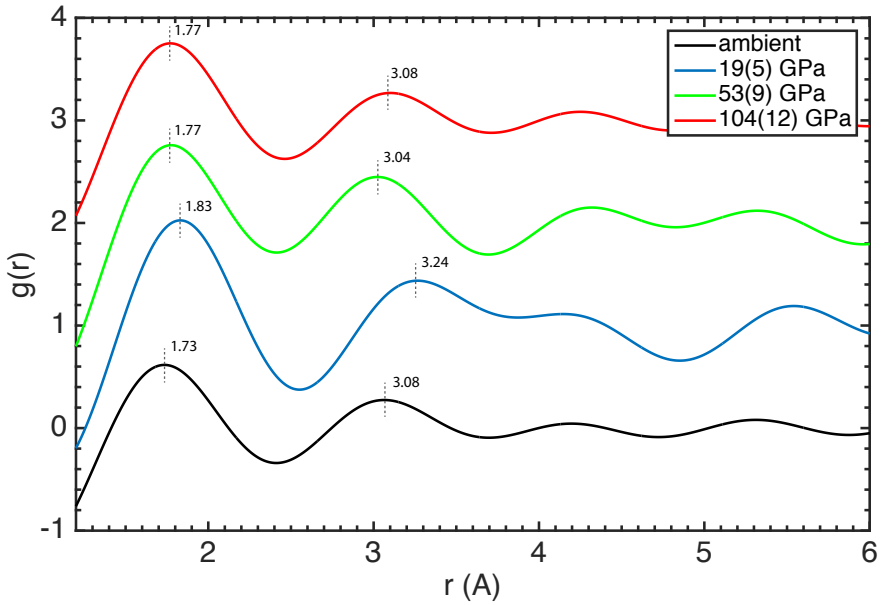

Figure 3.20: Calculated pair distribution functions of GeO_2 at ambient state, 19(5) GPa, 53(9) GPa and 104(12) GPa, derived from this work. Indicated are furthermore the maxima of the first and second peak, which represent the Ge-O and Ge-Ge distances.

Table 3.8: Experimental pressure conditions and the results of the first (r1) and second (r2) peak positions of g(r) and the coordination number CN.

Pressure (GPa)	r1 (Å)	r2 (Å)	CN
ambient	1.74(2)	3.06(6)	4.0(4)
19(5)	1.83(3)	3.27(8)	5.8(9)
53(9)	1.78(4)	3.02(9)	5.8(9)
104(12)	1.77(3)	3.10(8)	6.9(9)

3.1.4 Shock melt and release experiments of α-quartz, α-cristobalite and fused silica

A series of shock compression experiments were conducted to elucidate the melt and shock release behavior of single crystal α-quartz, polycrystalline α-cristobalite and amorphous fused silica. The experiments were carried out at the MEC end-station of LCLS and the BL3:EH5 end-station of SACLA. At MEC, 35 μm thick single crystal α-quartz (c-cut) and 35 μm thick amorphous fused silica windows were used. At BL3:EH5, 15 μm thick single crystal α-quartz and 20 μm thick polycrystalline α-cristobalite samples were investigated. Laser power at MEC and BL3:EH5 was each set to a maximum, to

Table 3.9: Experimental run conditions from this work with used targets (s.c. = single crystal, p.c. = polycristalline), as well as time delay (ns) and observed XRD features.

Run#	target	time delay (ns)	observed XRD feature
LCLS253	quartz (s.c)	5	single crystal reflections
LCLS254	quartz (s.c)	6	melt feature
LCLS256	quartz (s.c)	80	increasing p.c. qz reflections
LCLS257	quartz (s.c)	200	maximum p.c. qz reflections
SACLA795601	quartz (s.c)	5	single crystal reflections
SACLA795590	quartz (s.c)	10	melt feature
SACLA796463	quartz (s.c)	30	onset p.c. qz reflections
SACLA795606	quartz (s.c)	50	increasing p.c. qz reflections
SACLA795603	quartz (s.c)	80	maximum p.c. qz reflections
SACLA796521	cristobalite (p.c)	7	poly-crystalline reflections
SACLA795961	cristobalite (p.c)	13	melt feature
SACLA796504	cristobalite (p.c)	65	increasing p.c. crist. reflections
SACLA796501	cristobalite (p.c)	80	maximum p.c. crist. reflections
LCLS62	fused silica	6	amorphous
LCLS154	fused silica	7	melt feature
LCLS150	fused silica	50	amorphous
LCLS151	fused silica	80	amorphous
LCLS152	fused silica	150	amorphous
LCLS153	fused silica	250	amorphous

ensure sufficient high pressures and temperatures to reach the liquidus regime of the individual targets. At MEC, laser power was set to 6.3 TW/cm^3 in a 10 ns top hat drive laser pulse, which resulted in peak pressures within α-quartz and fused silica of 159(13) GPa and 126(12) GPa, respectively. At BL3:EH5, laser power was set to a maximum of 1.5 TW/cm^3 in a 5 ns top hat drive laser pulse. Because the α-quartz targets were only 15 μm thick and coated directly with 22 μm thick CH, one was still able to compress the samples with the relative low laser power up to a maximum pressure of 119(18) GPa. α-Cristobalite was driven to a maximum pressure of 70(9) GPa. The particle velocity U_p for each experimental drive was determined by the VISAR of each beamline and peak

pressures where calculated with the concomitant use of the impedance matching method. Furthermore, X-ray diffraction was used during shock transit to confirm the melting at each peak pressure. Timing of the X-rays was set according to the peak compression of the sample (close to the shock breakout) and at late time delays of up to 250 ns after laser impact. The scattering signal of the melt and the released samples allowed to gain information about the respective amorphisation or solidification at decreasing pressures and temperatures. An overview about the individual targets, delay times and observed XRD features is given in Table 3.9.

α-Quartz

Figure 3.21 displays four representative XRD images of the ambient state, shock induced melting and release of α-quartz at various time delays. Those are furthermore displayed as azumithally integrated XRD outlines in Figure 3.22. In the ambient XRD pattern of

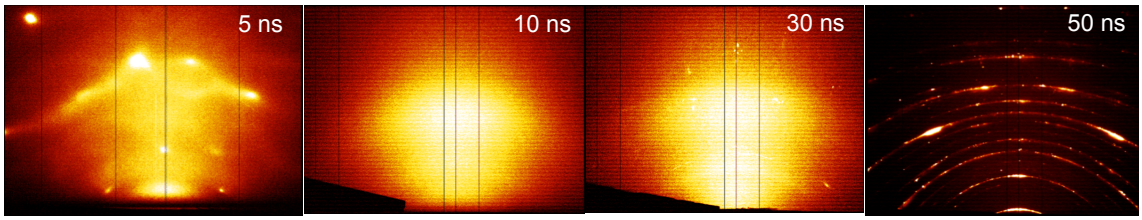

Figure 3.21: X-ray diffraction images of shock compressed α-quartz at various delay times.

the experiments at MEC, a single crystal α-quartz reflection (302) can be observed (Fig. 3.22a). Furthermore, Bragg reflections of the aluminum coating is shown. These peaks vanish at a later time delay of 6 ns, at with only an amorphous broad peak is exhibited at a 2θ angle of ∼30°. At time delays of 80 ns and 200 ns, respectively, Bragg reflections can be observed again and are indexed to polycrystalline α-quartz. Here, the intensity of the Bragg reflections are increasing with later time delays.
From the experimental campaign on α-quartz at BL3:EH5, a transformation from single crystal α-quartz at ambient state to an amorphous melt structure at a time delay of 10 ns is shown (Fig. 3.21b). The ambient α-quartz is indexed by the two single crystal (302) and (312) Bragg reflections whereas the amorphous structure is only exhibited by two distinct broad features at 2θ angles of ∼21° and ∼48°. At 30 ns time delay, the emergence of polycrystalline α-quartz Bragg reflections can be observed. The intensity of these polycrystalline α-quartz Bragg reflections are increasing at 50 ns and 80 ns, respectively.

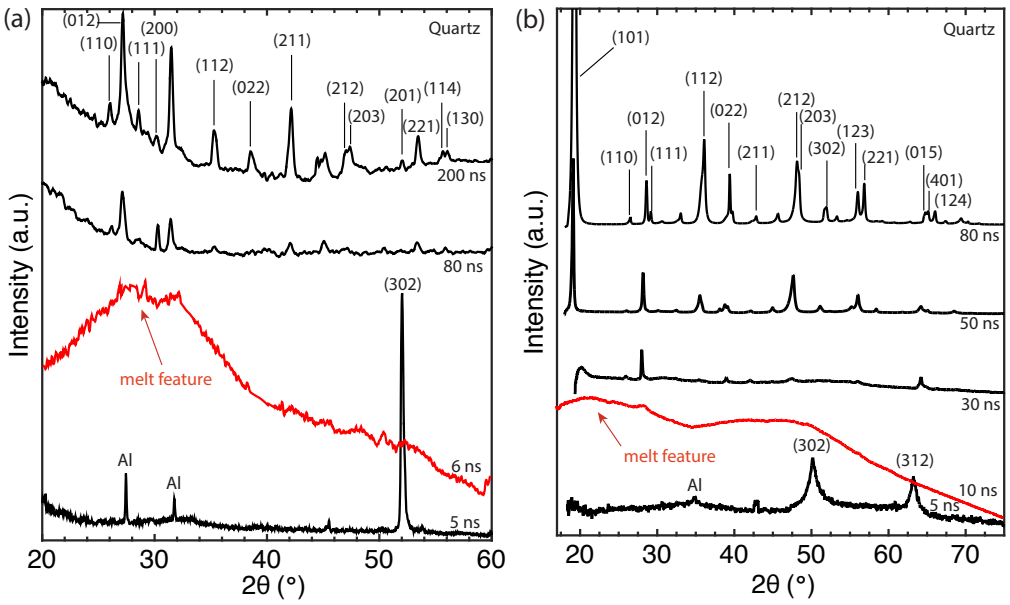

Figure 3.22: X-ray diffraction pattern of shock compressed α-quartz at various delay times. Shown are time series from the experimental campaigns at (a) MEC and (b) BL3:EH5. Furthermore given are the indices of α-quartz Bragg reflections at ambient and release conditions, as well as the observed melt feature from XRD (red line).

α-Cristobalite

Figure 3.23 depicts four XRD images of ambient-, shock molten- and released α-cristobalite at various time delays. From the azimuthally integrated XRD images (Fig. 3.25a) one can observe a transformation of polycrystalline α-cristobalite to an amorphous (melt) feature at a time delay of 13 ns. Here, a broad feature at a 2θ angle of ∼32° is apparent, which can be associated to the signature of the shock compressed kapton ablator. This signature depicts the (111) Bragg reflection of diamond, which originates from highly compressed carbon from the CH dissociation of the ablator, which has been also observed in previous experiments (see section 3.1). At time delays of 65 ns and 80 ns, respectively, the emergence of Bragg reflections, associated to the polycrystalline α-cristobalite structure, is shown. The peak intensities of polycrystalline α-cristobalite are increasing at later time delays.

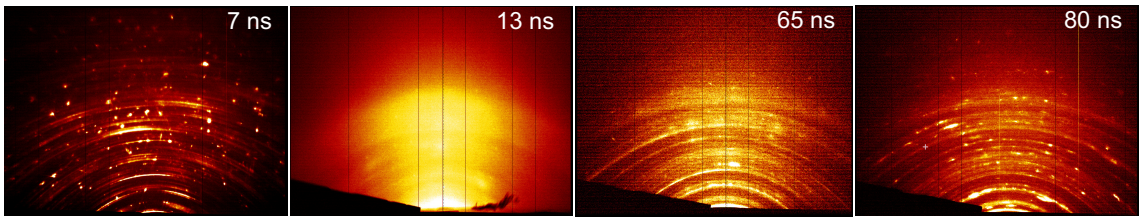

Figure 3.23: X-ray diffraction images of shock compressed α-cristobalite at various delay times.

Fused silica

XRD images of shock compressed fused silica with regard to time delay are shown in Figure 3.24. Furthermore, the azimuthally integrated XRD images are given in Figure 3.25b. A shift of the characteristic bright amorphous structure at low 2θ angles from the ambient pre-shocked state towards a broader and more diffused feature at later time delays is demonstrated. From the XRD pattern a broad melt feature at a 2θ angle of ∼32° at a time delay of 7 ns is shown. This broad feature has vanished at a time delay of 50 ns. At very late time delays of 80 ns, 150 ns and 250 ns, one can observe the re-emerging of the aluminum Bragg reflections of the ablator coatings, but no other crystalline phase can be identified.

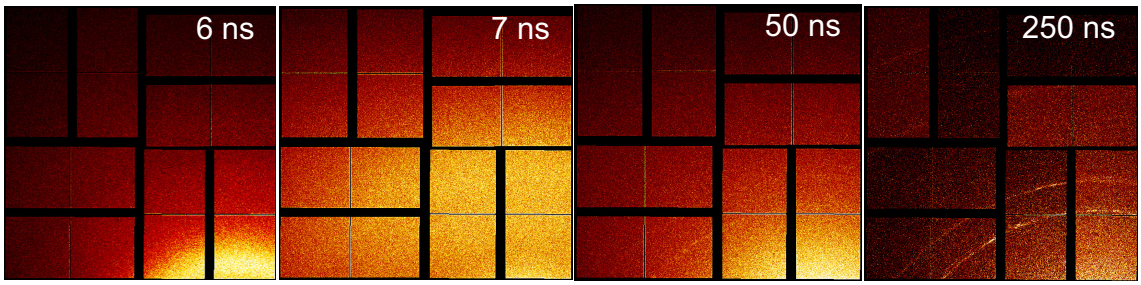

Figure 3.24: X-ray diffraction images of shock compressed fused silica at various delay times.

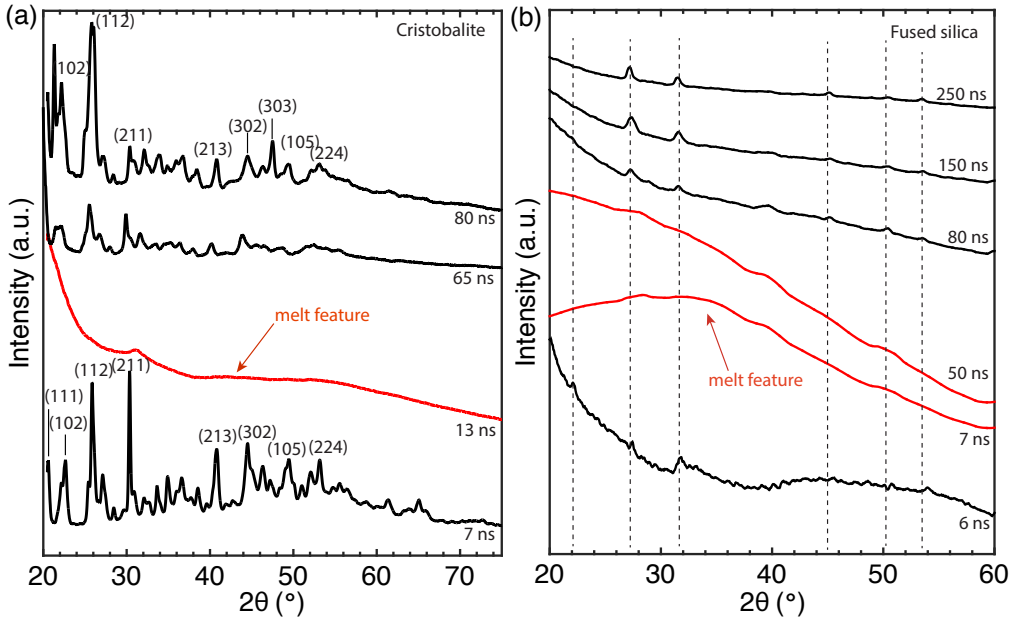

Figure 3.25: X-ray diffraction pattern of shock compressed (a) α-cristobalite and (b) fused silica at various delay times. Shown are time series from the experimental campaign at MEC with given indices of ambient and release conditions, melt features (red lines) and the Bragg reflections of the Al coatings (dashed lines).

3.2 Dynamic diamond anvil cell experiments

Experiments on α-cristobalite (space group $P4_12_12$) with the (resitive heated) dDAC were conduced to elucidate the effect of compression rate, hydrostaticity and temperature on the phase transitions towards the high pressure polymorphs cristobalite II (Space group *P21/c*), cristobalite X-I ($P2_1/n$) and seifertite (*Pbcn*). Different (de-)compression rates and holding times were used in the experiments on powder samples and single crystals. The experimental run conditions are shown in Table 3.10.

3.2.1 Dynamic compression of powder α-cristobalite

Figure 3.26 displays four representative diffraction images of a dynamic compression experimental run with powdered α-cristobalite as starting material. Indexed are the Bragg reflections from ambient α-cristobalite (α-C) as well as the high pressure phases cristobalite II (CII), cristobalite X-I (CXI) and seifertite (Sft). Shown are furthermore the reflections of the rhenium (Rh) gasket as well as the gold (Au) pressure standard. Several

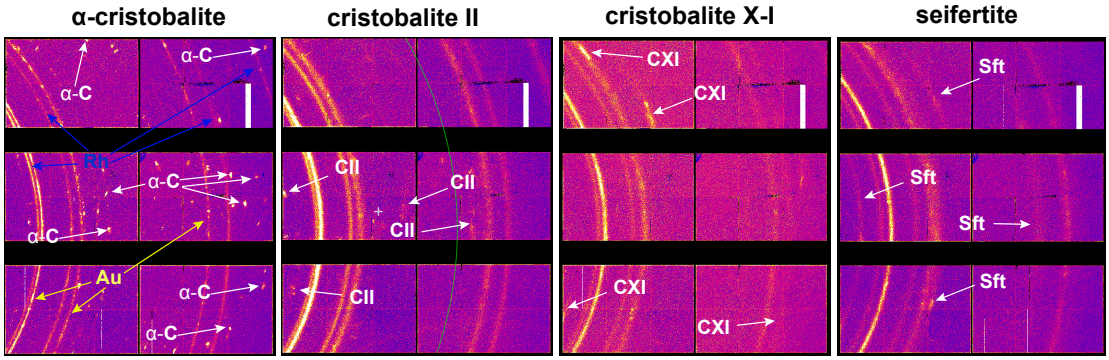

Figure 3.26: X-ray diffraction images of α-cristobalite, cristobalite II, cristobalite X-I and seifertite with corresponding Bragg reflections.

XRD images could be recorded for each experimental run. The XRD images were azimuthally integrated and converted into surface plots, which represent the evolution of Bragg reflections of the sample within the time - 2θ space. The representative surface plot in Figure 3.27 displays a successive 2θ shift of all Bragg reflections during the ramp compression, indicating increasing pressures within the dDAC cell. At 69 GPa, a sudden shift to lower 2θ angles is shown, which indicates the sudden decompression of the sample to a pressure of 21 GPa. Throughout compression, one can observe Bragg reflections of the α-cristobalite, cristobalite II, cristobalite X-I and seifertite structures at different ramp times, which demonstrates the well known phase transformation of α-cristobalite → cristobalite II → cristobalite X-I → seifertite. This was observed in all experimental runs with powder as a starting material.
From the XRD pattern of the experimental runs syn-08, syn06_2, vas0a_run2,

dRHDAC_run1 and dRHDAC_run2, unit cell volumes of seifertite were calculated. Here, corresponding sefiertite Bragg reflections were fitted using the Savitzky-Golay function and unit cell parameters were obtained. The intensity and abundance of the Bragg reflections of cristobalite II and cristobalite X-I were not sufficient to calculate unit cell volumes (Fig. 3.28). Here, the weak scattering of the sample decreased drastically the signal-to-noise ratio and consequently, a refinement analysis reached its limit.

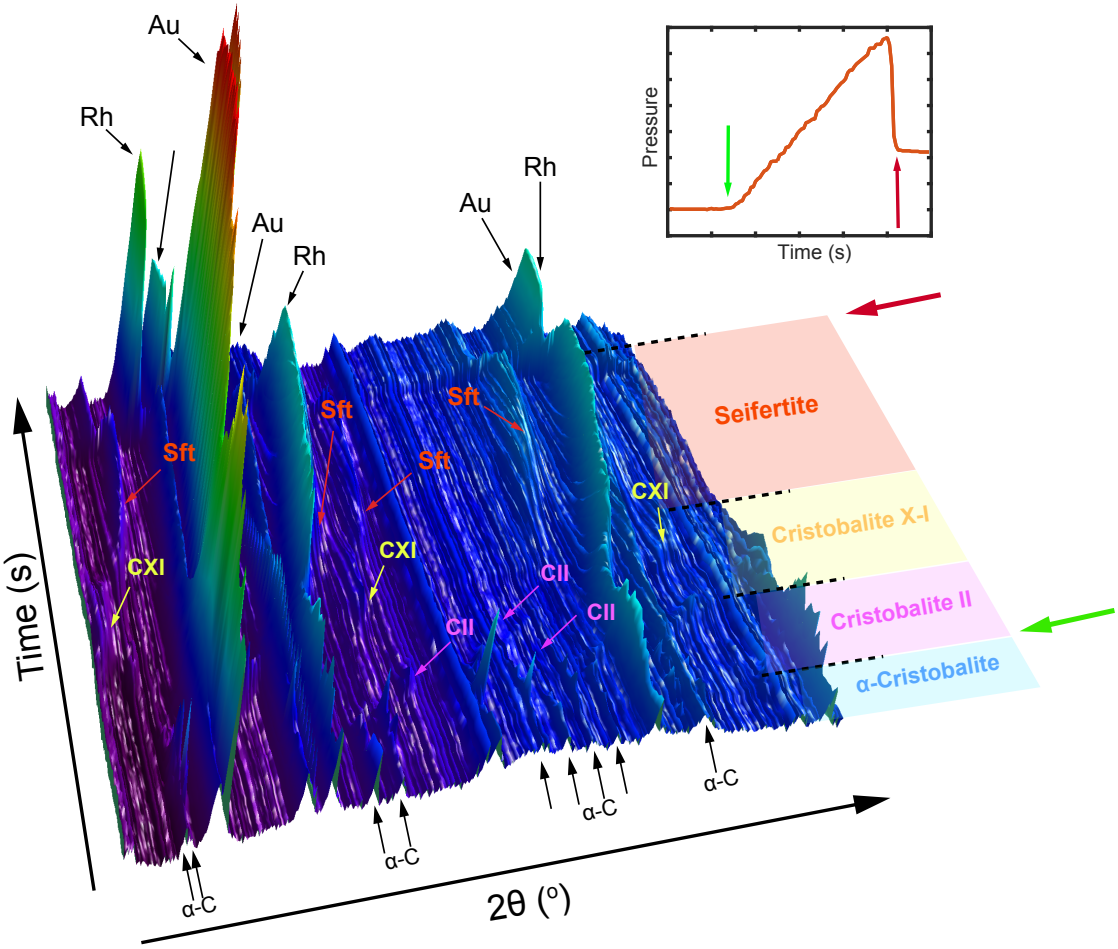

Figure 3.27: Representative 3-D surface plot exhibiting the effects of dynamically, rapid compression of α-cristobalite consisting of a series of integrated X-ray diffraction patterns. Pressure increases with time upwards in a 0.07 GPa/s experiment. Arrows identify individual peaks from α-cristobalite (α-C), cristobalite II (CII), cristobalite X-I (CXI), seifertite (Sft), the pressure marker (Au) and the gasket material (Rh).

Structural response to compression rate

The phase transition pressure onset was investigated with regard to different compression rates (low, intermediate and fast, Tab. 3.10). From dynamic compression of α-cristobalite using powder as a starting material, one can observe a phase transformation of α-cristobalite to cristobalite II between 0.5 GPa and 1 GPa within all experimental

Table 3.10: Summary of the experimental conditions of the dDAC experiments on α-cristobalite.

Run	sample	P_{start} (GPa)	P_{max} (GPa)	Total acquisition time (s)	Compression rate (GPa/s)	Hold at P_{max} (s)	P_{end} (GPa)	Decompression rate (GPa/s)
syn-08	powder	0	69	1000	0.07	0	21	0.96
syn11	powder	0	73	1000	0.02	0	73	N/A*
syn06_2	powder	18	106	1000	0.25	333	17	1.18
p2sv14	powder	0	57	1000	0.17	333	43	0.05
vas0a_run2	powder	0	66	1000	0.41	320	40	0.05
syn11_run2	powder	0	92	3000	0.19	320	41	0.03
dRHDAC_run1[a]	powder	5	101	300	0.27	0	83	3.23
dRHDAC_run2[b]	powder	3	114	300	0.17	0	103	2.21
p2sv13	sin.crys.	14	82	1000	0.07	0	21	3.11
p2sv13_run2	sin.crys.	21	31	1000	0.01	0	31	N/A*

[a]resistive heated to 500 °C and [b]700 °C; * diamonds broke

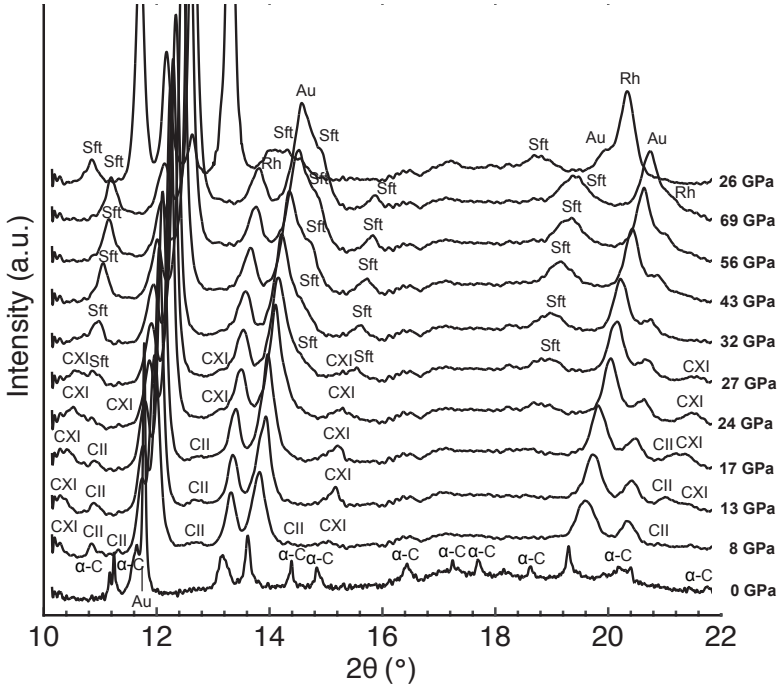

Figure 3.28: Selected X-ray diffraction pattern of the structural evolution of α-cristobalite during dynamic compression in experiment Syn-08 (compression rate 0.07 GPa/s). Indicated are α-cristobalite (α-C), cristobalite II (CII), cristobalite X-I (CXI), seifertite (Sft) The top diffraction outline depicts the rapid decompression of the dDAC to 26 GPa, from which seifertite can still be observed.

runs, independent of the compression rate. The occurrence of Bragg reflections of the cristobalite X-I phase can be observed at ∼5-7 GPa for the low compression rate runs (syn-11 and syn-08), at ∼7-9 GPa for the intermediate compression rate runs (p2sv14 and syn11_run2) and at ∼11 GPa for the fast compression rate run (vas0a_run2). For the experimental run syn06_2, the initial pressure in the cell was already equilibriated at ∼18 GPa, at which only the cristobalite X-I structure could be detected. First seifertite Bragg reflections were observed at ∼23-28 GPa for the low compression rate runs (syn11 and syn-08), at ∼28-31 GPa for the intermediate compression rate runs (p2sv14 and syn11_run2) and at ∼32-35 GPa for the fast compression rate runs (syn06_2 and vas0a_run2).
No transformation to a low pressure phase could be detected during decompression of all experimental runs to finite end pressures between 17 GPa to 73 GPa (Tab. 3.10) Independent of the decompression rate, the end product of the decompression runs could always be indexed to the seifertite structure. It should be noted, however, that at pressures below 17 GPa, this might not be the case anymore, but due to the experimental limitations (diamonds breaking and remaining pressure within the DAC), could not be further investigated.

The unit cell volume ($Å^3$) was calculated with respect to pressure (GPa) for three different experimental runs (Fig. 3.29). At a slow compression rate (0.07 GPa/s, Syn08), unit

cell volumes at respective pressures are in good agreement to static data [28]. However, molecular volumes derived from the slow compression rate experiment deviate from unit cell volumes of the experimental run at a faster compression rate (0.25 GPa/s, Syn06_2). The unit cell volumes at respective pressures of the experimental run with a slow compression are smaller compared to volumes derived from the fast compression rate run. This deviation increases in particular at higher pressures to $\sim$0.5 Å ^{3} per formula unit. In the experimental run with the highest compression rate (0.41 GPa/s, vas0a_run2), unit cell volumes at respective pressures are much larger compared to the slow and intermediate compression rate runs and static data, but converge towards smaller volumes during holding time.

Figure 3.30 depicts the volume strain of seifertite with regard to pressure for the three experimental runs. Here, the volume strain is strongly dependent on the compression/decompression rate. During fast compression (vas0a_run2), the volume strain of seifertite is lower (1-2%) compared to experiments with slow or intermediate compression rates (Syn08 and Syn06_2). During decompression, it can be demonstrated, that an almost instantaneous decompression (Syn06_2) leads to a much larger (1-3%) volume strain compared to slow decompression rate runs at respective pressures. The volume strain of seifertite derived from experimental run Syn06_2 converges towards smaller values, comparable to the slow decompression runs, only at low pressures and long holding times.

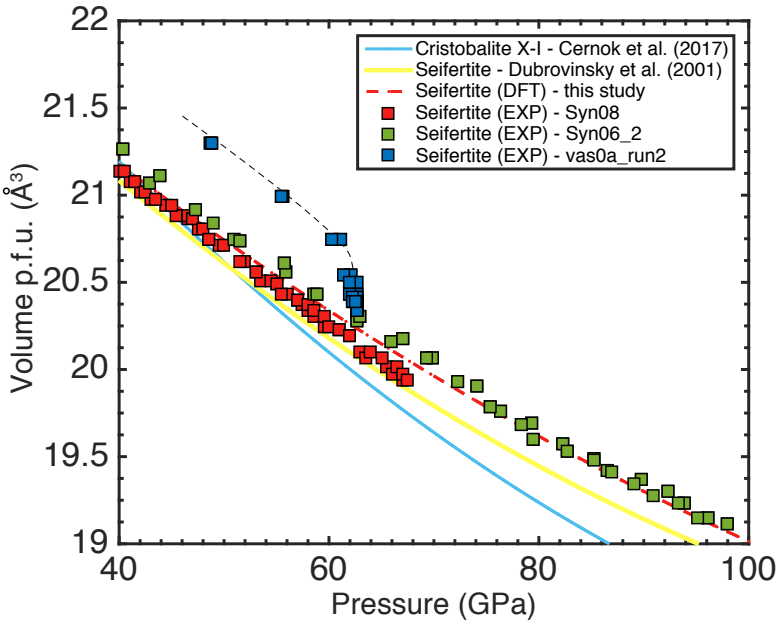

Figure 3.29: Molecular volume per formula unit of seifertite as a function of pressure. Shown are experimental results from three different experiments (Syn-08, Syn06_2 and vas0a_run2) with respective compression rates (0.07 GPa/s, 0.25 GPa/s and 0.41 GPa/s, respectively). Furthermore indicated are results from ground state DFT calculations of seifertite and published data of seifertite and cristobalite X-I at various pressure points.

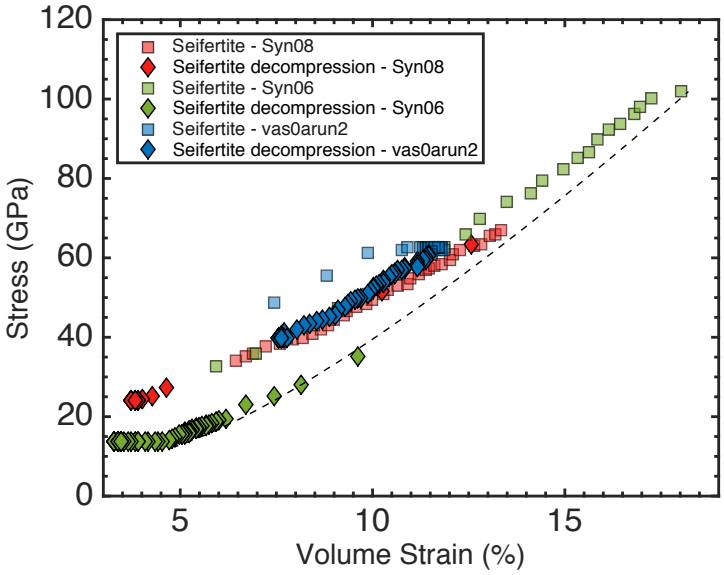

Figure 3.30: Volume strain with regard to pressure during compression and decompression of Syn-08, Syn06_2 and vas0a_run2.

Ground state calculations

Next to obtained refined unit cell data, DFT calculations on the unit cell volumes of seifertite at pressures between 40 GPa and 100 GPa were conducted. For the simulations, the relaxation of the cell at various external pressures with 96 atoms (32 Si and 64 O) in a $2\times2\times2$ orthorhombic supercell was performed. Here, Γ centered k-points were used to sample the entire Brillouin zone. A good compromise between accuracy and computational speed was found for the plane-wave expansion of the Kohn-Sham orbitals with a cutoff of 70 Ry. The simulations made use of PAW pseudopotentials and the PBE approximation as the exchange correlation functional. The BFGS quasi-newton algorithm, implemented in the Quantum Espresso suite is based on the trust radius procedure and was used for structural relaxation. All simulations were conducted at room temperature.
The results of the DFT ground state calculations of seifertite are in great agreement to calculated molecular volumes from literature data (e.g. [28]) at lower pressures between 40 GPa and 60 GPa (Fig. 3.29). However unit cell volumes calculated from DFT deviate from literature data at higher pressures of up to 0.8 %.
The results from first principle calculations agree well with the experimental results from this work on seifertite at slow (0.07 GPa/s)- and moderate compression rates (0.25 GPa/s), but deviate strongly for results from fast compression rates (0.41 GPa/s) (Fig. 3.29).

3.2.2 Resistive heated experimental runs

α-Cristobalite was furthermore resistively heated within the RHdDAC to maximum temperatures of 500 ($\pm$50) °C and 700 ($\pm$100) °C, respectively. Here, the cells were heated in

100 °C successive temperature steps up to a maximum temperature. Subsequently, cells were ramp compressed with a compression rate of 0.27 GPa/s (dRHDAC_run1) and 0.17 GPa/s (dRHDAC_run2) to a maximum pressure of 101 GPa and 114 GPa, respectively. The applied temperatures within the cell led to an increase of the internal pressure at each temperature step. The pressure increase was accompanied by phase transformations from α-cristobalite towards cristobalite II, cristobalite X-I and seifertite, which was observed in the XRD pattern (Fig. 3.31).

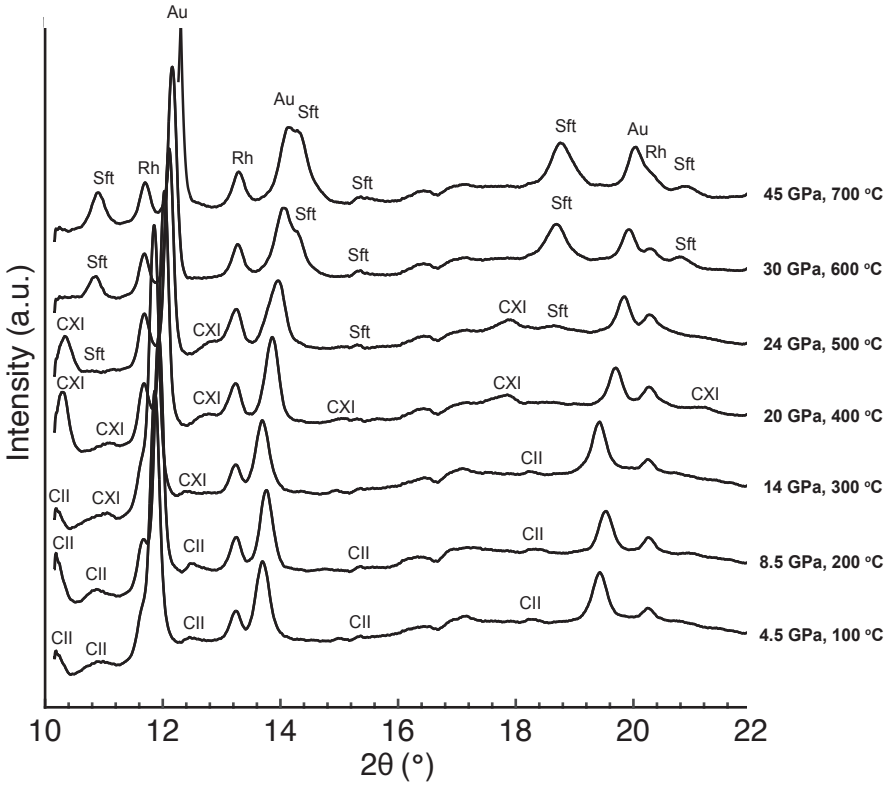

Figure 3.31: The structural evolution of α-cristobalite during resistive heating of experiment dRHDAC_run2. Here it can be shown, that structural transformations are appearing during heating and subsequent pressure increase within the cell.

In the experimental run dRHDAC_run1, the starting pressure in the cell at room temperature was 5 GPa. At this pressure, Bragg reflections of the sample could be associated to the cristobalite II structure. At 100 °C, pressure had increased to 7 GPa and sample reflections could still be indexed to cristobalite II, with no other phases observed. At a temperature of 200 °C, pressure had increased to 10 GPa with intensities of the Bragg reflections of cristobalite II decreasing. At 300 °C, pressure increased to 11.5 GPa and Bragg reflections of cristobalite II had almost vanished, however, no other phases were observed in the XRD pattern. At 400 °C, pressure had risen to 14.5 GPa and Bragg reflections of cristobalite X-I were emerging. The intensity of the cristobalite X-I reflections increased at 500 °C, at which pressure had risen to 18.5 GPa. The first diffraction image of the dDAC ramp compression was then acquired after around $\sim$20 minutes at which the

pressure had been further increased to 24 GPa. Here, Bragg reflections of the sample was indexed to the seifertite structure. The reflections of seifertite can be observed throughout the complete ramp compression run up to 101 GPa as well as the decompression to an end pressure of 83 GPa.

Starting pressures within the RHdDAC cell at room temperature of experimental run dRHDAC_run2 was 3 GPa. Similar to dRHDAC_run1, Bragg reflections of the sample could be indexed to the cristobalite II structure. At 100 °C and 200 °C, pressure within the cell had increased to 4.5 GP and 8.5 GPa, respectively, and the present Bragg reflections were still indexed to cristobalite II. At 300 °C and 14 GPa, however, first cristobalite X-I reflections were emerging and at 400 °C and 20 GPa, only reflections of the cristobalite X-I structure was demonstrated. At 500 °C, pressure had risen to 24 GPa and first Bragg reflections of the seifertite structure were indexed. At 600 °C and 700 °C, pressures within the cell had increased to 30 GPa and 45 GPa, respectively and Bragg reflections of the sample could only be associated to the seifertite structure, with no other structures observed (Fig. 3.31). The first XRD image of the ramp compression was acquired at 66 GPa. Up to 114 GPa, only the seifertite structure was indexed. Decompression of the sample to an end pressure of 103 GPa revealed no further phase transformation.

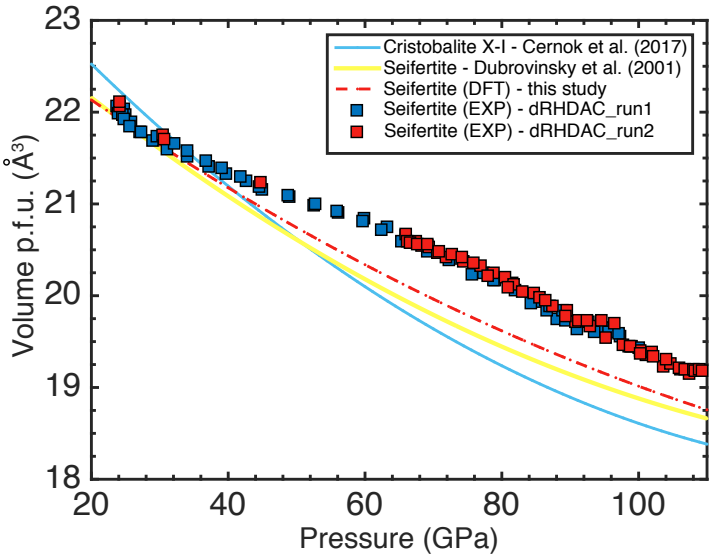

Figure 3.32: Molecular volume of seifertite as a function of pressure from experimental runs dRDAC_run1 and dRDAC_run2. Furthermore indicated are the results from ground state DFT calculations of seifertite and literature data of seifertite and cristobalite X-I at various pressure points. Here, the molecular volume from the experimental runs with the RHdDAC is deviating strongly from results of seifertite from static or dDAC experiments.

Unit cell volumes of seifertite during dynamic compression up to maximum pressures of 101 GPa (dRDAC_run1) and 114 GPa (dRDAC_run2) reveal increasingly larger values compared to static and theoretical DFT data (Fig. 3.32). Between ∼24 GPa and ∼38 GPa, unit cell volumes are similar to static data but deviate strongly at higher pressures

from the equilibrium steady state data (Fig. 3.32). The calculated unit cell volumes of experimental runs dRDAC_run1 and dRDAC_run2 during dynamic compression are comparable. The reason for this might be the slower compression rate of the experimental run (dRHDAC_run2) at higher temperatures compared to faster compression rates at lower temperatures (dRHDAC_run1).

3.2.3 Dynamic compression of single crystal α-cristobalite

To further investigate the effect of hydrostaticity within the dynamic diamond anvil cell during compression of cristobalite, two experimental runs at quasi-hydrostatic conditions with single crystal α-cristobalite and neon as a pressure transmitting medium were conducted. XRD reveals the cristobalite X-I structure upon compression from 14 GPa up to 82 GPa with no intermediate phase transitions. Because the pre-pressure of the dDAC was already at 14 GPa, it is not possible to ascertain, if a prior phase transformation from α-cristobalite towards cristobalite II, and cristobalite II to cristobalite X-I was apparent. The decompression of the sample to 21 GPa did not reveal any phase (re-)transformation towards cristobalite II or α-cristobalite and the diffraction pattern of the sample during a second ramp up to 31 GPa could still only be indexed to the cristobalite X-I structure. From the refined Bragg reflections of cristobalite X-I, unit cell volumes could be calcu-

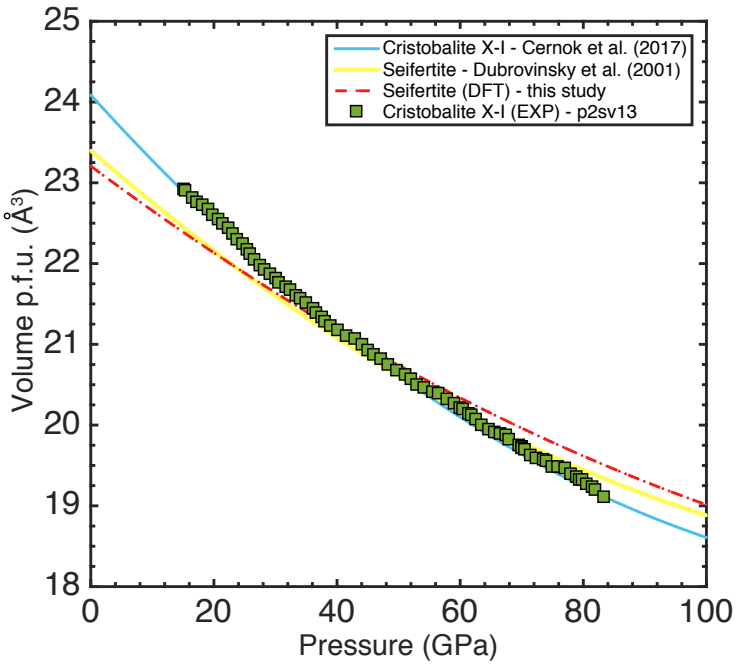

Figure 3.33: Molecular volume of cristobalite X-I as a function of pressure. Shown are experimental results of experiment p2sv13 with a compression rate of 0.07 GPa/s. Furthermore indicated the results from ground state DFT calculations of seifertite and literature data of seifertite and cristobalite X-I at various pressure points. The experimental data of this work is in excellent agreement to literature data from [46]

lated within the entire pressure regime of 14-82 GPa. The unit cell volumes appear to be in excellent agreement to literature data of Ref. [46] (Fig. 3.33).

3.2.4 Metadynamic simulations of α-cristobalite by means of variable cell DFT-MD calculations

In order to elucidate the effect of hydrostaticity on the transformational pathways of α-cristobalite, a metadynamics variable cell DFT-MD simulation was performed. The metadynamics simulations were conducted by means of first principles (*ab initio*)- and vc-md methods, implemented in the Quantum Espresso software package. *Ab initio* calculations were carried out within the DFT formalism, using the generalized-gradient approximation (GGA) for the exchange–correlation energy. A tetragonal super cell with 96 atoms (32 Si and 64 O atoms) were used for the simulations and Γ point sampling for the cell's Brillouin zone integration was chosen. For each value of the applied stresses, the lattice vectors were optimized together with the atomic coordinates. The vc-md runs were conducted at ambient temperatures (300 K), controlled through velocity rescaling. The planewave energy cutoff was set to 120 eV and a total of 19000 time steps, each 0.96 fs (total 9.67 ps) were applied. Because of the metadynamic nature of this study, the vc-md simulations were conducted within a variable cell, either with hydrostatic pressures applied on all three crystallographic axis, or a non-hydrostatic compression in the *c*-crystallographic direction.

The results show, that in the *ab initio* case, α-cristobalite undergoes a phase transformation to a high pressure (hp-cristobalite) phase at $\sim$20 GPa (Fig. 3.34). Further, the *ab initio* simulations predict a structural transformation of the hp-cristobalite phase into sixfold stishovite at $\sim$37 GPa up to $\sim$60 GPa (Fig. 3.35).

In the vc-md simulations, one can observe the same initial transformation from α-cristobalite to hp-cristobalite at $\sim$20 GPa, independent of hydrostatic or non-hydrostatic compression. Subsequently, in the non-hydrostatic case, i.e. when the α- cristobalite unit cell is uniaxially compressed, one can further determine a phase transformation from hp-cristobalite to seifertite at $\sim$28 GPa up to pressures of $\sim$60 GPa (Fig. 3.35). However, in the hydrostatic case one does not observe any further phase transformations from hp-cristobalite to a higher pressure structure (Fig. 3.35).

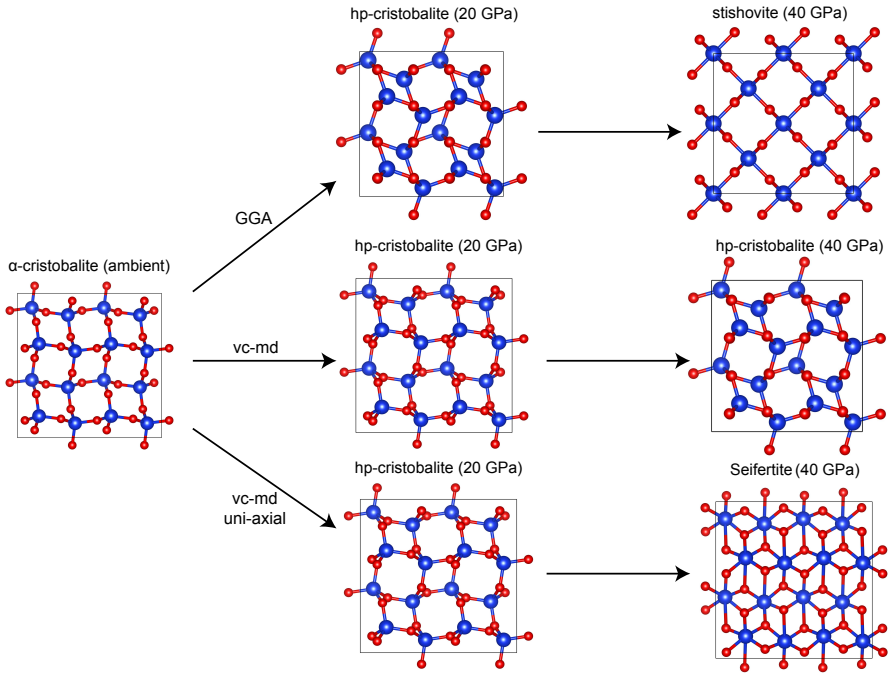

Figure 3.34: Structures of the ambient and high pressure polymorphs of α-cristobalite derived form *ab inito* (GGA) and vc-md simulations. The structures are viewed along the *c* axis at various pressures with the large spheres representing the Si atoms and the small ones the O atoms.

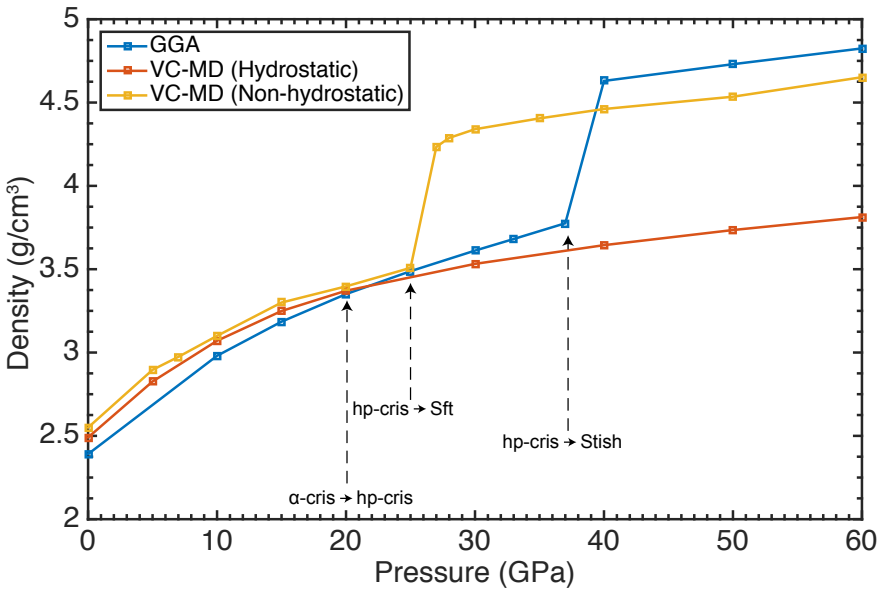

Figure 3.35: Density and structural evolution of α-cristobalite with regard to pressure. Shown is the density from *ab initio* (GGA) and variable-cell molecular dynamics (VC-MD) simulations. The phase transitions are indicated by dashed black arrows.

Chapter 4

Discussion

In this thesis, numerous physical effects on the atomic structure of silicates and GeO_2 were investigated using laser induced shock compression and dynamic DAC experiments. At first, the lattice response towards laser induced shock compression on α-quartz, stishovite and GeO_2 are discussed in chapter 4.1. Subsequently, the melting and post-shock dynamics of α-quartz, α-cristobalite and fused silica as starting materials are dissected with regard to recrystallization and grain growth kinetics during shock release. Next, the effect of fast- and ultra-fast kinetics by means of dynamic DAC and laser shock compression techniques (4.2) as well as the effect of hydrostaticity to high pressure phase transitionson of α-quartz, stishovite and α-cristobalite (4.3) are discussed. This ultimately leads to a new interpretation of the transformation pathways of SiO_2 and GeO_2 and elucidates the concomitant geophysical implications (4.4).

4.1 Material response to laser induced shock compression

4.1.1 α-Quartz

Figure 4.1 summarizes peak pressures and corresponding densities, derived from the *le Bail* refined XRD data (Fig. 3.11). The obtained α-quartz Hugoniot in pressure-density space are compared to experimental data on α-quartz from literature [144, 145, 146, 147, 148, 149, 150, 151] and the stishovite isotherm derived from 300 K static data [20]. The refined densities, obtained in this work, are in excellent agreement to literature values at comparable pressures and support the general α-quartz Hugoniot trend (Fig. 4.1). From this work, the refined density of the stishovite structure at 45(7) GPa exhibits slightly lower densities compared to experimental equilibrium data on the 300 K static stishovite isotherm [20]. The elevated temperatures during shock transit can explain this deviation from the static experimental data at ambient temperatures. At higher pressures, the

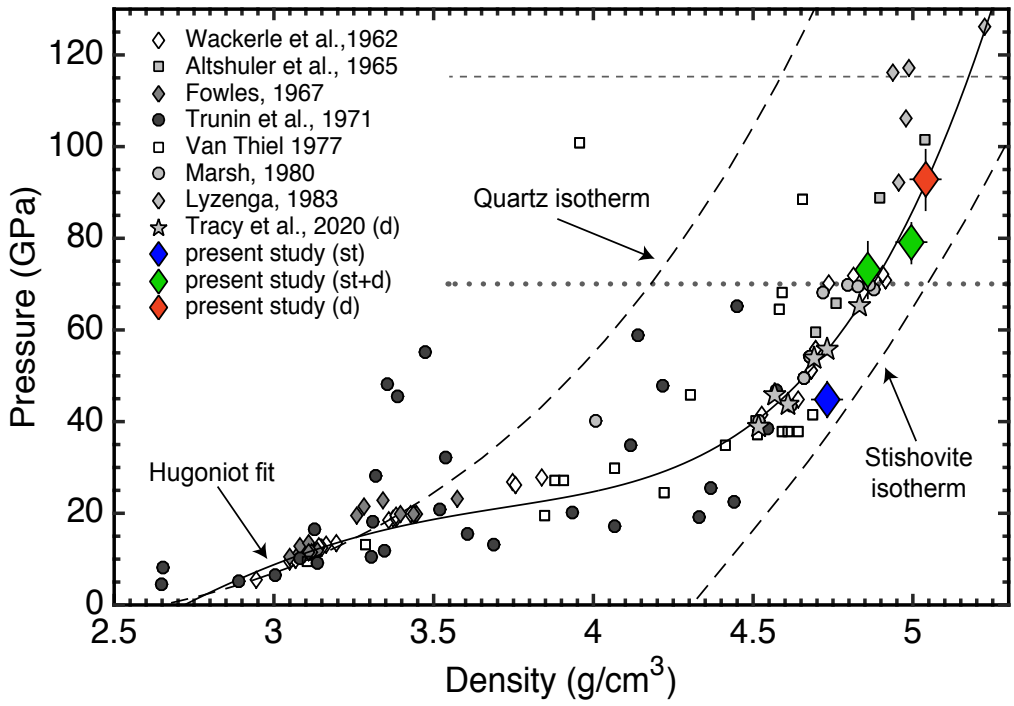

Figure 4.1: Pressure-density plot of α-quartz shock wave data. Shown is the α-quartz shock Hugoniot curve as well as the quartz and stishovite isotherms. Densities derived from this work are indicated as large diamonds. Shown are furthermore the continuum Hugoniot data from laser shock compression experiments [144, 145, 146, 147, 148, 149, 150], gas-gun experiments [151], as well as the 300 K static compression data for stishovite [20]. Horizontal dashed line indicates shock melting conditions, horizontal dotted line equilibrium melting conditions. st: stishovite, d: *d*-NiAs.

d-NiAs mass fraction of the mixed phase between stishovite and *d*-NiAs is increasing and results in overall lower densities compared to pure stishovite on its respective isotherm (Fig. 4.1). As described previously [151], we also observe a denser stishovite structure relative to the *d*-NiAs phase. The density ratio between stishovite and *d*-NiAs (1.01-1.02) is furthermore comparable to static experiments [152] at lower pressures.

Theoretical calculations suggest, that the mass fraction λ of stishovite from shocked α-quartz starts to increase at 15 GPa and will eventually reach $\sim$1 at 46 GPa [107], resulting in a complete transformation to the stishovite structure. The observed phase transformation from single crystal α-quartz to stishovite at 45(7) GPa in this study, is in great accordance to the theoretical assumption. The observations are furthermore comparable to diffraction data from shock compressed fused silica (SiO_2), in which a phase transformation to the stishovite (rutile) structure in laser shock compression experiments was observed at $\sim$33 GPa [100] and between 34 GPa to 64 GPa [153] in a gas-gun experiment. For fused silica it was shown, that the nucleation and growth of the high pressure stishovite phase is a coalescence grain growth due to the homogeneous nucleation [100] and a growth model involving only small-scale atomic motions was proposed [153]. For

α-quartz, there are two likely mechanisms, that would explain the transformation towards stishovite: the first one assumes that the α-quartz-stishovite transformation mechanism is a combination of shear-band melting of α-quartz and recrystallization (progressive bond-bending model [154, 155]). Here, heterogeneous strain results in the deformation of narrow shear zones, which can accommodate much higher temperatures than the bulk sample [156]. During shock transit, the α-quartz structure will be partially amorphized and stishovite nucleates and grows from the heated zones (Fig. 4.2a). The second mechanism is a displacive, martensitic phase transition from α-quartz to stishovite, induced by uniform shear stress in the shocked sample [157], however, the continuous increase in intensity of the Bragg reflections of polycrystalline stishovite (Fig. 3.11, purple lines) would rather suggest a successive nucleation and growth than a martensitic phase transition.

On the α-quartz Hugoniot, at pressures exceeding 70 GPa, a phase transformation towards the $CaCl_2$ structure was assumed [158]. The experimental data obtained in this thesis, did not reveal the $CaCl_2$ structure upon shock loading at 73(13) GPa, but instead a mixed phase between stishovite and defective niccolite (*d*-NiAs) was identified. The increasing intensity of the Bragg reflections during the various X-ray probe times indicate, that this mixed phase is also crystallizing from shear bands (Fig. 4.2b). At 79(9) GPa, the broadening of the stishovite reflections observed in X-ray diffraction most likely indicates an increase in the disordered distribution of the silicon cations in the octahedral sites due to higher temperatures on the shock Hugoniot. The (110) peak of the stishovite diffraction pattern is a result from silicon, filling every other void along the tetragonal <110> direction. A disorder in the silicon sublattice and a destructive interference along this direction, caused by motion due to the reduction of the free energy by the increase in configurational entropy, will effectively reduce the intensity of the (110) peak [151]. A complete disordering of the silicon cations is achieved at 94(14) GPa, at which the (110) stishovite peak has

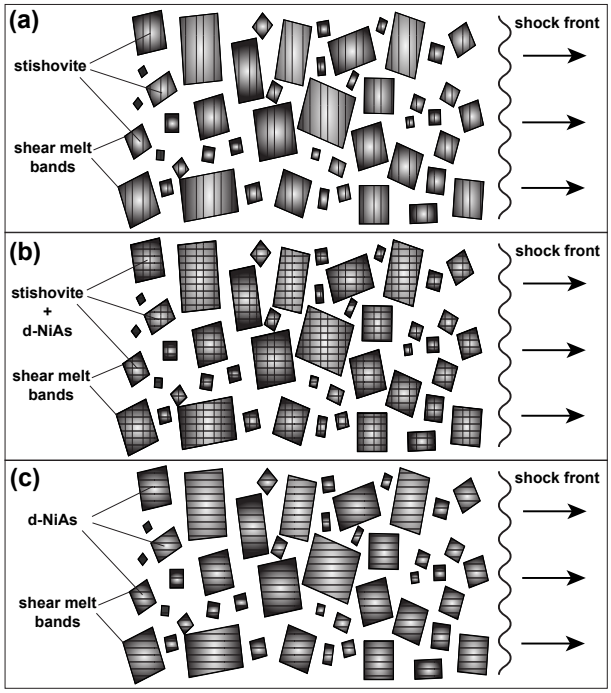

Figure 4.2: Schematic model of shear band melting (modified after [155]) behind the shock front and nucleation/growth of (a) stishovite at 45 GPa and ∼2900 K (b) the mixed phase of stishovite and *d*-NiAs at 73 GPa and ∼4600 K and (c) *d*-NiAs at 94 GPa and ∼5500 K.

vanished and only Bragg reflections of
the defective niccolite structure can be observed. One can assume, that during shock loading, a complete crystallization of stishovite is hindered, resulting in the *d*-NiAs structure (Fig. 4.2c). It should however be noted, that at 94(14) GPa, the sample could not be probed directly at shock breakout (t_{probe} = -0.5 ns relative to the shock breakout) and therefore there might be the possibility, that stishovite peaks are still emerging. However, molecular dynamic simulations [159] indicate that the crystallization of stishovite from quartz takes ∼0.5-5.0 ns and therefore corresponding peaks should already have been observed. In general, one can interpret the high pressure regime (> 70 GPa) of the general α-quartz Hugoniot as a metastable state with *d*-NiAs-type SiO_2 being the primary phase.

4.1.2 Stishovite

The pressures, determined from VISAR, as a function of density, obtained from XRD, are shown in Figure 4.3. They are in excellent agreement with literature data from shock compression experiments [63, 133, 135] and below 128 GPa comparable to static compression experiments[20, 33, 35, 36, 37]. A stishovite structure from the refined diffraction pattern

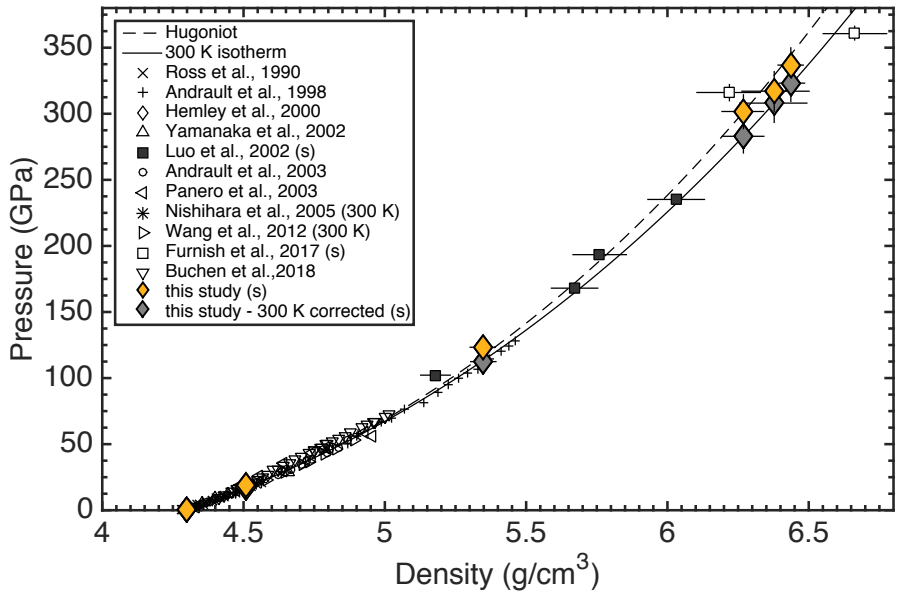

Figure 4.3: Pressure-density experimental data for stishovite (yellow diamonds) and 300 K corrected data (grey diamonds) from this study and literature. (s) indicates shock wave experiments. Drawn are furthermore the stishovite Hugoniot (dashed line) and 300 K isotherm (solid line). Modified after [113].

at 18(2) GPa is well within the stishovite stability field found in static compression experiments [17, 20, 25, 33, 35, 36, 37]. However, a departure from equilibrium behavior is observed at higher pressures: at 123(5) GPa, Bragg reflections of compressed stishovite are still apparent. These conditions are within the equilibrium phase stability field of α-PbO_2 type silica [25, 26, 27, 28, 29, 30, 31], and at 301(12) GPa and 336(13) GPa, P-T

conditions can be associated to the pyrite-type silica stability field [32].
The obtained bulk modulus of stishovite from this study (K_0 = 307 GPa, K_0' = 4.66 GPa) is comparable to published data of shock compression experiments (K_0 = 315 GPa, K_0' = 4.8 GPa and K_0 = 307 GPa, K_0' = 5.0 GPa) [133, 158] as well as EOS studies of stishovite at lower pressure from static DAC experiments (K_0 = 309.9 GPa, K_0' = 4.59 GPa and K_0 = 294 GPa, K_0' = 4.85 GPa) [20, 37]. It seems that this is not only valid at lower

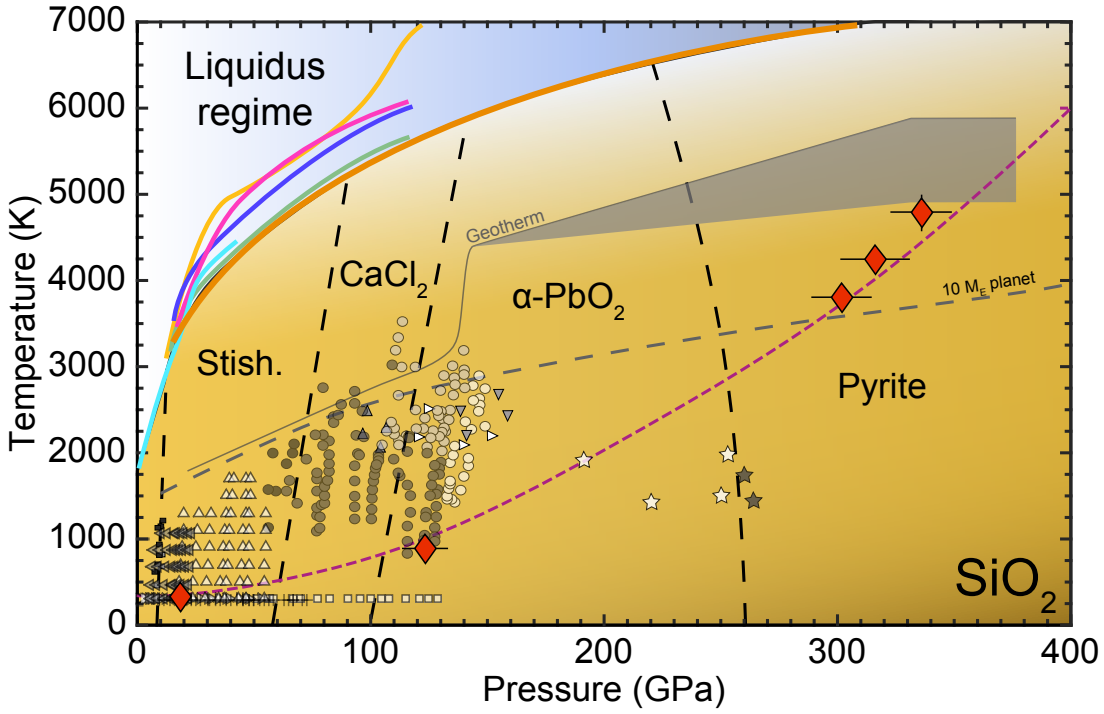

Figure 4.4: SiO_2 phase diagram, modified after [8, 63, 158]. Shown is experimental data where the structure of SiO_2 was resolved. Indicated are the different equilibrium phase stability fields and the geotherms of Earth and terrestrial planets with a mass of 10 M_E. Red diamonds are data from this study and the dashed magenta line indicates the Sesame stishovite EOS 7360 [134]. Shown is data with α-quartz or fused silica as a starting material: black and grey squares from [17], circles from [25], right triangles from [27], lower triangles from [30] and stars from [32] as well as stishovite as a starting material: white squares [19], upper triangles [37], crosses [38] and left triangles [36]. Furthermore melting lines are indicated: brown [63], orange [160], pink [59], blue [161], green [58] and light blue [162, 163]. Modified after [113].

pressures, but continues to be apparent at multi-Mbar pressures [63, 135]. Past studies have interpreted the lack of evidence for a phase transition as i) not being in the right pressure regime, ii) sluggish kinetics, or iii) relatively small changes in structure and energy attending a phase transition and not detectable with diagnostics [133]. Up to now, however, there has been no lattice-level structural information for stishovite under shock compression. By coupling XFEL sources to high-power laser systems, one can now reveal subtle changes in lattice structure during the shock response of materials. The femtosecond diffraction contradicts i) and iii), since Bragg reflections of stishovite can still be

observed in the shock compressed state along the respective Hugoniot at pressures exceeding 300 GPa. Furthermore, the measured lattice parameters do not indicate a change in crystal structure as in a first order transition, in contrast to static data [20, 38] (Fig. 3.15). The stishovite structure of the shock compression experiments of this work above 300 GPa is therefore in vast contrast to static compression experiments: at 123 GPa, there is no indication of a α-PbO_2 phase, which was seen in DAC experiments with SiO_2 [25, 27] and at experimental peak pressures of 301 GPa to 336 GPa there is no indication of the pyrite structure [32] at the ns-timescales of the experiment.

4.1.3 GeO_2

X-ray diffraction of shock compressed GeO_2 reveals two major high pressure phase transitions. The first transition from the ambient quartz-like structure of GeO_2 to a higher pressure polymorph seems to occur at 19(5) GPa, at which the onset of Bragg reflections within the XRD pattern of the rutile structure can be observed (Fig. 3.18). This is in accordance to literature, in which a rutile structure in this pressure regime on the respective Hugoniot is expected [164]. However, even though the obtained XRD pattern is close to the shock breakout (t_{probe} = -0.5 ns relative to the shock breakout), the rutile peaks are low in intensity compared to the ambient GeO_2 Bragg reflections. The reason for the indistinct rutile peaks may be due to the experimental setup. Since a slurry of GeO_2 powder was used, it is possible, that the various orientations of the GeO_2 crystals within the slurry are slightly distorted and pressure propagation within a slurry might not be as efficient and effective as for single crystal shock compression, because the used epoxy in the slurry likely attenuates the shock wave. This would also explain why some ambient GeO_2 peaks can still be observed at this pressure, close to the shock breakout. This indicates, that the sample was incompletely compressed at 19(5) GPa.
At higher applied laser intensities and a concomitantly increased peak pressure of 53(9) GPa, one can observe the transformation from ambient GeO_2 towards an amorphous structure close to the shock breakout (t_{probe} = -1.0 ns relative to the shock breakout) (Fig. 3.18). Here it seems that the GeO_2 slurry has transited towards melting, which is in accordance to theoretical calculations [164]. Shortly after the shock breakout on the release (t_{probe} = 0.5 ns relative to the shock breakout), the characteristic (110) rutile-structure Bragg reflection appears next to the amorphous feature. This is an indication, that the GeO_2 release Hugoniot traverses P-T conditions at which the SiO_2 rutile structure is stable, which would explain the observed feature within the XRD data.
At 104(12) GPa, the ambient GeO_2 Bragg reflections almost completely vanish close to the shock breakout and an amorphous structure emerges. This amorphous structure could result from the melting of the GeO_2 slurry. Similar to fused silica (Fig. 3.25), one ob-

serves a shift of the amorphous peak position towards lower 2θ angles at later time delays, on the respective release Hugoniot. This indicates that the release Hugoniot of GeO_2 at these pressures does not traverse the solidus regime, similar to what has been seen for fused silica [101]. Future research might probe on the release Hugoniot of GeO_2 at later time delays, which could exhibit a recrystallization of ambient GeO_2 at lower temperatures and ambient pressures.

The calculated structure factors are in accordance to static data [49] at comparable pressures (e.g. Fig. 3.19). Due to the lower photon energies available from XFEL sources compared to synchrotron radiation sources, a limitation in F(r) (eq. 3.22) is apparent, which arises from the experimental finite maximum Q_{max}. This can result in extraneous features near the first coordination peak in F(r) which will be evident in the radial distribution function. However, the quality of g(r) is in reasonable agreement to static data and the peak shapes and positions in g(r) are changing significantly at higher pressures. The Ge-O distances, obtained from the first peak of g(r) are slightly lower compared to data from [49] and [165]. However, similar to static compression, an observed shift of the Ge-O distance towards larger values with increasing pressure up to 19 GPa indicates a phase transformation from a 4-fold to a 6-fold coordination, hence from the quartz-like GeO_2 structure to the rutile structure. With further compression, the effect of the pressure is apparent and the Ge-O distance is increasing again.

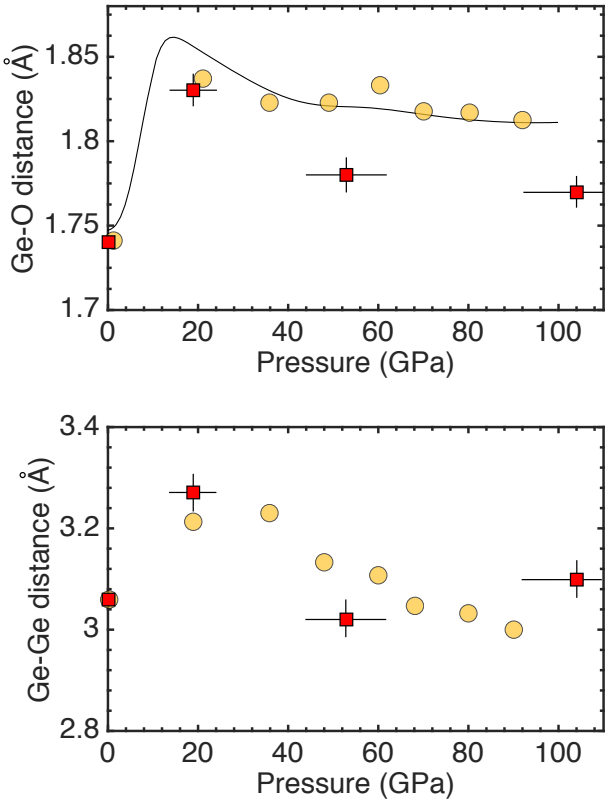

Figure 4.5: Ge-O (a) and Ge-Ge (b) distances derived from the first- and second peak position of g(r) with regard to pressure from this work (red squares) compared to Ge-O and Ge-Ge distances of amorphous GeO_2 glass at ambient temperatures from Ref. [165] (black line) and Ref. [49] (yellow circles)

A major difference between the results of shock compression from this work to static data

is the missing of the distinct shoulder at the lower ”r” side of the second peak, which has been widely observed in static data for pressures below 50 GPa [49, 165, 166, 167, 168]. The shoulder is associated to two Ge-Ge distances in the sixfold-coordinated GeO_2 structure. However, in this study, this feature cannot be distinguished from the broad second peak in g(r) at pressures below 53 GPa, likely because of the limited Q-range in the experiments. The pair correlation function at pressures of 53(9) GPa and 104(12) GPa are however in accordance to literature data [49, 165]. A coordination number of 4.0 at ambient state, of 5.8 at 19(5) GPa and 5.8 at 53(9) GPa is in good agreement with Ref. [165] but deviates from data of Ref. [49]. At 104(12) GPa, a coordination number of 6.9 indicates a higher coordinated GeO_2 structure.

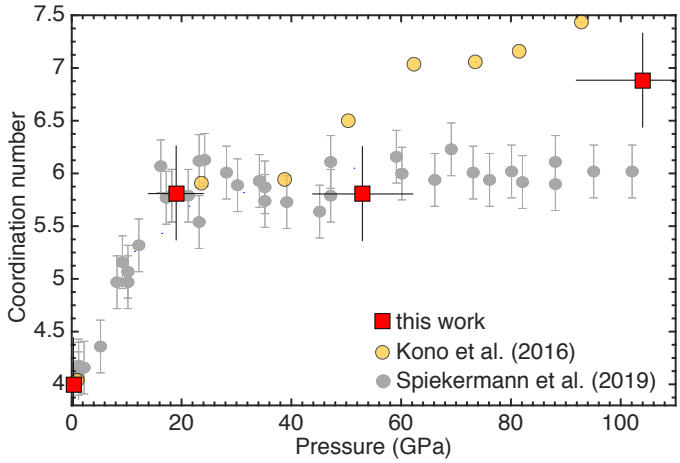

Figure 4.6: Germanium coordination number in shock compressed GeO_2 compared to literature data [49, 165].

4.1.4 Shock induced melting and recrystallization of α-quartz, α-cristobalite and fused silica

The results of the laser induced post-shock dynamic experiments on α-quartz, α-cristobalite and fused silica display distinct features, while being probed with the XFEL at late time delays on the respective release Hugoniot. The single crystal α-quartz structure undergoes two major stages during shock at pressures at liquidus conditions. In the first stage, melting is observed upon shock loading of the ambient structure. One can assume the structure is molten, because no crystalline features are observed within the X-ray diffraction data and only broad features are apparent. These broad XRD band(s) are similar to melt- and glass features seen for other materials, such as fused silica glass [169] or liquid tin [170]. In the results from the LCLS experiments, only one broad peak was detected, whereas in SACLA data, two broad plateaus are apparent (Fig. 3.22). Furthermore, the broad peak in the experimental data from LCLS is located at higher 2θ values than in the data from the SACLA experimental campaign, which likely derives from the

different peak pressures and temperatures in each experiment.
In the second stage, after 80 ns first Bragg reflections appear within the XRD of polycrystalline α-quartz at the LCLS experiments. Because the sample was only probed at a 80 ns delay time and not earlier, one cannot rule out the emergence of Bragg reflections at earlier times, as seen for instance at SACLA (30 ns time delay). The intensity of the Bragg reflections of polycrystalline quartz are generally increasing with later time delays, which suggests an increase of reflective α-quartz crystals within the melt.
Similar stages can be seen for α-cristobalite. Here the initial ambient polycrystalline structure, as seen in the XRD, transforms to a melt or melt-like structure, with no crystalline signatures apparent. It is not clear, however, if this structure results from shock amorphisation of the cristobalite bonds [171] or indeed represents a melt. Because of the emergence of Bragg reflections of polycrystalline α-cristobalite at late time delays, indicates a recrystallization from a melt, rather than the unlikely elastic re-bonding from an amorphous structure. Furthermore, amorphisation appears to be present at much lower pressures than achieved in the experiments and pressures within the sample likely correspond to the liquidus regime of the cristobalite Hugoniot [158].

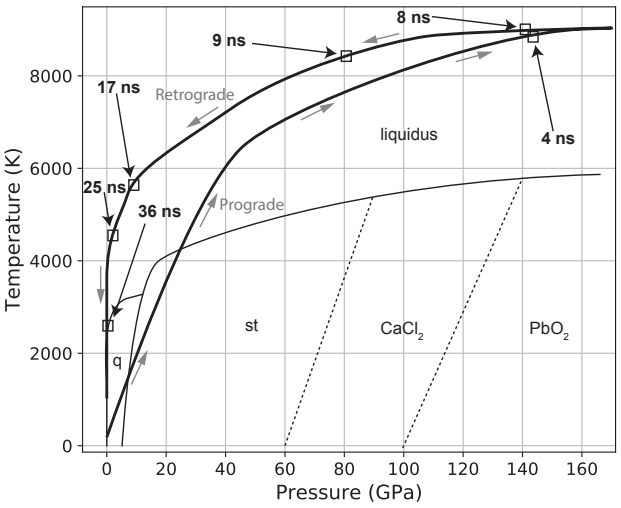

Figure 4.7: Results of the hydrodynamic simulations on shock compressed quartz up to 160 GPa and ~9000 K. Shown is the shock hysteresis with successive points of time after shock impact. As a reference, the phase diagram of SiO_2 is given with various polymorphs (q=quartz, st=stishovite, $CaCl_2$ and PbO_2 type silica).

Fused silica exhibits slightly different shock melt and release stages. From an initial amorphous glass structure, as seen in the XRD, one can observe the occurrence of a broad Bragg peak, similar to quartz, which can be associated to the melting of fused silica. This broad peak shifts towards lower 2θ values at later time delays, which indicates a pressure release of the sample. At late time delays (50 ns to 250 ns) the re-appearance of an amorphous structure with no crystalline features was detected. It is striking, that the product of molten single- as well as polycrystalline samples appear to be again of polycrystalline nature, whereas the shock melt product of an initial amorphous structure will remain amorphous on the release. A theoretical study indicated, that α-quartz will remain amorphous when shock loaded towards the liquidus regime and then released to ambient pressures [107]. However, it was argued, that the amorphous nature on the release is only

apparent at high temperatures and significant phase changes are likely happening during or after cooling over a period of time, much longer than the shock loading and unloading duration [107]. Since the time delays of the XFEL probing of the molten samples are relatively long, it is likely that the amorphous state of each sample has not been captured and temperatures have already cooled down. From hydrodynamic simulations (Fig. 4.7) it is evident, that for the simulated silica experiments at estimated peak pressures, the pressure is decreasing much faster than the temperature on the release, which is in accordance to the findings of this work, since first Bragg reflections of polycrystalline α-quartz emerged at a ∼30 ns time delay. At this time delay, temperature likely has reached the solidus regime of α-quartz at ambient pressure (Fig. 4.7).
To quantify the crystal growth kinetics, the grain size and growth of the release products during shock compression were determined, using the Scherrer equation (eq. 2.1). The calculated grain sizes gave rise to a grain growth for α-quartz of ∼80 Å within 200 ns (Fig. 4.8). The grain growth of α-cristobalite reaches ∼20 Å at 80 ns time delay (Fig.

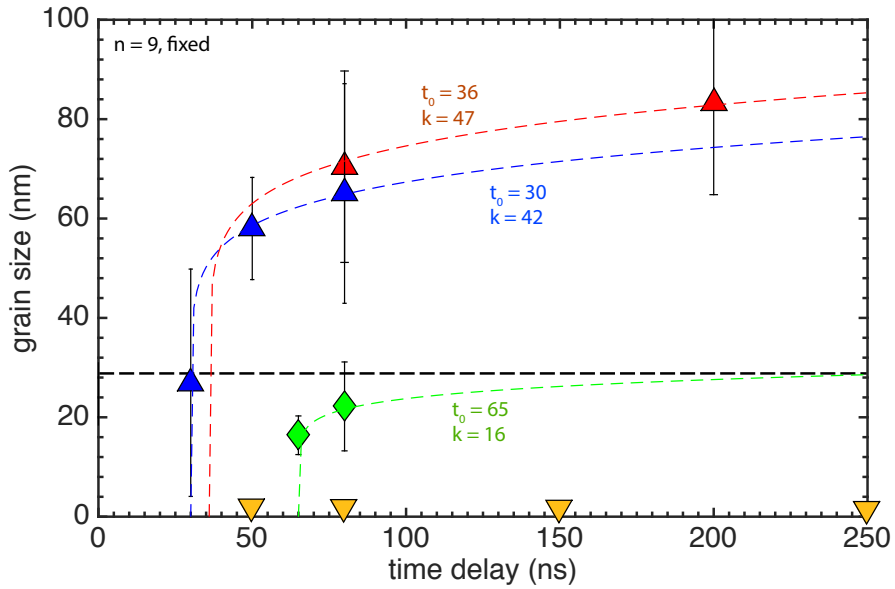

Figure 4.8: Experimentally determined average grain sizes as a function of delay time. Shown are results from the release kinetics of α-quartz (blue triangles at BL3:EH5, red triangles at MEC), α-cristobalite (green diamonds) and fused silica (yellow triangles). Given are further the fits from the simple growth model at a fixed n. The black dotted line indicates the initial grain size of the polycrystalline α-cristobalite.

4.8). No measurements at later time delays were conducted, and it is not clear, if grain growth continues at later time delays. However, similar to other nanocrystalline growth [172] the evolution of the mean particle size versus time resembles the trend predicted by classical growth models [173], in which the size of the particles D is proportional to growth time t, according to [174]:

$$D - D_0 = k(t - t_0)^{1/n} \tag{4.1}$$

where k(T) is the temperature-dependent material constant corresponding to exponent n, D_0 is the starting size and t_0 is the starting nucleation time. n can be associated to the transformation and growth mechanism [174, 175, 176]. Here, crystal growth is diffusion related if $n \leq 4$ or described by attachment or coalescence events if $n > 4$.
From hydrocode simulations, it is possible to determine the approximate time delay ($= t_0$), at which the P-T conditions would reach the solidus of α-quartz, α-cristobalite and fused silica, respectively (Fig. 4.7). For cristobalite, initial grain size of the polycrystalline structure was calculated from the ambient drives (28 nm), which was assumed to be also the final grain size after a complete recrystallization from the melt (Fig. 4.8, dashed black line). If fitted with a single best-fit value of n = 9 for all given crystal growths, one can assume a strong coalescence grain growth from the melt to be most appropriate. The strong coalescence grain growth as well as the absence of any crystal growth from fused silica at any given time delay indicates that crystallization and nucleation must arise from remaining short-range structures within the melt. Short-range bonding was also determined by DFT-MD simulations, in which the α-quartz structure was simulated at 9000 K and a pressure of 160 GPa. The resulting structure still exhibits some remaining Si-O bonding (Fig. 4.9a). By simulating X-ray diffraction of this bonded melt structure, one can observe a strong resemblance of the simulated- and the experimental diffraction pattern of molten quartz (Fig. 4.9b) which may be attributable to the growing structural disorder caused by bond breaking in the melt.

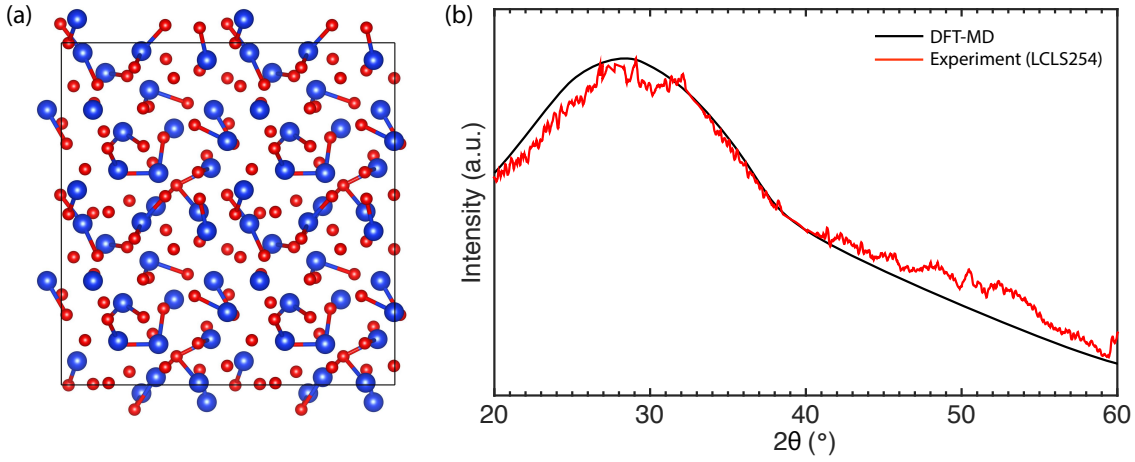

Figure 4.9: (a) Snapshot of the DFT-MD simulations of α-quartz at 160 GPa and 9000 K. Partial bonds within the liquid like structure are still apparent. (b) Diffuse liquid scattering signal from the experimental work at MEC and simulated from DFT-MD of the liquid α-quartz structure.

4.2 The effect of fast compression and temperature on phase transitions

4.2.1 Laser induced shock compression

From the experimental campaign on shock compressed **α-quartz**, a phase transformation towards the metastable *d*-NiAs structure was observed at 73 GPa, which are at higher P-T conditions than required for steady state SiO_2 equilibrium melting [58, 161, 162, 163]. A possible explanation for this discrepancy might be, that upon shock compression, pressure and temperature are raised simultaneously on ultra short time scales. The rise time of a shock wave is approximately 1 ns and temperature increases at about $\sim 10^3$ K, which results in a heating rate of $\sim 10^{12}$ K/s [107]. Solids can therefore be heated at rates higher than those required for a rearrangement of atoms upon melting [55]. The fast heating rate during this so-called "superheating" of the structure is likely an explanation for the metastable nature in the high P-T regime of the α-quartz Hugoniot. One can assume a shear-mediated crystallization of stishovite in which the oxygen sublattice responds readily to the loading of the applied shock and transforms to a quasi hexagonal closed packed (hcp) structure, accompanied by a partial diffusion and reordering of the Si cations. By increasing temperatures, the crystalline part of the sample successively transforms to a disordered network of atoms in which the smaller Si cations are randomly occupying one half of the octahedral sites. Prior to the sudden catastrophic homogenous melting at ∼115 GPa [107, 158], this structure is metastable, which is because of the short timescales during shock loading. Experiments in which only the temperature was monitored, revealed superheating of α-quartz at pressures between ∼70 GPa and ∼115 GPa [144, 150, 177]. This was consolidated by theoretical calculations [107, 158], but could not be verified on the lattice level, because of the limited diagnostics at that time.

For shocked compressed **stishovite** there was no phase transformation at a pressure of up to 336 GPa, which deviates strongly from structural modification in static compression experiments at respective pressures. This is in accordance with previous shock compression studies on stishovite [63, 133, 135]. It is assumed, that in absence the phase transformations, shock temperatures rise with increasing pressure to adjust to the increase of internal energy due to the compression work [63]. The calculations in this work indicate, that stishovite is experiencing temperatures ranging from 324 K up to 4757 K over a pressure range of 18 GPa to 336 GPa during shock loading (Fig. 4.4). However, because of the nanosecond timescales during dynamic loading and accommodation of rate-limiting kinetic hinderances, effects can result in significant shifts of equilibrium phase boundaries. Hence, transitions may not be observed or may require significant overpressure.

The delay or absence of a phase transition during shock loading, which have previously been determined by static data, is a known phenomenon for other shock compressed ma-

terials [105, 178, 179, 180, 181, 182]. The extent, however, to which these pressure induced phase transformations can be hindered seems to be much more pronounced for α-quartz and stishovite than for other materials such as Sn or Bi [105, 106]. The results are unexpected as one would not presume crystallization to be inhibited, at least e.g. for the $CaCl_2$ structure, which is differentiated from stishovite only by a small diffusionless displacement of oxygen ions.

4.2.2 Dynamic compression with the (RH)dDAC

A comparative summary of the dDAC study from this work of the structural response of α-cristobalite with regard to the compression rate is shown in Figure 4.10. Here, the pressure onset of phase transformations towards the high pressure polymorphs is increasing with increasing compression rates. Out of all the experimental runs, only the pressure onset of the phase transformation of α-cristobalite towards cristobalite II does not exhibit a clear correlation between compression rate and phase transformation. The uncertainty of the pressure determination from the Au standard is however at $\sim$0.5 GPa and is therefore comparable to the pressure range of the α-cristobalite $\rightarrow$ cristobalite II transition itself. From Figure 4.10 it is evident, that the compression rate has a fundamental effect on phase transformations. It has been shown, that an overpressurization of α-cristobalite can lead to the delay of phase transformation towards cristobalite II [46, 47], however, no quantification of this effect was made before. Because of the novelty of the dDAC technique, there are only a few other experimental campaigns, which elucidate the effect of compression rate towards pressure onset of phase transitions for geological materials [88, 89, 90, 183]. The effect of a delayed phase transition by fast compression was observed in a dDAC study with α-quartz as the starting material [88]. Here, the high pressure phase transition towards stishovite (and an amorphous feature) was seen between 18-38 GPa, which is in contrast to the pressure of $\sim$7 GPa reported in static transformation experiments. The effect of fast compression rate to over-pressurization was also found in a study on KCl [183]. It was shown, that the compression rate is dependent on the activation energy, with the activation energies decreasing linearly with the logarithm of the compression rate.
In static experiments, it was shown, that at small over-pressurization of a DAC, the nuclei of high pressure phases can be formed on grain boundaries, whereas at large overpressurization nuclei form in the grain interiors. That means, that the nucleation mechanism changes from a heterogeneous, to a homogeneous nucleation with increasing overpressurization. The formation of nuclei near the grain boundaries and surfaces has therefore a slightly smaller activation energy at low compression rates. However, with increasing compression rates, the effective activation energy for homogeneous nucleation decreases, which results in the increasing likelihood of a nucleation in the grain interiors and subsequent suppression of heterogeneous nucleation. This can be observed from the

diffraction images of the seifertite formation at increasing compression rates at which slower compression resulted in larger and more inhomogeneous diffraction spots and rings, while more rapid compression led to more homogeneous diffraction rings. One can therefore assume, that the higher compression rates seen in this work are the result of the effective increase in the slower homogeneous nucleation, resulting in the over-pressurization and delay of phase transitions to higher transition pressures.

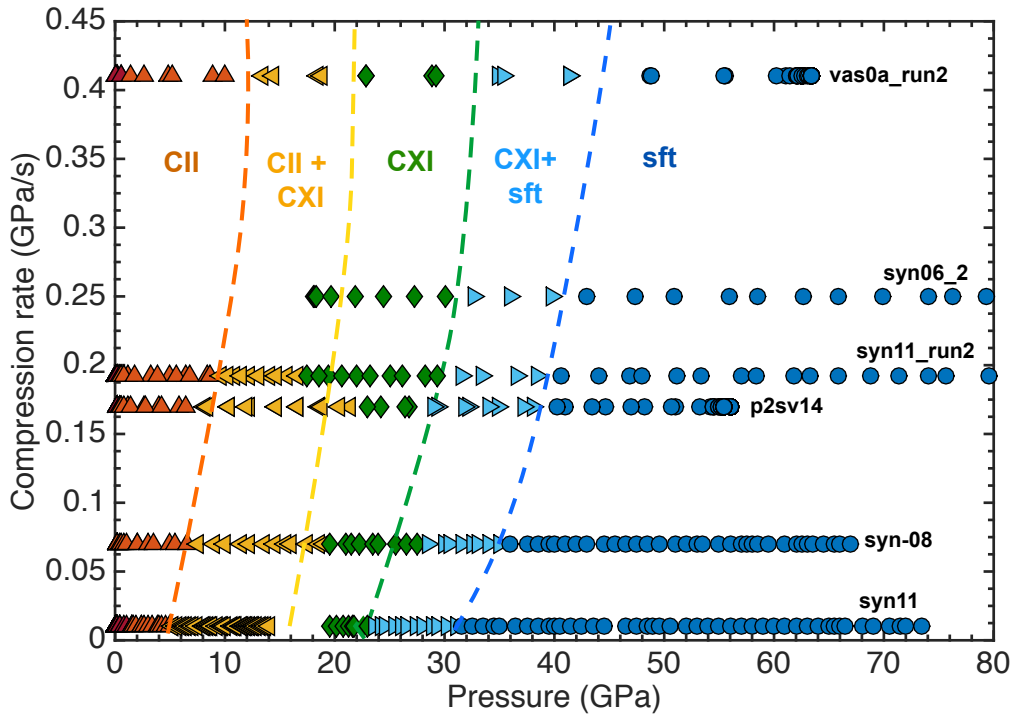

Figure 4.10: Pressure versus compression rate for different experimental runs with the dDAC and powder as starting material. Shown are the different high pressure polymorphs of α-cristobalite: cristobalite II (CII), cristobalite X-I (CXI) and seifertite (Sft).

Subsequently, the effect of temperature on the phase transition of α-cristobalite during fast compression was investigated. At static conditions, it was shown, that elevated temperatures will promote seifertite formation at pressures as low as ∼11 GPa due to its low activation energy (∼10 kJ/mol). This is consistent with a diffusionless transformation mechanism from α-cristobalite to seifertite [42]. At even higher temperatures a possible diffusion controlled mechanism can promote formation of stishovite, which occurs with a relatively large activation energy (∼110 kJ/mol) [184]. Since the formation of stishovite was not encountered in this study, the applied temperatures were apparently not sufficient to promote the phase transformation. The first seifertite Bragg reflections in this work with the RHdDAC were observed at 24 GPa. At this pressure, temperatures exceeding ∼825 °C would have likely promoted stishovite formation [184], however temperatures applied in this work were only at a maximum of 700 °C. Furthermore, during the fast ramp compression, the molecular volumes are strongly deviating from static and dynamic

compression data at comparable compression rates. This indicates, that the molecular volume of seifertite at temperatures between 500 °C and 700 °C cannot reach equilibrium- or low compression rate steady state values because of the thermal expansion within its lattice structure during fast compression.

4.3 The effect of hydrostaticity on structural transformation pathways

4.3.1 Stishovite

There has been evidence derived from this work, that shock compressed stishovite remains stable up to a pressure of 336 GPa. Besides the effect of short-timescales, this can be explained by uniaxial compression during shock loading. Strong anisotropic effects are in place while the shock wave traverses the sample, which is reflected in the differences of relative compression between the lattice parameters *a* and *c* of shock compressed stishovite (Fig. 4.11). The relative lattice parameter displays a preferred compression along the *a* axis up to ∼100 GPa. At pressures between 100 GPa and 336 GPa,

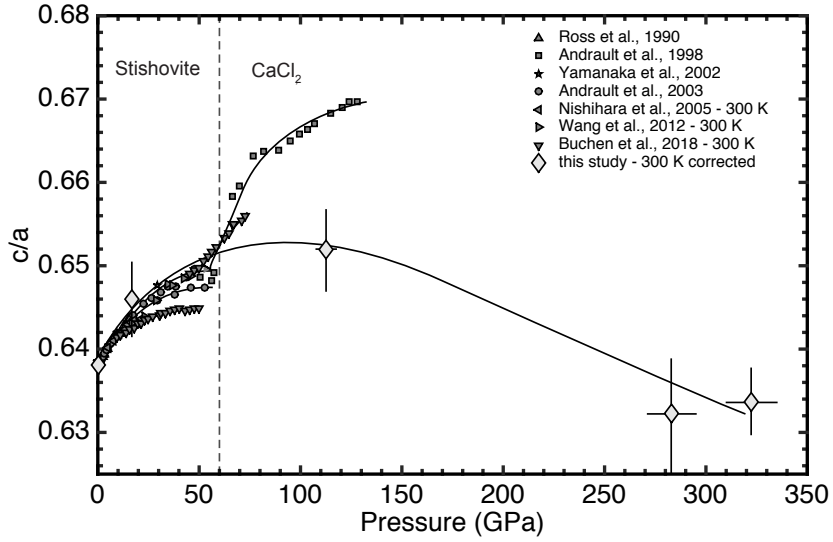

Figure 4.11: Lattice parameter ratio *c*/*a* with regard to pressure. Indicated is furthermore the pressure, at which a structural transformation from stishovite to $CaCl_2$-type silica has been observed in static experiments [20, 38] (dashed line).

the pressure axis of stishovite orientates itself primarily along the *c*-direction, indicating strong non-hydrostatic conditions. Additionally, the broadening of the Bragg reflections in Figure 3.11 likely arises from a pressure gradient and non-hydrostatic stress, with the accuracy of the measured d-values being diminished. Previous studies on stishovite in static experiments show, that non-hydrostaticity produces large deviatoric stresses as a

result of the high shear strength [22, 24] and it was reported that the preferred orientation of stishovite under compression was the crystallographic *c*-direction [185]. It is well known from static experiments, that the effect of hydrostaticity can fundamentally change the onset, or presence, of phase transitions [46, 186]. However, it was suggested, that non-hydrostatic conditions in DACs, for instance, actually decrease the pressure-induced onset of e.g. a ferroelastic phase transition from the tetragonal (stishovite) to the orthorhombic ($CaCl_2$) structure [23]. Since no such transition was observed in this work, the non-hydrostatic stresses may displace the equilibrium boundaries to higher pressures in shock compression experiments, as previously suggested [107, 187].

The anisotropic behavior of shock compressed stishovite was further confirmed by variable cell DFT-MD simulations. These showed, that by hydrostically compressing the stishovite unit cell the expected phase transition of the stishovite structure to the $CaCl_2$ structure took place (Fig. 3.16). Here, the transition is driven by the softening of a zone-center optic mode that couples with acoustic modes to produce a marked softening of the shear elastic constants [18]. In contrast, when applying uniaxial stress conditions to the stishovite unit cell, only slightly distorted oxygen atoms are observed and the general stishovite structure is retained (Fig. 3.16). These observations endorse the anisotropic compression behavior of stishovite during laser induced shock compression and might be, next to the short timescales of the experiment, an explanation, why a phase transition of stishovite to $CaCl_2$ cannot be observed at pressures of up to 336 GPa.

4.3.2 α-Cristobalite

The effect of hydrostaticity during dynamic compression was furthermore investigated with the dDAC, and it is evident that the mechanism that α-cristobalite adopts during compression depends on the stress conditions. In contrast to non-hydrostatic conditions, that is without any pressure transmitting medium (PTM) using powders as starting material, this work also reports on hydrostatic experiments with single crystal α-cristobalite and Ne as the PTM. In non-hydrostatic experiments with powders, the α-cristobalite $\rightarrow$ cristobalite II $\rightarrow$ cristobalite X-I $\rightarrow$ seifertite phase transition sequence takes place. Here, grain interaction within the powder samples are the major contributor to a non-hydrostatic environment. For single crystal α-cristobalite in a hydrostatic environment only a phase transformation to the cristobalite X-I structure was detected between 14 GPa and 82 GPa. No intermediate phase transitions or higher pressure phases, such as seifertite were encountered, neither during compression nor decompression. The results are in great accordance with recent data from a steady state Raman study [46], in which cristobalite X-I was shown to be stable up to $\sim$80 GPa under hydrostatic conditions. Furthermore,

this work demonstrates, that in hydrostatic experiments, seifertite formation cannot be induced by e.g. an overdriving of the hydrostastic conditions through fast compression rates (0.07-0.41 GPa/s). This might be different at even higher compression rates and should be further investigated in the future.

The dependence of phase transitions of α-cristobalite at high pressures to hydrostaticity was investigated by means of metadynamics DFT-MD simulations. Here, variable cell conditions (hydrostatic and non-hydrostatic) and *ab initio* calculations were applied. From the result of the simulations one can observe various phase transformations towards high pressure structures, strongly depending on the simulation modes. Both, the *ab initio* and vc-md simulations show a similar transformation pathway up to $\sim$20 GPa, in which a phase transition of α-cristobalite to a high pressure structure (hp-cristobalite) was shown. The hp-cristobalite structure is identical to cristobalite X-I and the transition pressure of the simulations is consistent with experimental findings, in which the transformation towards the cristobalite X-I phase was observed. The difference in density (Fig. 3.35) of the two simulated approaches can be attributed to the fact that the *ab initio* simulations are carried out at zero Kelvin compared to the vc-md calculations at finite temperatures. On further compression by means of *ab initio*, this structure transforms into six-fold coordinated stishovite at $\sim$37 GPa, which is in agreement to MD simulations [188]. This is, however, in stark contrast to experimental findings, in which the stishovite structure was not observed during compression with the dDAC, neither for single crystals (hydrostatic) nor powder starting materials (non-hydrostatic). When metadynamics are switched on and α-cristobalite is uniaxial compressed in the vc-md runs, a phase transformation from hp-cristobalite towards the seifertite structure at $\sim$28 GPa takes place. This is consistent with experimental results from this work and literature data [28, 31, 44, 45, 189] in a non-hydrostatic environment, in which a transformation of cristoablite X-I to seifertite was demonstrated between 23 GPa and 28 GPa. By hydrostatically compressing α-cristobalite with the use of variable cell DFT-MD one does not observe any further phase transformations from hp-cristobalite to a higher pressure phase. This is consolidating experimental results of this work and literature data [46], in which the cristobalite X-I structure was observed at pressures up to 82 GPa during hydrostatic compression (Fig. 3.33). In conclusion, the vc-md simulations match the experimental results of this work and the effect of hydrostaticity on the phase transitions was successfully demonstrated.

4.4 Conclusions and geophysical implications

4.4.1 The transformation pathways of silica and GeO_2 at high pressure conditions

In summary, this work investigated four different silica polymorphs, α-quartz, fused silica, stishovite and α-cristobalite, as well as the structural analogue GeO_2 by means of laser induced shock compression and the concomitant use of XFEL radiation.
Furthermore, the dynamic behavior of α-cristobalite at high pressures and variable compression rates were studied with the use of the (resistive heated) dynamic DAC and synchrotron radiation.
On the basis of the obtained results, phase transformation pathways of silica at high pressures in relation to compression techniques were constructed (Fig. 4.13). Finally, these results are incorporated into the current understanding of silica phase relations.

A phase transformation from shock compressed **α-quartz** to the stishovite (rutile) structure at 45 GPa and a transition between 73 GPa and 94 GPa to the defective niccolite (*d*-NiAs) structure was observed in this work. The occurrence of stishovite on the quartz Hugoniot was theoretically predicted [107] and verified in the experiments. Even though the timescales of shock loading are short, crystallization of stishovite was not hindered as previously suggested [151]. These findings are consistent with DFT-MD simulations on nanosecond nucleation and crystal growth of shock compressed SiO_2 [159]. The transition from quartz to the defective niccolite structure on the Hugoniot could be explained by elevated shock temperatures and fast heating rates, indicating a strong thermal dependence of the *d*-NiAs phase formation under disequilibrium conditions. The formation of stishovite at 45 GPa in this work is, however, in contrast to gas-gun experiments, where solely the *d*-NiAs structure was found [151]. The differences between gas-gun and laser induced shock compression experiments, which have been similarly encountered recently for fused silica [100, 153], might result from distinctions of the experimental techniques (e.g. timescales, shock planarity and shock temperatures) and should be investigated in the future.
From dDAC experiments, it was shown, that α-quartz undergoes a phase transition between ∼18-38 GPa to the rutile structure, with remains of α-quartz and amorphization signatures [88, 89]. Between ∼38-77 GPa, quartz ultimately transforms to the rutile structure and glass. The results from shock and dynamic compression deviate strongly from static equilibrium data, in which a phase transformation of α-quartz to coesite at ∼2-7 GPa [14, 15] to the rutile structure at ∼7-60 GPa [16, 17, 18] and to the $CaCl_2$ structure above 60 GPa was observed [31].

The transformation pathway of **fused silica** at high pressures was investigated by means of static and shock compression. In laser and gas-gun experiments it was demonstrated that fused silica transforms along its Hugoniot to the stishovite (rutile) structure at pressures of ∼5-34 GPa (laser shock) and ∼34-63 GPa (gas-gun) [100, 153]. Up to date it could not be shown, if an intermediate phase transition to e.g. the *d*-NiAs structure might occur at higher pressures, which has been seen for quartz in this work. However, we did observe the transformation of fused silica to the *d*-NiAs structure in one shock drive to ∼60 GPa (Fig. 4.12). Due to the statistical limitation we cannot conclusively identify this phase transition at this point. There are, although, indications from shock recovery experiments, that fused silica is transitioning to the *d*-NiAs structure at high pressures on the Hugoniot, because a very small amount of d-NiAs phase was identified together with glass within recovery material [190].

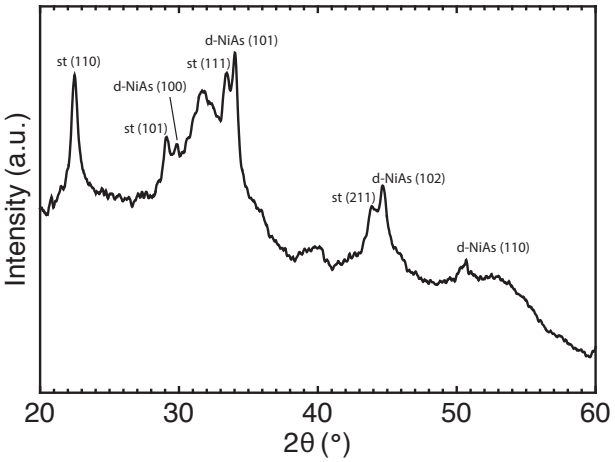

Figure 4.12: XRD outline of shock compressed fused silica. Here, a transformation towards the stishovite (st) and *d*-NiAs phase was observed.

In comparison to shock experiments, data from static compression exhibits a transition towards the rutile structure at ∼10 GPa and subsequently the *d*-NiAs structure has been demonstrated at pressures between 30-55 GPa (and 1000-1300 K) [31]. At pressure exceeding 55 GPa, the $CaCl_2$ structure was observed [21, 22, 23, 24, 25].

In this work, **α-cristobalite** was shock driven to a peak pressure of ∼70 GPa and a melting signature was obtained by means of X-ray diffraction. Shock induced melting of α-cristobalite along its Hugoniot at ∼70 GPa is in good agreement to theoretical calculations [191], in which liquidus conditions are achieved at pressures exceeding ∼65 GPa. One other study reports on the structural transformation of α-cristobalite on its Hugoniot. Here, the recovery experiment could demonstrate an amorphization of α-cristobalite at pressures between 23-28 GPa [171].
In comparison, the P-T conditions of the high pressure phase transitions of α-cristobalite with the use of the dDAC seems to be more complex and strongly depending on the compression rate and hydrostaticity of the experiment. It is evident from this study, that α-cristobalite transforms to cristobalite II at pressures between 0.5 and 1 GPa when using powder as the starting material. Further compression induced a phase transition towards the cristobalite X-I structure between 5-35 GPa and ultimately to seifertite between 23-35

GPa. By dynamically compressing single crystal α-cristobalite, one only observes a phase transition of α-cristobalite to cristobalite II at $\sim$1 GPa, and cristobalite II to cristobalite X-I at $\sim$14 GPa. It was demonstrated, that cristobalite X-I remains stable up to a pressure of 82 GPa and no further phase transition towards the seifertite structure was detected. This transformational pathway is similar to static experiments, in which a phase transition of α-cristobalite towards cristobalite II has been observed between 1.5-11 GPa, cristobalite II to cristobalite X-I at 11 GPa and cristobalite X-I to seifertite at $\sim$30 GPa [45, 46, 47]. Similar to the findings of this work, it becomes evident, that by using single crystal α-cristobalite as the starting material cristobalite X-I remains stable up to 80 GPa [46].

The structural behavior of **stishovite** at high pressures seems to be less complex, compared to other silica polymorphs. In this work we demonstrated, that the stishovite structure remains stable up to 336 GPa. This is in contrast to static compression experiments, in which a phase transformation to $CaCl_2$ at $\sim$60 GPa was observed [20, 38]. The shock compressed stable stishovite structure at 336 GPa implies a skipping of three different second-order equilibrium phase transitions to $CaCl_2$, α-PbO_2 and pyrite-type structures, illustrating how complex structural changes are hindered during dynamic compression experiments.

The lattice response of polycrystalline $\mathbf{GeO_2}$ was investigated by means of laser shock compression. From XRD it was shown, that GeO_2 undergoes a phase transition from a quartz-like structure to the rutile structure at 19 GPa and transforms to a melt at a pressure of 53 GPa. It was furthermore shown, that the bonding of Ge-O and Ge-Ge changes during shock loading towards high pressures, and is accompanied with an increase of the coordination number. A change in coordination from 4-fold at ambient conditions to 5.8-fold at 19 GPa indicates further a transition from a tetragonal quartz-like structure towards an octahedral rutile structure. Ultimately, a coordination number of 6.9 at 104 GPa implies a high-coordinated melt structure. Similar observations were made by using silica glass as starting material in a DAC experiment [169]. Here, a continuous increase in coordination from 4 to 6.8 at pressures of up to 172 GPa was observed.

Finally **shock induced melting** was investigated by using α-quartz, α-cristobalite and fused silica as starting materials. Here, it was shown, that melting occurs at peak pressures of at least 119 GPa for α-quartz, at 70 GPa for α-cristobalite and at 126 GPa for fused silica. It must be noted, that shock induced melting for these three silica polymorphs might also occur at lower pressures, but was not investigated in this work.

To summarize, it becomes evident from the results of this work and literature, that the

different phase transition pathways of silica are strongly dependent on the applied compression techniques and that the compression rate of an experiment has a vast influence on the pressure onset of a phase transition. One should be therefore cautious to compare results form dynamic compression experiments to the existing pressure and temperature conditions of silica phase relations obtained from static data.

4.4.2 Geophysical implications

Although the pressure and temperature range encompassed in Super-Earths (1-10 M_E) is comparable to conditions from this work (e.g. Fig. 4.4), one has to be careful to constrain the physical and chemical properties inside these planets from results of shock compressed materials. Within the mantle of terrestrial planets, high pressure mineral phase transitions are likely occurring on large timescales ($\sim$Mio years) and static conditions must be assumed. For instance, seismic discontinuities observed in the mid-lower mantle (1000-1600 km) are associated to the phase transition of the $CaCl_2$ structure, which was demonstrated in static compression experiments, but is in contrast to findings of this work and other dynamic compression experiments. It can therefore be assumed, that results from e.g. diamond anvil cell experiments are a more likely proxy for the compositional transitions within the interiors of terrestrial planets compared to dynamic compression by a laser or gas-gun experiment.
On the other hand, some natural phenomena are occurring on timescales, which are more comparable to conditions of a laser induced shock compression, gas-gun or dynamic DAC experiment. The timescales of an impact, for instance, are within the ns-s range, depending on the size of the impactor. In natural impact sites, small quantities of e.g. stishovite or the defective niccolite phase were found [192, 193] which strongly endorse the findings of this work on other dynamic compression experiments [100, 151, 153].
The dDAC experiments in this study furthermore demonstrated, that the compression rate has a vast influence on the phase transition onset pressure and, for at least α-cristobalite, it is evident that faster compression leads to a delay of the transition to a high-pressure phase. These findings are therefore very important to correctly understand the complex P-T conditions of e.g. an impact event. These conditions are often derived from minerals and crystal structures found in meteorites or impact debris. However, meteorites which descend from fast velocity impacts, and are thus experiencing fast compression conditions, might exhibit low-pressure mineral phases (such as α-cristobalite, cristobalite II or cristobalite X-I) while actually having experienced much higher pressures. The lack of a high pressure phase such as seifertite might then cause a misleading conclusion about the prevailing P-T conditions. Moreover, single crystal α-cristobalite might have experienced hydrostatic compression during the impact event. It will then not have transitioned to a high pressure phase (e.g. seifertite) which could easily lead to the misassumption of lower

pressure conditions during impact.

Finally, the crystal growth detected from shock-induced melting of α-quartz and α-cristobalite in this work, lead to the conclusion, that a strong coalescence growth is apparent on nanosecond timescales. The occurrence of crystalline α-quartz and α-cristobalite in highly shocked meteorites within a glass-like matrix [43] endorses the *in-situ* findings of nanocrystalline silicate growth from a shock induced melt in this study. Contrary to the recrystallization of the initially crystalline materials α-quartz and α-cristobalite from the melt, there were no recrystallization signatures from initially amorphous fused silica. This indicates a short-range bonding within the melt from α-quartz and α-cristobalite, which is consolidated by a simple growth model that results in coalescence grain growth. From published results of optical reflectivity measurements in a laser induced shock compression study, it was proposed that liquid silica undergoes a transition from a bonded melt to an atomic fluid, which causes the electrical and therefore thermal conductivities of silica to attain metallic like values [194]. We could demonstrate, that at P-T conditions of at least $\sim$160 GPa and $\sim$9000 K, silica is present as a bonded liquid and does not experience a complete dissociation of Si-O atoms. These experimental conditions are comparable to the Earth's deep interior and it can be deduced, that silica melts are not present as a conductive fluid and have no influence on the dynamo generation in the lower mantle or upper liquid core. This might be different for larger terrestrial planets, where P-T conditions are much higher and for which it can be assumed that liquid silica would contribute to magnetic fields in the deep interior [108].

Figure 4.13: Summary of the high pressure polymorphism of SiO_2 with regard to compression techniques and starting material. Shown are results from this work and literature of the structural transformation pressures of α-quartz, fused silica, α-cristobalite and stishovite as starting materials.

Bibliography

[1] A. Wolszczan and D. A. Frail, Nature **355**, 145 (1992).

[2] M. Damasso, A. Bonomo, N. Astudillo-Defru, X. Bonfils, L. Malavolta, A. Sozzetti, E. Lopez, L. Zeng, R. Haywood, J. Irwin, et al., Astronomy & Astrophysics **615**, A69 (2018).

[3] L. Zeng and D. Sasselov, Publications of the Astronomical Society of the Pacific **125**, 227 (2013).

[4] S. Seager, M. Kuchner, C. Hier-Majumder, and B. Militzer, The Astrophysical Journal **669**, 1279 (2007).

[5] D. Valencia, R. J. O'Connell, and D. Sasselov, Icarus **181**, 545 (2006).

[6] T. S. Duffy and R. F. Smith, Frontiers in Earth Science **7**, 23 (2019).

[7] W. J. Borucki, Reports on Progress in Physics **79**, 036901 (2016).

[8] T. Duffy, N. Madhusudhan, and K. Lee, Treatise on Geophysics **2** (2015).

[9] S. Seager, Science **340**, 577 (2013).

[10] A. R. Howe, A. Burrows, and W. Verne, The Astrophysical Journal **787**, 173 (2014).

[11] W. F. McDonough and S.-S. Sun, Chemical geology **120**, 223 (1995).

[12] F. Wagner, N. Tosi, F. Sohl, H. Rauer, and T. Spohn, Astronomy & Astrophysics **541**, A103 (2012).

[13] A. Putnis, *An introduction to mineral sciences* (Cambridge University Press, 1992).

[14] F. Boyd and J. England, Journal of Geophysical Research **65**, 749 (1960).

[15] M. Akaogi, H. Yusa, K. Shiraishi, and T. Suzuki, Journal of Geophysical Research: Solid Earth **100**, 22337 (1995).

[16] S. Stishov and S. Popova, Geokhimiya **10**, 923 (1961).

[17] V. Dmitriev, P. Toledano, V. Torgashev, and E. Salje, Physical Review B **58**, 11911 (1998).

[18] J. K. Wicks and T. S. Duffy, Deep earth: Physics and chemistry of the lower mantle and core **217**, 69 (2016).

[19] D. Andrault, G. Fiquet, F. Guyot, and M. Hanfland, Science **282**, 720 (1998).

[20] D. Andrault, R. J. Angel, J. L. Mosenfelder, and T. Le Bihan, American Mineralogist **88**, 301 (2003).

[21] R. E. Cohen, Geophysical Research Letters **14**, 37 (1987).

[22] Y. Tsuchida and T. Yagi, Nature **340**, 217 (1989).

[23] K. J. Kingma, R. E. Cohen, R. J. Hemley, and H.-k. Mao, Nature **374**, 243 (1995).

[24] R. Hemley, J. Shu, M. Carpenter, J. Hu, H. Mao, and K. Kingma, Solid State Communications **114**, 527 (2000).

[25] N. Sun, W. Shi, Z. Mao, C. Zhou, and V. B. Prakapenka, Journal of Geophysical Research: Solid Earth (2019).

[26] P. Dera, C. T. Prewitt, N. Z. Boctor, and R. J. Hemley, American Mineralogist **87**, 1018 (2002).

[27] M. Murakami, K. Hirose, S. Ono, and Y. Ohishi, Geophysical Research Letters **30**, 1207 (2003).

[28] L. Dubrovinsky, N. Dubrovinskaia, S. Saxena, F. Tutti, S. Rekhi, T. Le Bihan, G. Shen, and J. Hu, Chemical Physics Letters **333**, 264 (2001).

[29] A. B. Belonoshko, L. S. Dubrovinsky, and N. A. Dubrovinsky, American Mineralogist **81**, 785 (1996).

[30] B. Grocholski, S.-H. Shim, and V. Prakapenka, Journal of Geophysical Research: Solid Earth **118**, 4745 (2013).

[31] V. Prakapenka, G. Shen, L. Dubrovinsky, M. Rivers, and S. Sutton, Journal of Physics and Chemistry of Solids **65**, 1537 (2004).

[32] Y. Kuwayama, K. Hirose, N. Sata, and Y. Ohishi, Science **309**, 923 (2005).

[33] N. L. Ross, J. Shu, and R. M. Hazen, American Mineralogist **75**, 739 (1990).

[34] T. Yamanaka, T. Fukuda, and J. Mimaki, Physics and Chemistry of Minerals **29**, 633 (2002).

[35] W. R. Panero, L. R. Benedetti, and R. Jeanloz, Journal of Geophysical Research: Solid Earth **108**, ECV (2003).

[36] Y. Nishihara, K. Nakayama, E. Takahashi, T. Iguchi, and K.-ì. Funakoshi, Physics and Chemistry of Minerals **31**, 660 (2005).

[37] F. Wang, Y. Tange, T. Irifune, and K.-i. Funakoshi, Journal of Geophysical Research: Solid Earth **117** (2012).

[38] J. Buchen, H. Marquardt, K. Schulze, S. Speziale, T. Boffa Ballaran, N. Nishiyama, and M. Hanfland, Journal of Geophysical Research: Solid Earth **123**, 7347 (2018).

[39] I. Weber, A. Greshake, and A. Bischoff, LPI p. 1342 (2000).

[40] A. El Goresy, P. Dera, T. G. Sharp, C. T. Prewitt, M. Chen, L. Dubrovinsky, B. Wopenka, N. Z. Boctor, and R. J. Hemley, European Journal of Mineralogy **20**, 523 (2008).

[41] M. Miyahara, S. Kaneko, E. Ohtani, T. Sakai, T. Nagase, M. Kayama, H. Nishido, and N. Hirao, Nature communications **4**, 1 (2013).

[42] U. W. Bläß, Physics and Chemistry of Minerals **40**, 425 (2013).

[43] H. Leroux and P. Cordier, Meteoritics & Planetary Science **41**, 913 (2006).

[44] V. Prokopenko, L. Dubrovinsky, V. Dmitriev, and H.-P. Weber, Journal of alloys and compounds **327**, 87 (2001).

[45] N. A. Dubrovinskaia, L. S. Dubrovinsky, S. K. Saxena, F. Tutti, S. Rekhi, and T. Le Bihan, European Journal of Mineralogy **13**, 479 (2001).

[46] A. Černok, K. Marquardt, R. Caracas, E. Bykova, G. Habler, H.-P. Liermann, M. Hanfland, M. Mezouar, E. Bobocioiu, and L. Dubrovinsky, Nature communications **8**, 1 (2017).

[47] P. Dera, J. D. Lazarz, V. B. Prakapenka, M. Barkley, and R. T. Downs, Physics and Chemistry of Minerals **38**, 517 (2011).

[48] J. Haines, J. Leger, C. Chateau, and A. Pereira, Physics and Chemistry of Minerals **27**, 575 (2000).

[49] Y. Kono, C. Kenney-Benson, D. Ikuta, Y. Shibazaki, Y. Wang, and G. Shen, Proceedings of the National Academy of Sciences **113**, 3436 (2016).

[50] J. Haines, J. Leger, and C. Chateau, Physical Review B **61**, 8701 (2000).

[51] A. R. Oganov, R. J. Hemley, R. M. Hazen, and A. P. Jones, Reviews in Mineralogy and Geochemistry **75**, 47 (2013).

[52] L. Verlet, Physical review **159**, 98 (1967).

[53] D. M. Teter, R. J. Hemley, G. Kresse, and J. Hafner, Physical Review Letters **80**, 2145 (1998).

[54] S.-N. Luo, T. J. Ahrens, T. Çağın, A. Strachan, W. A. Goddard III, and D. C. Swift, Physical Review B **68**, 134206 (2003).

[55] S.-N. Luo and T. J. Ahrens, Physics of the Earth and Planetary Interiors **143**, 369 (2004).

[56] H. Niu, P. M. Piaggi, M. Invernizzi, and M. Parrinello, Proceedings of the National Academy of Sciences **115**, 5348 (2018).

[57] V. V. Le and G. T. Nguyen, Journal of Non-Crystalline Solids **505**, 225 (2019).

[58] S.-N. Luo, T. Çağin, A. Strachan, W. A. Goddard III, and T. J. Ahrens, Earth and Planetary Science Letters **202**, 147 (2002).

[59] Y. Usui and T. Tsuchiya, Journal of Earth Science **21**, 801 (2010).

[60] R. Martoňák, D. Donadio, A. R. Oganov, and M. Parrinello, Physical Review B **76**, 014120 (2007).

[61] F. González-Cataldo, S. Davis, and G. Gutiérrez, **720**, 012032 (2016).

[62] D. C. Swift, J. Eggert, D. G. Hicks, S. Hamel, K. Caspersen, E. Schwegler, G. W. Collins, N. Nettelmann, and G. Ackland, The Astrophysical Journal **744**, 59 (2011).

[63] M. Millot, N. Dubrovinskaia, A. Černok, S. Blaha, L. Dubrovinsky, D. Braun, P. Celliers, G. Collins, J. Eggert, and R. Jeanloz, Science **347**, 418 (2015).

[64] P. Bridgman, Physical Review **48**, 893 (1935).

[65] C. Weir, E. Lippincott, A. Van Valkenburg, and E. Bunting, Journal of Research of the National Bureau of Standards. Section A, Physics and Chemistry **63**, 55 (1959).

[66] A. Van Valkenburg, Review of Scientific Instruments **33**, 1462 (1962).

[67] W. A. Bassett, High Pressure Research **29**, 163 (2009).

[68] A. Dewaele, P. Loubeyre, F. Occelli, O. Marie, and M. Mezouar, Nature communications **9**, 1 (2018).

[69] Z. Jenei, E. O'Bannon, S. Weir, H. Cynn, M. Lipp, and W. Evans, Nature communications **9**, 1 (2018).

[70] N. Dubrovinskaia, L. Dubrovinsky, N. A. Solopova, A. Abakumov, S. Turner, M. Hanfland, E. Bykova, M. Bykov, C. Prescher, V. B. Prakapenka, et al., Science advances **2**, 1600341 (2016).

[71] W. J. Evans, C.-S. Yoo, G. W. Lee, H. Cynn, M. J. Lipp, and K. Visbeck, Review of Scientific Instruments **78**, 073904 (2007).

[72] Z. Jenei, H. Liermann, R. Husband, A. Méndez, D. Pennicard, H. Marquardt, E. O'Bannon, A. Pakhomova, Z. Konopkova, K. Glazyrin, et al., Review of Scientific Instruments **90**, 065114 (2019).

[73] R. Smith, J. Eggert, R. Jeanloz, T. Duffy, D. Braun, J. Patterson, R. Rudd, J. Biener, A. Lazicki, A. Hamza, et al., Nature **511**, 330 (2014).

[74] R. Trainor, J. Shaner, J. Auerbach, and N. Holmes, Physical Review Letters **42**, 1154 (1979).

[75] P. Celliers, G. Collins, L. Da Silva, D. Gold, and R. Cauble, Applied Physics Letters **73**, 1320 (1998).

[76] A. L. Robinson, Synchrotron Radiation News **28**, 4 (2015).

[77] D. W. Kerst and R. Serber, Physical Review **60**, 53 (1941).

[78] Y. Akahama and H. Kawamura, High Pressure Research **27**, 473 (2007).

[79] L. Dubrovinsky, N. Dubrovinskaia, V. B. Prakapenka, and A. M. Abakumov, Nature communications **3**, 1 (2012).

[80] J. Liu, Chinese Physics B **25**, 076106 (2016).

[81] S. Saxena, L. Dubrovinsky, P. Häggkvist, Y. Cerenius, G. Shen, and H. Mao, Science **269**, 1703 (1995).

[82] A. Zerr, A. Diegeler, and R. Boehler, Science **281**, 243 (1998).

[83] A. F. Goncharov, P. Beck, V. V. Struzhkin, R. J. Hemley, and J. C. Crowhurst, Journal of Physics and Chemistry of Solids **69**, 2217 (2008).

[84] R. Boehler, Reviews of Geophysics **38**, 221 (2000).

[85] S. Anzellini, A. Dewaele, M. Mezouar, P. Loubeyre, and G. Morard, Science **340**, 464 (2013).

[86] A. Salamat, R. A. Fischer, R. Briggs, M. I. McMahon, and S. Petitgirard, Coordination Chemistry Reviews **277**, 15 (2014).

[87] S. Tateno, K. Hirose, Y. Ohishi, and Y. Tatsumi, Science **330**, 359 (2010).

[88] E.-R. Carl, U. Mansfeld, H.-P. Liermann, A. Danilewsky, F. Langenhorst, L. Ehm, G. Trullenque, and T. Kenkmann, Meteoritics & Planetary Science **52**, 1465 (2017).

[89] E.-R. Carl, H.-P. Liermann, L. Ehm, A. Danilewsky, and T. Kenkmann, Meteoritics & Planetary Science **53**, 1687 (2018).

[90] M. Sims, S. J. Jaret, E.-R. Carl, B. Rhymer, N. Schrodt, V. Mohrholz, J. Smith, Z. Konopkova, H.-P. Liermann, T. D. Glotch, et al., Earth and Planetary Science Letters **507**, 166 (2019).

[91] R. Schoenlein, S. Chattopadhyay, H. Chong, T. Glover, P. Heimann, C. Shank, A. Zholents, and M. Zolotorev, Science **287**, 2237 (2000).

[92] S. Khan, K. Holldack, T. Kachel, R. Mitzner, and T. Quast, Physical Review Letters **97**, 074801 (2006).

[93] P. Beaud, S. Johnson, A. Streun, R. Abela, D. Abramsohn, D. Grolimund, F. Krasniqi, T. Schmidt, V. Schlott, and G. Ingold, Physical review letters **99**, 174801 (2007).

[94] R. Schoenlein, T. Elsaesser, K. Holldack, Z. Huang, H. Kapteyn, M. Murnane, and M. Woerner, Philosophical Transactions of the Royal Society A **377**, 20180384 (2019).

[95] J. M. Madey, Journal of Applied Physics **42**, 1906 (1971).

[96] D. A. Deacon, L. Elias, J. M. Madey, G. Ramian, H. Schwettman, and T. I. Smith, Physical Review Letters **38**, 892 (1977).

[97] V. Ayvazyan, N. Baboi, J. Bähr, V. Balandin, B. Beutner, A. Brandt, I. Bohnet, A. Bolzmann, R. Brinkmann, O. Brovko, et al., The European Physical Journal D-Atomic, Molecular, Optical and Plasma Physics **37**, 297 (2006).

[98] C. Bostedt, S. Boutet, D. M. Fritz, Z. Huang, H. J. Lee, H. T. Lemke, A. Robert, W. F. Schlotter, J. J. Turner, and G. J. Williams, Reviews of Modern Physics **88**, 015007 (2016).

[99] T. Ishikawa, H. Aoyagi, T. Asaka, Y. Asano, N. Azumi, T. Bizen, H. Ego, K. Fukami, T. Fukui, Y. Furukawa, et al., nature photonics **6**, 540 (2012).

[100] A. Gleason, C. Bolme, H. Lee, B. Nagler, E. Galtier, D. Milathianaki, J. Hawreliak, R. Kraus, J. Eggert, D. Fratanduono, et al., Nature communications **6**, 1 (2015).

[101] A. Gleason, C. Bolme, H. Lee, B. Nagler, E. Galtier, R. Kraus, R. Sandberg, W. Yang, F. Langenhorst, and W. Mao, Nature communications **8**, 1 (2017).

[102] D. Kraus, J. Vorberger, A. Pak, N. Hartley, L. Fletcher, S. Frydrych, E. Galtier, E. Gamboa, D. Gericke, S. Glenzer, et al., Nature Astronomy **1**, 606 (2017).

[103] M. Guarguaglini, J.-A. Hernandez, T. Okuchi, P. Barroso, A. Benuzzi-Mounaix, M. Bethkenhagen, R. Bolis, E. Brambrink, M. French, Y. Fujimoto, et al., Scientific reports **9**, 1 (2019).

[104] J.-A. Hernandez, G. Morard, M. Guarguaglini, R. Alonso-Mori, A. Benuzzi-Mounaix, R. Bolis, G. Fiquet, E. Galtier, A. Gleason, S. Glenzer, et al., Geophysical Research Letters **47**, e2020GL088887 (2020).

[105] M. Gorman, A. Coleman, R. Briggs, R. McWilliams, D. McGonegle, C. Bolme, A. Gleason, E. Galtier, H. Lee, E. Granados, et al., Scientific reports **8**, 1 (2018).

[106] R. Briggs, R. Torchio, A. Sollier, F. Occelli, L. Videau, N. Kretzschmar, and M. Wulff, Journal of Synchrotron Radiation **26**, 96 (2019).

[107] S.-N. Luo, T. J. Ahrens, and P. D. Asimow, Journal of Geophysical Research: Solid Earth **108** (2003).

[108] B. A. Remington, R. E. Rudd, and J. S. Wark, Physics of Plasmas **22**, 090501 (2015).

[109] J. I. Langford and A. Wilson, Journal of applied crystallography **11**, 102 (1978).

[110] P. Celliers, G. Collins, D. Hicks, and J. Eggert, Journal of applied physics **98**, 113529 (2005).

[111] B. Nagler, B. Arnold, G. Bouchard, R. F. Boyce, R. M. Boyce, A. Callen, M. Campell, R. Curiel, E. Galtier, J. Garofoli, et al., Journal of synchrotron radiation **22**, 520 (2015).

[112] H. T. Philipp, M. Hromalik, M. Tate, L. Koerner, and S. M. Gruner, Nuclear Instruments and Methods in Physics Research Section A: Accelerators, Spectrometers, Detectors and Associated Equipment **649**, 67 (2011).

[113] M. O. Schoelmerich, T. Tschentscher, S. Bhat, C. A. Bolme, E. Cunningham, R. Farla, E. Galtier, A. E. Gleason, M. Harmand, Y. Inubushi, et al., Scientific Reports **10**, 1 (2020).

[114] I. Kantor, V. Prakapenka, A. Kantor, P. Dera, A. Kurnosov, S. Sinogeikin, N. Dubrovinskaia, and L. Dubrovinsky, Review of Scientific Instruments **83**, 125102 (2012).

[115] C. Prescher and V. B. Prakapenka, High Pressure Research **35**, 223 (2015).

[116] A. Méndez, H. Marquardt, R. Husband, I. Schwark, J. Mainberger, K. Glazyrin, A. Kurnosov, C. Otzen, N. Satta, J. Bednarcik, et al., Review of Scientific Instruments **91**, 073906 (2020).

[117] J.-P. Colombier, P. Combis, F. Bonneau, R. Le Harzic, and E. Audouard, Physical review B **71**, 165406 (2005).

[118] C. Fortmann-Grote, A. Andreev, K. Appel, J. Branco, R. Briggs, M. Bussmann, A. Buzmakov, M. Garten, A. Grund, A. Huebl, et al., in *Advances in X-ray Free-Electron Lasers Instrumentation IV* (International Society for Optics and Photonics, 2017), vol. 10237, p. 102370S.

[119] J. MacFarlane, I. Golovkin, and P. Woodruff, Journal of Quantitative Spectroscopy and Radiative Transfer **99**, 381 (2006).

[120] J. E. Jones, Proceedings of the Royal Society of London. Series A, Containing Papers of a Mathematical and Physical Character **106**, 463 (1924).

[121] P. Hohenberg and W. Kohn, Physical review **136**, B864 (1964).

[122] N. D. Mermin, Physical Review **137**, A1441 (1965).

[123] W. Lorenzen, Doktorarbeit, Universität Rostock (2012).

[124] J. P. Perdew, K. Burke, and M. Ernzerhof, Physical review letters **77**, 3865 (1996).

[125] W. Kohn and L. J. Sham, Physical review **140**, A1133 (1965).

[126] P. Giannozzi, S. Baroni, N. Bonini, M. Calandra, R. Car, C. Cavazzoni, D. Ceresoli, G. L. Chiarotti, M. Cococcioni, I. Dabo, et al., Journal of physics: Condensed matter **21**, 395502 (2009).

[127] P. E. Blöchl, Physical review B **50**, 17953 (1994).

[128] G. Kresse and D. Joubert, Physical review b **59**, 1758 (1999).

[129] E. Weinan and D. Li, Communications on pure and applied mathematics **61**, 96 (2008).

[130] J. W. Forbes, *Shock wave compression of condensed matter: a primer* (Springer Science & Business Media, 2013).

[131] B. H. Toby and R. B. Von Dreele, Journal of Applied Crystallography **46**, 544 (2013).

[132] A. Altomare, C. Cuocci, C. Giacovazzo, A. Moliterni, R. Rizzi, N. Corriero, and A. Falcicchio, Journal of Applied Crystallography **46**, 1231 (2013).

[133] S.-N. Luo, J. L. Mosenfelder, P. D. Asimow, and T. J. Ahrens, Geophysical Research Letters **29**, 36 (2002).

[134] G. Kerley, Rep. KPS99 **4** (1999).

[135] M. D. Furnish, L. Shulenburger, M. Desjaralais, and Y. Fei, Tech. Rep., Sandia National Lab.(SNL-NM), Albuquerque, NM (United States) (2017).

[136] R. Angel, Computer program. Crystallography Laboratory, Department of Geological Sciences, Virginia Tech, Blacksburg (2001).

[137] F. Birch, Journal of Geophysical Research: Solid Earth **83**, 1257 (1978).

[138] R. Jeanloz, P. M. Celliers, G. W. Collins, J. H. Eggert, K. K. Lee, R. S. McWilliams, S. Brygoo, and P. Loubeyre, Proceedings of the National Academy of Sciences **104**, 9172 (2007).

[139] Y. Fei, H.-k. Mao, and R. J. Hemley, The Journal of chemical physics **99**, 5369 (1993).

[140] H. Watanabe et al., High-pressure Research in Geophysics pp. 441–464 (1982).

[141] C. Meade and R. Jeanloz, Geophysical Research Letters **17**, 1157 (1990).

[142] I. Jackson and T. J. Ahrens, Physics of the Earth and Planetary Interiors **20**, 60 (1979).

[143] P. Juhás, T. Davis, C. L. Farrow, and S. J. Billinge, Journal of Applied Crystallography **46**, 560 (2013).

[144] J. Wackerle, Journal of applied physics **33**, 922 (1962).

[145] L. V. Al'tshuler, Soviet Physics Uspekhi **8**, 52 (1965).

[146] R. Fowles, Journal of Geophysical Research **72**, 5729 (1967).

[147] R. Trunin, G. Simakov, M. Podurets, B. Moiseyev, and L. Popov, Izv. Acad. Sci. USSR Phys. Solid Earth **1**, 13 (1971).

[148] M. Van Thiel (1977).

[149] S. P. Marsh, *LASL shock Hugoniot data*, vol. 5 (University of California Press, 1980).

[150] G. A. Lyzenga, T. J. Ahrens, and A. C. Mitchell, Journal of Geophysical Research: Solid Earth **88**, 2431 (1983).

[151] S. J. Tracy, S. J. Turneaure, and T. S. Duffy, arXiv preprint arXiv:2005.01871 (2020).

[152] L.-G. Liu, W. A. Bassett, and J. Sharry, Journal of Geophysical Research: Solid Earth **83**, 2301 (1978).

[153] S. J. Tracy, S. J. Turneaure, and T. S. Duffy, Physical review letters **120**, 135702 (2018).

[154] E. M. Stolper and T. J. Ahrens, Geophysical Research Letters **14**, 1231 (1987).

[155] H. Tan and T. J. Ahrens, Journal of Applied Physics **67**, 217 (1990).

[156] D. Grady, W. Murri, and G. Fowles, Journal of Geophysical Research **79**, 332 (1974).

[157] M. Podurets, P. MA, and T. RF (1976).

[158] J. A. Akins and T. J. Ahrens, Geophysical Research Letters **29**, 31 (2002).

[159] Y. Shen, S. B. Jester, T. Qi, and E. J. Reed, Nature materials **15**, 60 (2016).

[160] D. Andrault, G. Morard, G. Garbarino, M. Mezouar, M. A. Bouhifd, and T. Kawamoto, Physics and Chemistry of Minerals **47**, 10 (2020).

[161] A. B. Belonoshko and L. S. Dubrovinsky, Geochimica et Cosmochimica Acta **59**, 1883 (1995).

[162] G. Shen and P. Lazor, Journal of Geophysical Research: Solid Earth **100**, 17699 (1995).

[163] J. Zhang, R. C. Liebermann, T. Gasparik, C. T. Herzberg, and Y. Fei, Journal of Geophysical Research: Solid Earth **98**, 19785 (1993).

[164] G. Q. Chen, T. J. Ahrens, W. Yang, and J. K. Knowles, Journal of the Mechanics and Physics of Solids **47**, 763 (1999).

[165] G. Spiekermann, M. Harder, K. Gilmore, P. Zalden, C. J. Sahle, S. Petitgirard, M. Wilke, N. Biedermann, C. Weis, W. Morgenroth, et al., Physical Review X **9**, 011025 (2019).

[166] M. Guthrie, C. Tulk, C. Benmore, J. Xu, J. Yarger, D. Klug, J. Tse, H. Mao, and R. Hemley, Physical Review Letters **93**, 115502 (2004).

[167] Q. Mei, S. Sinogeikin, G. Shen, S. Amin, C. Benmore, and K. Ding, Physical Review B **81**, 174113 (2010).

[168] X. Hong, L. Ehm, and T. S. Duffy, Applied Physics Letters **105**, 081904 (2014).

[169] C. Prescher, V. B. Prakapenka, J. Stefanski, S. Jahn, L. B. Skinner, and Y. Wang, Proceedings of the National Academy of Sciences **114**, 10041 (2017).

[170] R. Briggs, M. Gorman, S. Zhang, D. McGonegle, A. Coleman, F. Coppari, M. Morales-Silva, R. Smith, J. Wicks, C. Bolme, et al., Applied Physics Letters **115**, 264101 (2019).

[171] A. Gratz, L. DeLoach, T. Clough, and W. Nellis, Science **259**, 663 (1993).

[172] H. Zheng, R. K. Smith, Y.-w. Jun, C. Kisielowski, U. Dahmen, and A. P. Alivisatos, science **324**, 1309 (2009).

[173] V. Fokin, N. Yuritsyn, and E. Zanotto, *Nucleation theory and applications* (2005).

[174] F. Huang, H. Zhang, and J. F. Banfield, Nano letters **3**, 373 (2003).

[175] H. Kirchner, Metallurgical Transactions **2**, 2861 (1971).

[176] M. Ghasemzadeh, A. Nemati, A. Nozad, Z. Hamnabard, and S. Baghshahi, Ceramics-Silikaty **55**, 188 (2011).

[177] M. Boslough, Journal of Geophysical Research: Solid Earth **93**, 6477 (1988).

[178] R. Smith, J. Eggert, M. Saculla, A. Jankowski, M. Bastea, D. Hicks, and G. Collins, Physical review letters **101**, 065701 (2008).

[179] R. Smith, J. Eggert, D. Swift, J. Wang, T. S. Duffy, D. Braun, R. Rudd, D. Reisman, J.-P. Davis, M. Knudson, et al., Journal of Applied Physics **114**, 223507 (2013).

[180] L. Rapp, B. Haberl, C. J. Pickard, J. E. Bradby, E. G. Gamaly, J. S. Williams, and A. V. Rode, Nature communications **6**, 1 (2015).

[181] A. Coleman, M. Gorman, R. Briggs, R. McWilliams, D. McGonegle, C. Bolme, A. Gleason, D. Fratanduono, R. Smith, E. Galtier, et al., Phys. Rev. Lett. **122**, 255704 (2019).

[182] C. M. Pépin, A. Sollier, A. Marizy, F. Occelli, M. Sander, R. Torchio, and P. Loubeyre, Physical Review B **100**, 060101 (2019).

[183] C. Lin, J. S. Smith, S. V. Sinogeikin, C. Park, Y. Kono, C. Kenney-Benson, E. Rod, and G. Shen, Journal of Applied Physics **119**, 045902 (2016).

[184] T. Kubo, T. Kato, Y. Higo, and K.-i. Funakoshi, Science advances **1**, e1500075 (2015).

[185] P. M. Kaercher, E. Zepeda-Alarcon, V. B. Prakapenka, W. Kanitpanyacharoen, J. S. Smith, S. Sinogeikin, and H.-R. Wenk, Physics and Chemistry of Minerals **42**, 275 (2015).

[186] D. Donadio, R. Martoňák, P. Raiteri, and M. Parrinello, Physical review letters **100**, 165502 (2008).

[187] N. Simha and L. Truskinovsky, Acta metallurgica et materialia **42**, 3827 (1994).

[188] L. Huang, M. Durandurdu, and J. Kieffer, Nature materials **5**, 977 (2006).

[189] T. Yagi, M. Yamakata, H. Aoki, Y. Syono, and R. Hemley, Physics Meets Mineralogy: Condensed Matter Physics in the Geosciences pp. 242–256 (2000).

[190] T. Sekine, M. Akaishi, and N. Setaka, Geochimica et Cosmochimica Acta **51**, 379 (1987).

[191] J. A. Akins, Ph.D. thesis, California Institute of Technology (2003).

[192] O. Tschauner, S.-N. Luo, P. D. Asimow, and T. J. Ahrens, American Mineralogist **91**, 1857 (2006).

[193] T. G. Sharp and P. S. DeCarli, Meteorites and the early solar system II **943**, 653 (2006).

[194] D. Hicks, T. Boehly, J. Eggert, J. Miller, P. Celliers, and G. Collins, Physical Review Letters **97**, 025502 (2006).

Curriculum vitae

EDUCATION

- 05/2017-present: European XFEL, Germany
  Joint Ph.D. student of the HED group at European XFEL and in the Statistical Physics Group, supervisor: Prof. Ronald Redmer

- 04/2014-09/2016: Goethe University Frankfurt, Germany
  Master of Science (M.Sc.) in Geoscience
  Master thesis supervised by Prof. Gerhard Brey:
  Evaporational loss of lithium during high temperature experiments: Implications for chondrule formation
  Final mark: 1,0 *with distinction*

- 04/2011-03/2014: Goethe University Frankfurt, Germany
  Bachelor of Science (B.Sc.) in Geoscience
  Bachelor thesis supervised by Prof. Gerhard Brey:
  Chemical analysis of the carbonaceous meteorite NWA 5515 with SEM, EPMA and LA-ICP-MS
  Final mark: 2,0

- 04/2010-04/2011: Georg-August University, Göttingen, Germany
  Bachelor of Science (B.Sc.) in Physics

- 10/2008-04/2010: Freie University Berlin, Germany
  Bachelor of Science (B.Sc.) in Physics

- 06/2007: Pindl Gymnasium Regensburg, Germany
  University entrance diploma (Abitur)
  Final mark: 1.8

RESEARCH EXPERIENCE

- 2017-present: Doctoral candidate, scientific assistant, European XFEL, 22869 Schenefeld, Germany
- 2013-2017: Scientific assistant, Goethe University Frankfurt, 60438 Frankfurt Germany
- 2015: Visiting student research assistant, Woods Hole Oceanographic Institution, Woods Hole, MA02543, USA
- 2013 Stagiaire, European Space Agency (ESA), 2201 Noordwijk, Netherlands

LIST OF PUBLICATIONS DURING THE Ph.D.

1. **Schoelmerich M.O.**, Tschentscher T., Baht S., Bolme C., Cunningham E., Farla R., Galtier E., Gleason A.E., Harmand M., Inubushi Y., Katagiri K., Miyanishi K., Nagler B., Ozaki N., Preston T.R., Redmer R., Smith R., Tobase T., Togashi T., Tracy S.J., Umeida Y., Wollenweber L., Yabuuchi T., Zastrau U., and Appel K.
   Evidence of shock-compressed stishovite above 300 GPa
   Scientific Reports **10(1)**, 1-8 (2020)

2. Hartley N.J., Brown S., Cowan T.E., Cunningham E., Döppner T., Falcone R.W., Fletcher L.B., Frydrych S., Galtier E., Gamboa E.J., Garcia A.L., Gericke D. O., Granados E., Heimann P. A., Lee H. J., MacDonald M. J., MacKinnon A. J., McBride E. E., Nam I., Neumayer P., Pak A., Pelka A., Prencipe I., Ravasio A., Rödel M., Rohatsch A.M., Saunders A.M., **Schölmerich M.O.**, Schörner M., Schuster A.K., Sun P., van Driel T., Vorberger J. and Kraus D.
   Evidence for Crystalline structure in Dynamically-Compressed Polyethylene up to 200 GPa
   Scientific Reports **9(1)**, 1-7 (2019)

3. Kraus D., Hartley N. J., Frydrych S., Schuster A. K., Rohatsch K., Rödel M., Cowan T. E., Brown S., Cunningham E., van Driel T., Fletcher L. B., Galtier E., Gamboa E. J., Laso Garcia A., Gericke D. O., Granados E., Heimann P. A., Lee H. J., MacDonald M. J., MacKinnon A. J., McBride E. E., Nam I., Neumayer P., Pak A., Pelka A., Prencipe I., Ravasio A., Redmer R., Saunders A. M., **Schölmerich M.O.**, Schörner M., Sun P., Turner S. J., Zettl A., Falcone R. W., Glenzer S. H., Döppner T., and Vorberger J.
   High-pressure chemistry of hydrocarbons relevant to planetary interiors and inertial confinement fusion
   Phys. Plasmas **25**, 056313 (2018)

LIST OF CONFERENCE CONTRIBUTIONS

- **Schoelmerich M.O.**, Appel K., Tschentscher T., Bolme C., Cunningham E., Galtier E., Gleason A.E., Nagler B., Preston R.T., Smith R., Tracy S.J., Wollenweber L., Zastrau U.
  Femtosecond diffraction studies of shock-compressed silicate melts at the LCLS-XFEL
  EPSC Abstracts **13**, EPSC-DPS2019-531 (2019)

- Kim D., Tracy S.J., Berryman E.J., Han S., Smith R., Gleason A.E., Bolme C., Appel K., **Schoelmerich M.O.**, Prakapenka V.B. and Lee H.J.
  X-ray Diffraction Study of Laser-shocked Forsterite (Mg2SiO4) from 20-130 GPa
  AGUFM 2019, MR23D-0152 (2019)

- Tracy S.J., Smith R., Berryman E., Kim D., Han S., Gleason A.E., Bolme C., **Schoelmerich M.O.**, Appel K., Prakapenka V. and Lee H.J.
  Calcite Phase Transitions and Melting Under Shock Loading and Release Using Ultrafast X-Ray Diffraction
  AGUFM 2019, MR33A-03 (2019)

Oral contributions:

- 6th Joint Workshop on High Pressure, Planetary and Plasma Physics (HP4), Göttingen, Germany (10/4/2017) “Dynamic compression experiments with the new High Energy Density Science (HED) instrument at the European XFEL”

- Workshop “Low Mass Planets”, University of Rostock, Germany (8/7/2018) “Dynamic compression experiments at X-Ray Free-Electron Laser (XFELs)”

- European Planetary Science Congress, Geneva, Switzerland (9/19/2019) “Femtosecond diffraction studies of shock-compressed silicate melts at the LCLS-XFEL”

- 7th High-Power Laser Workshop SLAC National Accelerator Laboratory, Menlo Park USA, (9/27/2019) “Structure of SiO_2 melts at ultrahigh pressures“

- Workshop: Experimental Work at DESY and EuXFEL, Hamburg, Germany (12/12/2019) “Dynamic laser shock compression experiments on SiO_2 at LCLS and SACLA”

LIST OF PROPOSALS WITH GRANTED BEAMTIME

1. Appel, K. (PI), Schoelmerich, M.O. (Co-PI), Tschentscher, T., Zastrau, U. *et al.*
   Structure of SiO_2 melts at ultrahigh pressures
   Matter in Extreme Conditions (MEC) end-station of the Linac Coherent Light Source (proposal LS84 in run 17, 2018).

2. Tschentscher, T. (PI), Schoelmerich, M.O. (Co-PI), Appel, K. *et al.*
   Melting structure of SiO_2 and its analogues – kinetics at superheating conditions
   BL3:EH5 end-station of the SACLA (proposal 2019A8072, 2019).

3. Schoelmerich, M.O. (PI), Appel, K. (Co-PI) *et al.*
   Dynamic compression of cristobalite at in-situ conditions
   P02.2 end-station of PETRAIII at DESY (proposal I-20180745, 2019).

Acknowledgements

I would like to express my sincere gratitude to my supervisor Karen Appel for the incredible support and encouragement throughout my Ph.D., in particular during stressful beamtimes (and their preparation) and her constant guidance during all circumstances.
Further I would like to thank Prof. Ronald Redmer for the great opportunity of being his Ph.D. student within the field of high-pressure/XFEL science, and his outstanding scientific support.
Moreover, I would like to thank Thomas Tschentscher for the great discussions and extremely fruitful conclusions, which improved my research significantly. Also counting, the fact that he was able to join two of my three beamtimes, which is tremendous, considering his everyday work load and schedule, and it is greatly appreciated.
I would also like to thank my group leader Ulf Zastrau for his generous support for our research, enhancement of our talents and vivid discussions. Further, he always made us Ph.D. student feel to be equal scientists within the HED group at the European XFEL, for which I would like to express my gratitude.
Furthermore I would like to thank my fellow Ph.D. students, Nicole, Lennart, Christian, Alba and Johannes, who actively helped me throughout my beamtimes, gave always great input and were just incredible colleagues!
I also would like to seize the opportunity and thank my collaborators, in particular Florian Trybel and Gerd Steinle-Neumann for their extraordinary help with computational simulations and, among others, Ray Smith, Arianna Gleason, Cindy Bolme and Marion Harmand for their actively help during stressful beamtimes. I would further like to thank Shrikant Bhat and Robert Farla for their vivid help at the Large Volume Press.
This work was moreover funded by the Deutsche Forschungsgemeinschaft (DFG) within the DFT research unit 2440 ”Matter Under Planetary Interior Conditions”. Special thanks also to the researchers of this group for support and collaboration.
Finally I would like to thank my wife Marie, who supports me everyday in every situation and without her, I would not be where I am today.

Statement of authorship

I hereby declare that I am the sole author of this thesis and that I have not used any sources other than those listed in the bibliography and identified as references. I further declare that I have not submitted this thesis at any other institution in this form or a otherwise.

Ich versichere hiermit an Eides statt, dass ich die vorliegende Arbeit selbständig angefertigt und ohne fremde Hilfe verfasst habe, keine außer den von mir angegebenen Hilfsmitteln und Quellen dazu verwendet habe und die den benutzten Werken inhaltlich und wörtlich entnommenen Stellen als solche kenntlich gemacht habe. Weiterhin versichere ich, dass ich diese Arbeit an keiner anderen Institution in dieser oder einer ähnlichen Form eingereicht habe.

Markus Schölmerich

Rostock, 10. November 2020